

DYNAMIC MODELLING AND CONTROL OF A GIMBALLED AIRBORNE
ANTENNA PLATFORM WITH MASS UNBALANCE AND FRICTION

A THESIS SUBMITTED TO
THE GRADUATE SCHOOL OF NATURAL AND APPLIED SCIENCES
OF
MIDDLE EAST TECHNICAL UNIVERSITY

BY

TUĞÇE ŞEREF

IN PARTIAL FULFILLMENT OF THE REQUIREMENTS
FOR
THE DEGREE OF MASTER OF SCIENCE
IN
ELECTRICAL AND ELECTRONICS ENGINEERING

AUGUST 2018

Approval of the thesis:

**DYNAMIC MODELLING AND CONTROL OF A GIMBALLED AIRBORNE
ANTENNA PLATFORM WITH MASS UNBALANCE AND FRICTION**

submitted by **TUĞÇE ŞEREF** in partial fulfillment of the requirements for the degree of **Master of Science in Electrical and Electronics Engineering Department, Middle East Technical University** by,

Prof. Dr. Halil Kalıpçılar
Dean, Graduate School of **Natural and Applied Sciences**

Prof. Dr. Tolga Çiloğlu
Head of Department, **Electrical and Electronics Engineering**

Prof. Dr. Kemal Leblebicioğlu
Supervisor, **Electrical and Electronics Eng. Dept., METU**

Examining Committee Members:

Prof. Dr. Coşku Kasnakoğlu
Electrical and Electronics Eng. Dept., TOBB Univ.

Prof. Dr. Kemal Leblebicioğlu
Electrical and Electronics Eng. Dept., METU

Assoc. Prof. Dr. Klaus Werner Schmidt
Electrical and Electronics Eng. Dept., METU

Assist. Prof. Dr. Mustafa Mert Ankaralı
Electrical and Electronics Eng. Dept., METU

Assist. Prof. Dr. Ulaş Beldek
Mechatronics Eng. Dept., Çankaya University

Date:

15.08.2018

I hereby declare that all information in this document has been obtained and presented in accordance with academic rules and ethical conduct. I also declare that, as required by these rules and conduct, I have fully cited and referenced all material and results that are not original to this work.

Name, Last Name: TUĞÇE ŞEREF

Signature :

ABSTRACT

DYNAMIC MODELLING AND CONTROL OF A GIMBALLED AIRBORNE ANTENNA PLATFORM WITH MASS UNBALANCE AND FRICTION

Şeref, Tuğçe

M.S., Department of Electrical and Electronics Engineering

Supervisor : Prof. Dr. Kemal Leblebicioğlu

August 2018, 101 pages

Inertial stabilized gimballed systems are widely-used in many applications to achieve a high precision positioning. Airborne antennas pointing target as a part of the satellite communication may be examples of such systems.

This thesis presents the dynamic modelling and control of a two axes gimballed airborne antenna platform. First, reference frames and the transformation matrices are defined to build up the motion of the antenna and kinematic equations of each gimbal are derived. Next, the dynamic equations including mass unbalance of the gimbals and the friction torques about pivot points are obtained.

Then, the study puts emphasis on the concepts of the static and dynamic mass unbalance and also argues how much each mass unbalance affects the operation. Furthermore, a dynamic model, Lugre friction, establishes the friction torques for both of the gimbals.

All these studies results in the complete dynamic model of the two axes gimballed airborne antenna platform. The overall system model is implemented in MATLAB/Simulink environment. Next, system identification studies to determine the parameters of the Lugre friction model have been performed by two different methods based on real and simulated data. Finally, PI based controllers have been designed for the overall system in several design stages.

Keywords: Gimballed systems, friction identification, dynamic and static mass unbalance, cascade PID controller.

ÖZ

ÇİFT EKSENLİ, HAVA ARACINA MONTE ANTEN PLATFORMUNUN KÜTLE DENGESİZLİĞİ VE SÜRTÜNME İLE DİNAMİK MODELLENMESİ VE KONTROLÜ

Şeref, Tuğçe

Yüksek Lisans, Elektrik ve Elektronik Mühendisliği Bölümü

Tez Yöneticisi : Prof. Dr. Kemal Leblebicioğlu

Ağustos 2018 , 101 sayfa

Yüksek hassasiyette konumlanma ve kontrolün sağlanması için gimbal sistemleri birçok alanda kullanılmaktadır. Uydu haberleşmesi yapacak hava araçlarına yerleştirilen bu şekilde tasarlanmış anten platformları bu uygulamalara örnek olarak gösterilebilir.

Bu tez böyle bir anten platformunun dinamik modellenmesi ve kontrol edilmesini anlatmaktadır. Öncelikle referans koordinat düzlemleri ve bu düzlemler arasında çevrimleri gerçekleştirecek geçiş matrisleri tanımlandı. Bu kavramlar kullanılarak kinematik ve dinamik denklemler elde edildi.

Daha sonra kütle dengesizliği üzerinde duruldu. Hem statik hem de dinamik kütle dengesizliğinin sistemi nasıl etkilediği gösterildi. Ek olarak, her iki gimbal için de Lugre sürtünme modelinin tanımlanması yapıldı.

Bütün bu çalışmalar sonunda tüm sisteme ait matematiksel model elde edilmiştir. Bu model daha sonra MATLAB/Simulink ortamında kodlanmıştır. Ortaya çıkan karmaşık yapıdaki Lugre sürtünme modeline ait katsayılar, iki farklı yöntemle, gerçek ve benzetim verileri üzerinden sistem tanımlama yöntemleri ile bulunmuş ve sonuçlar karşılaştırılmıştır. En sonunda, çok katlı PI denetleyicileri ile tüm sistem için kontrol-cular tasarlanmıştır.

Anahtar Kelimeler: Gimbal sistemleri, srtnme modelleme, dinamik ve statik ktle dengesizliđi, ok katlı PID denetleyici.

ACKNOWLEDGMENTS

I would like to express my gratitude for my supervisor Professor Kemal Leblebicioğlu for his guidance, patience and sincere friendship throughout the thesis work. It has been such great experience for me to work with him.

I want to thank Enis Kobal for his endless and precious support that motivates me at the every stage of the work. I also thank Erhan Poyrazoğlu for his great help and contribution to the theoretical background of the work. He has always answered my questions about the dynamic modelling kindly and helped me a lot to understand the concepts regarding the inertially stabilized system.

I would like to thank ASELSAN since it has given me a chance to work on such a project and supported the study.

TABLE OF CONTENTS

ABSTRACT	v
ÖZ	vii
ACKNOWLEDGMENTS	x
TABLE OF CONTENTS	xi
LIST OF TABLES	xvi
LIST OF FIGURES	xviii
LIST OF ABBREVIATIONS	xxi
CHAPTERS	
1 INTRODUCTION	1
1.1 Inertially Stabilized Systems	1
1.2 Motivation for Work	2
1.3 Organization of the Thesis	4
2 KINEMATIC AND DYNAMIC EQUATIONS	7
2.1 Introduction	7
2.2 Reference Frames and Transformation Matrices	8
2.3 Kinematic Equations	11

2.3.1	Angular Velocities	12
2.3.1.a	Angular Velocity of the Outer Gimbal	12
2.3.1.b	Angular Velocity of the Inner Gimbal .	14
2.3.2	Angular Accelerations	15
2.3.2.a	Angular Acceleration of the Outer Gimbal	16
2.3.2.b	Angular Acceleration of the Inner Gimbal	16
2.4	Dynamic Equations	17
2.4.1	Dynamic Equation of the Inner Gimbal	18
2.4.2	Dynamic Equation of the Outer Gimbal	20
3	DYNAMIC AND STATIC MASS UNBALANCE	25
3.1	Introduction	25
3.2	Dynamic Mass Unbalance	26
3.2.1	Dynamic Mass Unbalance of the Inner Gimbal . .	27
3.2.2	Dynamic Mass Unbalance of the Outer Gimbal . .	28
3.2.3	Simulation Results	30
3.2.3.a	Simulation Construction	30
3.2.3.b	Simulation Results of the Outer Gimbal	32
3.2.3.c	Simulation Results of the Inner Gimbal	36
3.2.3.d	Evaluation of the Results	39
3.3	Static Mass Unbalance	40

3.3.1	Static Mass Unbalance of the Inner Gimbal	40
3.3.2	Static Mass Unbalance of the Outer Gimbal	40
3.3.3	Simulation Results	41
3.3.3.a	Simulation Construction	41
3.3.3.b	Simulation Results of the Outer Gimbal	43
3.3.3.c	Simulation Results of the Inner Gimbal	44
3.3.3.d	Evaluation of the Results	46
3.4	Comparison of the Effects of Dynamic and Static Mass Un- balance	47
4	FRICION IDENTIFICATION	49
4.1	Introduction	49
4.2	Lugre Friction Model	50
4.3	The Identification of Friction Model with the Physical Sys- tem	52
4.3.1	Sliding Phase Experiments	52
4.3.1.a	Experimental Setup	53
4.3.1.b	Identification of Static Parameters	54
4.3.2	Presliding Phase Experiments	57
4.3.2.a	Experimental Setup	58
4.3.3	The Identified Friction Models	60
4.3.3.a	Lugre Friction Model of the Inner Gim- bal	60

	4.3.3.b	Lugre Friction Model of the Outer Gimbal	61
4.4		The Identification of Friction Model in Simulation Environment	62
	4.4.1	Simulation Construction	62
	4.4.2	The Optimization Method	63
	4.4.2.a	The Friction Parameters of the Outer Gimbal	65
	4.4.2.b	The Friction Parameters of the Inner Gimbal	66
5		MATHEMATICAL MODEL AND THE CONTROLLER	69
	5.1	Introduction	69
	5.2	Dynamic Models	70
	5.2.1	Dynamic Model Representation of the Outer Gimbal	70
	5.2.2	Dynamic Model Representation of the Inner Gimbal	70
	5.3	Cascade PI Controller	71
	5.3.1	Tuning of the Controller Parameters	73
	5.3.2	The Secondary Controller Design	74
	5.3.3	The Primary Controller Design	79
	5.3.4	The Response of the System	84
	5.3.5	Cascade PI Controller with Prefilters	86
	5.3.6	The Response of the System with Changing Inertia Parameters	91
6		CONCLUSION AND FUTURE WORK	93

6.1	Conclusion	93
6.2	Future Work	96
	REFERENCES	97
	APPENDICES	
A	THE PARAMETERS	101

LIST OF TABLES

TABLES

Table 3.1	Different test cases with varying angular velocity of the platform . . .	32
Table 3.2	Different test cases with varying angular velocity of the platform . . .	42
Table 4.1	The static parameters of Lugre friction model for the inner gimbal . . .	56
Table 4.2	The static parameters of Lugre friction model for the outer gimbal . . .	57
Table 4.3	Presliding phase experimental data	59
Table 4.4	Dynamic parameters of Lugre friction model	60
Table 4.5	The parameters of Lugre friction model for the inner gimbal	60
Table 4.6	The parameters of Lugre friction model for the outer gimbal	61
Table 4.7	The parameters of Lugre friction model for the outer gimbal	65
Table 4.8	Comparison of the parameters	66
Table 4.9	The parameters of Lugre friction model for the inner gimbal	66
Table 4.10	Comparison of the parameters	67
Table 5.1	The effect of increasing PI parameters on the dynamic characteristics	73
Table 5.2	The step response of the secondary control loop with different K_p when $K_i = 300$	74
Table 5.3	The step response of the secondary control loop with different K_i when $K_p = 140$	75
Table 5.4	The step response of the secondary control loop with different K_p values when $K_i = 300$	77
Table 5.5	The step response of the secondary control loop with different K_i when $K_p = 35$	78

Table 5.6 The step response of the primary control loop with different K_p when $K_i = 10$	80
Table 5.7 The step response of the primary control loop with different K_i when $K_p = 7$	81
Table 5.8 The step response of the primary control loop with different K_p values when $K_i = 25$	82
Table 5.9 The step response of the primary control loop with different K_i values when $K_p = 11$	83
Table 5.10 The resultant parameters of the controller	84
Table 5.11 The resultant parameters of the controller with the prefilters	87
Table 5.12 The performance of the outer gimbal with different reference inputs	88
Table 5.13 The performance of the inner gimbal with different reference inputs	89
Table 5.14 The performance of the outer gimbal with different reference inputs	91
Table 5.15 The performance of the inner gimbal with different reference inputs	91
Table A.1 The parameters of the outer gimbal	101
Table A.2 The parameters of the inner gimbal	101

LIST OF FIGURES

FIGURES

Figure 1.1	The airborne antenna platform [6]	2
Figure 1.2	Two axes gimballed airborne antenna platform	4
Figure 2.1	Frames of antenna body	8
Figure 2.2	The transformations between the coordinates and frames	9
Figure 2.3	Coordinate axes	10
Figure 3.1	Stabilization loops for outer and inner gimbals	31
Figure 3.2	Step response of the azimuth axis	33
Figure 3.3	Results with test scenarios when $\omega_{oe_{ref}} = 0.1$ rad/sec	34
Figure 3.4	Results with test scenarios when $\omega_{oe_{ref}} = 0.5$ rad/sec	35
Figure 3.5	The comparison between no disturbance and Case 5 when $\omega_{oe_{ref}} =$ 0.5 rad/sec	36
Figure 3.6	Step response of the elevation axis	37
Figure 3.7	Results with test scenarios when $\omega_{ie_{ref}} = 0.1$ rad/sec	38
Figure 3.8	Results with test scenarios when $\omega_{ie_{ref}} = 0.5$ rad/sec	39
Figure 3.9	Stabilization loops for the outer and the inner gimbals	42
Figure 3.10	Results with test scenarios when $\omega_{oe_{ref}} = 0.1$ rad/sec	43
Figure 3.11	Results with test scenarios when $\omega_{oe_{ref}} = 0.5$ rad/sec	44
Figure 3.12	Results with test scenarios when $\omega_{ie_{ref}} = 0.1$ rad/sec	45
Figure 3.13	Results with test scenarios when $\omega_{ie_{ref}} = 0.5$ rad/sec	46

Figure 4.1	The bristles in LuGre friction model [37]	50
Figure 4.2	The friction-velocity graph of the inner gimbal from the experimental data	53
Figure 4.3	The friction-velocity graph of the outer gimbal from the experimental data	54
Figure 4.4	The estimated friction-velocity graph of the inner gimbal and experimental data	55
Figure 4.5	The estimated friction-velocity graph of the outer gimbal and experimental data	56
Figure 4.6	The friction-velocity graph of the inner gimbal with identified parameters	61
Figure 4.7	The friction-velocity graph of the outer gimbal with identified parameters	62
Figure 4.8	The friction-velocity graph of the inner gimbal with identified parameters	63
Figure 4.9	The friction-velocity graph of the outer gimbal with identified parameters	65
Figure 4.10	The friction-velocity graph of the outer gimbal with identified parameters	67
Figure 5.1	The block diagram of the outer gimbal	70
Figure 5.2	The block diagram of the inner gimbal	71
Figure 5.3	The cascade control system for the outer gimbal	72
Figure 5.4	The cascade control system for the inner gimbal	72
Figure 5.5	The secondary loop of the outer gimbal	74
Figure 5.6	The response of the secondary control loop with different K_p when $K_i = 300$	75
Figure 5.7	The response of the secondary control loop with different K_i when $K_p = 140$	76
Figure 5.8	The secondary loop of the inner gimbal	77

Figure 5.9 The response of the secondary control loop with different K_p values when $K_i = 300$	78
Figure 5.10 The response of the secondary control loop with different K_i values when $K_p = 35$	79
Figure 5.11 The response of the primary control loop with different K_p when $K_i = 10$	80
Figure 5.12 The response of the primary control loop with different K_i when $K_p = 7$	81
Figure 5.13 The response of the primary control loop with different K_p when $K_i=25$	83
Figure 5.14 The response of the primary control loop with different K_i when $K_p = 11$	84
Figure 5.15 The system response of the outer gimbal	85
Figure 5.16 The system response of the inner gimbal	85
Figure 5.17 The block diagram of the system with prefilter	86
Figure 5.18 The response of the outer gimbal with prefilter	87
Figure 5.19 The response of the inner gimbal with prefilter	88
Figure 5.20 The response of the outer gimbal	89
Figure 5.21 The response of the inner gimbal	90

LIST OF ABBREVIATIONS

ISP	Inertially stabilized platform
LTI	Linear time-invariant
PI	Proportional-integral
PID	Proportional-integral-derivative
F_b	Reference frame fixed to the antenna body with u_x^b, u_y^b, u_z^b axes
F_o	Reference frame fixed to the outer gimbal with u_x^o, u_y^o, u_z^o axes
F_i	Reference frame fixed to the inner gimbal with u_x^i, u_y^i, u_z^i axes
F_e	Reference frame fixed to the earth
F_c	One of the intermediate reference frames between the earth frame and the antenna body
F_f	One of the intermediate reference frames between the earth frame and the antenna body
u_z^o	z-axis of Frame Outer(F_o)
u_x^b	x-axis of Frame Base(F_b)
u_y^f	y-axis of Frame F(F_f)
u_z^c	y-axis of Frame C(F_c)
ψ	Yaw angle
θ	Pitch angle
ϕ	Roll angle
η	Azimuth-angle
ε	Elevation-angle
r_{oc_o}	Position vector from the pivot point to COG of the outer gimbal
r_{oc_i}	Position vector from the pivot point to COG of the inner gimbal
g^o	Gravity vector transformed to F_o relative to F_e
g^i	Gravity vector transformed to F_i relative to F_e
R_{ij}	Matrix that transforms of any vector in reference frame (i) to reference frame (j)
P^i	Position vector of “P” relative to frame (i)
P^j	Position vector of “P” relative to frame (j)

ω_{oe}	Angular velocity for the outer gimbal
ω_{ie}	Angular velocity for the inner gimbal
$\omega_{oe_{ref}}$	Reference angular velocity input for the outer gimbal
$\omega_{ie_{ref}}$	Reference angular velocity input for the inner gimbal
α_{oe}	Angular acceleration of the outer body
α_{ie}	Angular acceleration of the inner body
D_o	Time derivative operator for the angular velocity of the outer gimbal
D_i	Time derivative operator for the angular velocity of the inner gimbal
m_o	Mass of the outer gimbal
m_i	Mass of the inner gimbal
a_o	Linear acceleration of the center of gravity of the outer gimbal
a_i	Linear acceleration of the center of gravity of the inner gimbal
F_{oi}	Force applied by the outer gimbal on inner gimbal
F_{bo}	Force applied by base of the platform on the outer gimbal
g	Gravity vector
H^o	Angular momentum of the outer gimbal
H^i	Angular momentum of the inner gimbal
$\Sigma\Gamma$	Total torque acting on the inner/ the outer gimbal
ΔH^o	Variation of angular momentum of the outer gimbal
ΔH^i	Variation of angular momentum of the inner gimbal
I	Inertia of the rotating body induced to the rotational axis
I_o	Inertia tensor of the outer gimbal about pivot point
I_i	Inertia tensor of the inner gimbal about pivot point
I_{yy_i}	Moment of the inner gimbal transferred to y-axis
I_{zz_o}	Moment applied to z-axis of the outer gimbal
α_{oe}	Angular acceleration of the outer gimbal relative to F_e
α_{ie}	Angular acceleration of the inner gimbal relative to F_e
ω_{oe}	Angular velocity of the outer gimbal relative to Frame F_e
ω_{ie}	Angular velocity of the inner gimbal relative to Frame F_e
T_{io}	Moment applied by the inner gimbal on the outer gimbal
T_{oi}	Moment applied by the outer gimbal on the inner gimbal
T_{bo}	Moment applied by the platform base on the outer gimbal

$T_{DynMass_z}$	Disturbance due to dynamic mass unbalance induced on the outer gimbal
$T_{DynMass_y}$	Disturbance due to dynamic mass unbalance induced on the inner gimbal
$T_{StaticMass_z}$	Disturbance torque induced on the azimuth axis
$T_{StaticMass_y}$	Disturbance torque induced on the elevation axis
T_{m_o}	Torque applied by the motor on the rotational axis of the outer gimbal
T_{m_i}	Torque applied by the motor on the rotational axis of the inner gimbal
T_{fr_o}	Friction torque between the motor end the pivot point of the outer body
T_{fr_i}	Friction torque between the motor end the pivot point of the inner body
$T_{fr_{i_z}}$	Transformed friction torque to the azimuth axis, the principal rotational axis, between inner and outer gimbal
T_{fr}	Predicted friction torque
T_s	Stiction torque
T_c	Coulomb torque
T_{ss_i}	Steady state output of Lugre friction torque data
\hat{T}_{ss_i}	Experimental steady state friction torque data
T_{input}	Input torque to the system
v	Velocity between two surfaces in contact
\dot{v}	Angular acceleration
$s(v)$	Stribeck effect
δ	Stribeck shape factor
v_s	Stribeck velocity
σ_0	Stiffness coefficient
σ_1	Damping coefficient
σ_2	Viscous damping coefficient
ζ	Damping ratio
ω_n	Natural frequency of the system
K_p	Proportional gain of the controllers
K_i	Integral gain of the controllers

CHAPTER 1

INTRODUCTION

1.1 Inertially Stabilized Systems

Inertially stabilized platforms (ISP) may be encountered in many engineering applications such as target tracking, missile guidance, communication, hand-held cameras, etc. The electromechanical design of such platforms varies with type of the application; yet, they can be regarded as the combination of a mechanical structure, motor, bearings, mounted-gyroscopes called as a gimbal. In most applications, at least two orthogonal gimbals are implemented [1]. The configuration of a gimballed system may alter according to the application; they may be mounted on aircrafts, spacecrafts, ground vehicles, ships, etc. When a gimballed system is mounted on a moving base, it becomes more complicated due to the base movements, inertial dynamics and sometimes environmental distortions [2], [3].

Even though the specifications and configurations differ widely, the main purpose of ISPs is to keep the orientation of the object towards a specified target. They try to achieve the stable operation via the electro-optic sensors despite the system dynamics such as friction, mass unbalance and the environmental disturbance [1], [4], [5].

This study concentrates on an inertially stabilized system, the two axes gimballed antenna platform that will be mounted on an unmanned aerial vehicle and to be developed by ASELSAN, which is shown in Figure 1.1.



Figure 1.1: The airborne antenna platform [6]

The airborne antenna control platform is a part of a satellite communication terminal which implements voice and data communication. It aims to maintain the link between the satellite and to maximize the satellite tracking accuracy by two axes stabilization control loops; azimuth and elevation axes. The gimballed antenna body has two gimbals named as outer and inner gimbals. The gimbals have their own DC motors; moreover, the encoders and gyros are mounted on them so that they handle the stable operation for a more accurate positioning. Since the RF component in charge of the communication with the satellite takes place at the center of the inner gimbal, especially, the positioning of the inner gimbal gains more importance.

1.2 Motivation for Work

The antenna body is designed and developed by ASELSAN; however, it is not an end product yet, which is still worked on as a prototype. Therefore, the modelling and control of the stabilization loops have not been finalized yet. The main motivation behind the study is to model and to control the system appropriately by simulating the platform under different test conditions imitating the operation of the antenna in real world.

To fulfill the motivation, first, the dynamic modelling of the antenna has been studied in a detailed way, which has the greatest importance throughout the whole study since the accurate stabilization of the system depends on more detailed and correct plant modelling [7]. Kinematic equations have been derived for each gimbal. By Newton-Euler method, the dynamics of the system have been obtained.

During the modelling, the inertial dynamics of the gimbals have been investigated. The effect of non-symmetrical system geometry in the dynamic modelling may be seen as mass unbalance which has been usually ignored in many applications [7]. However, in this study, dynamic and static mass unbalance have been introduced to the system modelling and, how static and dynamic mass unbalance affect the performance has been analysed for each gimbal under different base motions.

Next, the other nonlinear distortion, friction force, has been investigated to come up with a dynamic friction model. Throughout the work on the friction identification, a set of measurements have been taken with a prototype physical platform. In other words, the plant model and the primary control loop are not only based on dynamic equations suggested in this study but also obtained experimentally by ASELSAN to get a set of real measurements. By utilizing the set of data obtained from the experiments, the friction identification has been performed for the LuGre Model, a well-known dynamic friction model, for both outer and inner gimbals. Thus, all the terms established in the dynamic equations have been examined and the dynamic modelling has been completed.

Then, the cascaded PI controllers for each gimbal are designed such that they can achieve a high precision positioning. For such systems, many control methods may be proposed. For this case, a cascade control system have been introduced for the stabilization loop since the effectiveness and the applicability of PI controller has been verified in both simulation environment and in industrial world [8]. Next, the required positioning has been improved by an effective tuning procedure [9].

All in all, this study is mainly about the dynamic modelling and also control of a two axes gimballed system; a part of a satellite communication system, which is presented in Figure 1.2. It provides a plant model covering the main nonlinearities and proposes an effective positioning control method with high accuracy in satellite tracking.

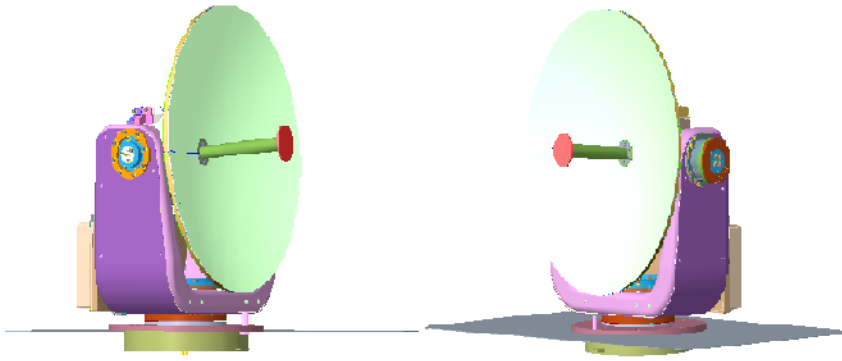


Figure 1.2: Two axes gimbaled airborne antenna platform

1.3 Organization of the Thesis

The remaining part of the thesis work is arranged as following;

Chapter 2 focuses on the kinematic and dynamic equations. First, reference frames, transformation matrices and the derivatives of the transformation matrices have been determined. By using these concepts, the angular velocities of outer and inner gimbals are derived. Then the derivation of the angular velocities of the gimbals takes place. Next, Newton-Euler method is used to obtain the dynamic equations which mainly consist of the angular velocity and angular acceleration terms. As a result, the system dynamics of both inner and outer gimbals are introduced, which will be investigated in a detailed way in next chapters.

Chapter 3 deals with dynamic and static mass unbalance concept. First, Newton-Euler equation for each gimbal is reviewed to concentrate on the terms causing dynamic mass unbalance. Then, how dynamic mass unbalance the gimbals experience affect the performance of the system is investigated with different test cases with a basic stabilization control loop. Next, the concept of static mass unbalance is studied which is already declared due to the asymmetrical geometry of the gimbals in the dynamic equations. Similarly, the influence of the static mass unbalance is investigated via varying test cases as well.

In Chapter 4, the friction force appeared in Newton-Euler equation is studied. First, the dynamic friction model, LuGre friction model, is established by addressing a set of equations based on a number of parameters. Friction identification consists of two set of experiments; sliding and presliding experiments performed with the physical antenna body to estimate the LuGre friction parameters. After identifying the exact parameters, LuGre friction of the gimbals are implemented in Simulink and then a dynamic system identification procedure is performed to estimate the parameters from the model developed in Simulink. Finally, they are compared with the exact parameters identified via the physical experiments.

Chapter 5 discusses the controller part of the thesis. After studying all the components of the dynamic equations, the dynamic model of the gimbals are completed in Simulink and cascade control systems are designed for each gimbal. Two stabilization control loops; the primary and secondary control loops are established for inner and outer gimbals separately in which PI controllers are implemented as the primary and the secondary controllers. Therefore, an effective and an easily-applicable control method is developed on for accurate positioning.

In Chapter 6, all the work carried out in the thesis is summarized. Furthermore, the future work for the end product is addressed.

CHAPTER 2

KINEMATIC AND DYNAMIC EQUATIONS

2.1 Introduction

Dynamic modelling of inertially stabilized systems stands for the formulation of a set of equations characterizing the relationship between the total forces and torques acting on the system and the motion of the system. For a stable control operation, the modelling of plant dynamics is regarded as the first stage but it is the most significant work. Dynamic modelling starts with the derivation of the kinematic equations. Before dealing with the kinematic equations, the reference frames of each gimbal describing the motion should be assigned properly which also establishes the transformation matrices. Kinematics describe the angular velocities and angular accelerations of the two axes stabilized system [10], [11].

In literature, there are two widely followed approaches to derive the dynamic equations of the system; Euler-Lagrangian formulation and Newton-Euler formulation [12]. While Lagrangian method provides a set of equations based on the energy calculation, Newton-Euler approach builds up the dynamic model on the balance of forces acting on the system by which observation of the internal dynamics in the equations may be more convenient. Thus, Newton-Euler method may be encountered mostly in the dynamic modelling of the stabilized gimbaled systems [13], [14], [15].

In this section, the kinematic modelling is studied and then the dynamics of the outer and inner gimbal are investigated via Newton-Euler approach including inertia tensors, motor torques, friction force, static and dynamic mass unbalance to be able to attain the required stabilization [11].

2.2 Reference Frames and Transformation Matrices

In this thesis, the gimballed antenna platform shown in Figure 2.1 is worked on. The body has two gimbals which can achieve angular motion around their own axes: inner gimbal and outer gimbal. For the antenna body, three reference frames are assigned as follows: The coordinate axes of the antenna frames are indicated in Figure 2.1:

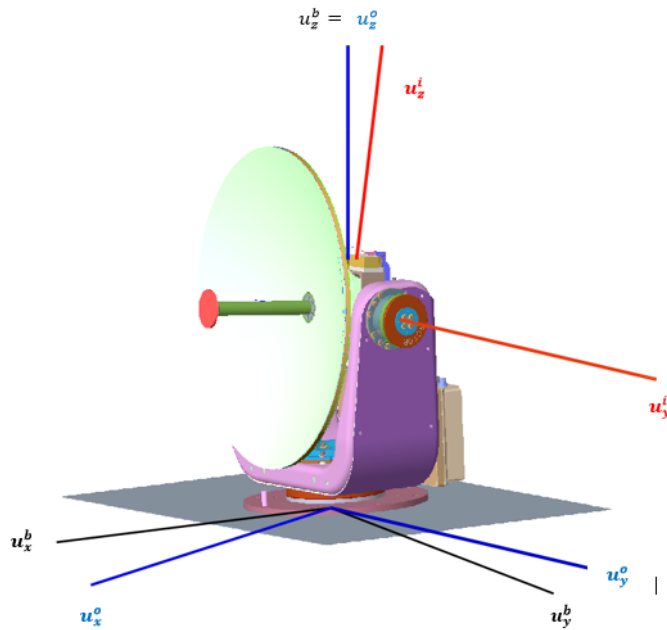


Figure 2.1: Frames of antenna body

Frame Base (F_b): Reference frame fixed to the antenna body with u_x^b, u_y^b, u_z^b axes,

Frame Outer (F_o): Reference frame fixed to the outer gimbal with u_x^o, u_y^o, u_z^o axes,

Frame Inner (F_i): Reference frame fixed to the inner gimbal with u_x^i, u_y^i, u_z^i axes.

Moreover, to handle the stabilization of the airborne antenna, we need to take the motion of unmanned aerial vehicle into consideration. To do that, we define additional three frames that implement the sequential angular motions, yaw (ψ), pitch (θ) and roll (ϕ), into whole movement. Those angles are called as Euler angles. Their assigned frames can be defined as follows:

Frame Earth (F_e): Reference frame fixed to the earth,

Frame C and Frame F (F_c and F_f): Intermediate reference frames between the earth

frame and the antenna body.

The transformation between the frames is shown in Figure 2.2.

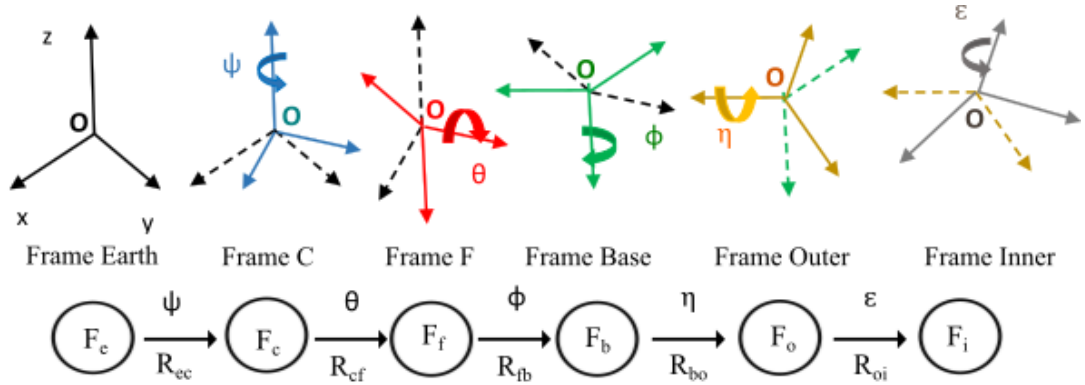


Figure 2.2: The transformations between the coordinates and frames

The unit vectors of all the frames are defined as

$$u_x = \begin{bmatrix} 1 \\ 0 \\ 0 \end{bmatrix}, u_y = \begin{bmatrix} 0 \\ 1 \\ 0 \end{bmatrix}, u_z = \begin{bmatrix} 0 \\ 0 \\ 1 \end{bmatrix} \quad (2.1)$$

If the Earth Frame (F_e) rotates around its z-axis by yaw-angle (ψ), a new frame whose x-axis and y-axis differs from the earth exists: Frame C (F_c). Similarly, when pitch-angle (θ) of rotation around y-axis of F_c occurs, the new unit vectors of Frame F (F_f) are defined. Finally, when we rotate F_f by roll-angle (ϕ) around its own x-axis, Frame Base (F_b), reference frame fixed to antenna body, is presented as shown in Figure 2.2.

As we come to the body, the rotation by azimuth-angle (η) around z-axis of F_b results in Frame Outer (F_o) that also describes the motion of the outer gimbal. That is why we can call z-axis of F_b or F_o as azimuth-axis. The angular motion of the inner gimbal is around y-axis of F_o , the elevation axis, by the elevation-angle (ϵ) which ends up with Frame Inner (F_i). Each rotation around an axis defines a transformation matrix between the frames explained so far.

In general case, the matrix “ R_{ij} ” point out the matrix that transforms of any vector in reference frame (i) to reference frame (j). In Figure 2.3, coordinate axes of the frame (i) and frame (j) are illustrated.

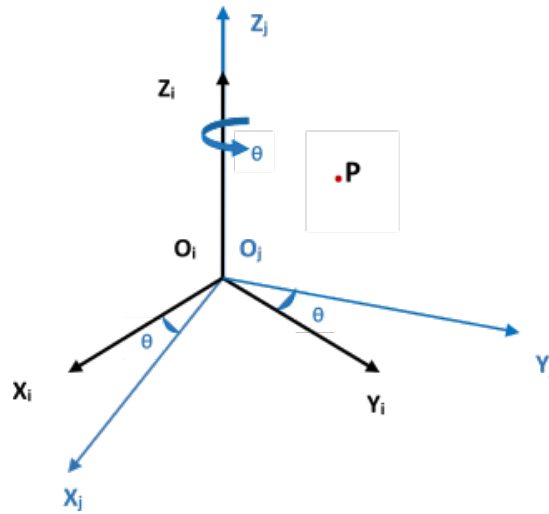


Figure 2.3: Coordinate axes

If we rotate frame (i) spanning R^3 whose unit vectors are (x_i, y_i, z_i) by θ -angle around its z-axis, there will exist an orientated frame, with unit vectors (x_j, y_j, z_j) . The position of the origins (o_i, o_j) are the same. The transformation between the frames relies on the rotation matrix “ R_{ij} ”.

To clarify the role of the rotation matrix, we concentrate on a point “ P ” in R^3 . The position vector of a point in a fixed reference frame is defined through the use of its unit vectors (i.e., basis vectors). Therefore, we can denote the point “ P ” via a position vector in each frame differently;

The position vector of “ P ” relative to frame (i): P^i ,

The position vector of “ P ” relative to frame (j): P^j .

The “ R_{ij} ” represents a coordinate transform and it gives the orientation of transformed frame relative to a fixed one. We can regard it as an operator satisfying the equation;

$$P^i = R_{ij} P^j \tag{2.2}$$

Here, it actually means that the position vector of any point in R^3 may be oriented relative to a fixed reference frame as long as the rotation or transformation matrix is assigned between the fixed and the oriented frame.

The transformations between the frames in Figure 2.2 are defined with the rotation matrices;

$$R_{ec}(\psi) = R_{ce}^T(\psi) = \begin{bmatrix} \cos\psi & -\sin\psi & 0 \\ \sin\psi & \cos\psi & 0 \\ 0 & 0 & 1 \end{bmatrix} \quad (2.3)$$

$$R_{cf}(\theta) = R_{fc}^T(\theta) = \begin{bmatrix} \cos\theta & 0 & \sin\theta \\ 0 & 1 & 0 \\ -\sin\theta & 0 & \cos\theta \end{bmatrix} \quad (2.4)$$

$$R_{fb}(\phi) = R_{bf}^T(\phi) = \begin{bmatrix} 1 & 0 & 0 \\ 0 & \cos\phi & -\sin\phi \\ 0 & \sin\phi & \cos\phi \end{bmatrix} \quad (2.5)$$

$$R_{bo}(\eta) = R_{ob}^T(\eta) = \begin{bmatrix} \cos\eta & -\sin\eta & 0 \\ \sin\eta & \cos\eta & 0 \\ 0 & 0 & 1 \end{bmatrix} \quad (2.6)$$

$$R_{oi}(\varepsilon) = R_{io}^T(\varepsilon) = \begin{bmatrix} \cos\varepsilon & 0 & \sin\varepsilon \\ 0 & 1 & 0 \\ -\sin\varepsilon & 0 & \cos\varepsilon \end{bmatrix} \quad (2.7)$$

2.3 Kinematic Equations

The kinematic equations will handle the definitions of angular velocities and then angular accelerations of outer, inner gimbals. The essential idea behind the kinematics can be considered as the derivative of the whole platform motion. The next step corresponds to the derivation of angular velocities to get angular accelerations of each

gimbal. All in all, the kinematic equations will allow us to work with Newton-Euler approach for dynamic modelling.

Before detailing the kinematic equations, some fundamental concepts may be revised which accounts about how to calculate the derivative of a transformation matrix. In [10] and [16], it is attributed to the property of the transformation matrix (T) in 2.8;

$$T^T T = I \quad (2.8)$$

This actually leads to the following derivation;

$$\frac{dT^T}{dt} + T^T \frac{dT}{dt} = 0 \quad (2.9)$$

In other words;

$$T^T \frac{dT}{dt} = -\frac{dT^T}{dt} T = -(T^T \frac{dT}{dt})^T \quad (2.10)$$

The term " $T^T \frac{dT}{dt}$ " is a skew symmetric matrix denoted by M_Ω where

$$M_\Omega = \begin{bmatrix} 0 & -\Omega_z & \Omega_y \\ \Omega_z & 0 & -\Omega_x \\ -\Omega_y & \Omega_x & 0 \end{bmatrix} \quad (2.11)$$

We may regard M_Ω as an operator whose input is angular velocity vector:

$$\Omega = \begin{bmatrix} \Omega_x \\ \Omega_y \\ \Omega_z \end{bmatrix} \quad (2.12)$$

Therefore, that ends up with the equation 2.13

$$\frac{dT}{dt} = M_\Omega .T \quad (2.13)$$

2.3.1 Angular Velocities

2.3.1.a Angular Velocity of the Outer Gimbal

In this section, angular velocity of the outer gimbal will be represented as a function of position. The combination of the displacement in each frame shown in Figure 2.2

establishes the equation for the gimbal. To deal with all the motion, the rate of change in position in each frame (F_e, F_c, F_f, F_b) is transformed to Frame Outer (F_o).

First, we express the angular velocity of the outer gimbal in Frame Outer (F_o) relative to Frame Earth (F_e), represented in Frame Outer (F_o) as: ω_{oe}

$$\omega_{oe} = \begin{bmatrix} \omega_{oe_x} \\ \omega_{oe_y} \\ \omega_{oe_z} \end{bmatrix}$$

$$\omega_{oe} = \omega_{ob} + \omega_{bf} + \omega_{fc} + \omega_{ce} \quad (2.14)$$

Equation 2.14 point outs that:

$$\omega_{oe} = \dot{\eta}u_z^o + \dot{\phi}u_x^b + \dot{\theta}u_y^f + \dot{\psi}u_z^c \quad (2.15)$$

where η is the angular displacement of the azimuth axis and

u_z^o : z-axis of Frame Outer(F_o),

u_x^b : x-axis of Frame Base(F_b),

u_y^f : y-axis of Frame F(F_f),

u_z^c : z-axis of Frame C(F_c).

Therefore,

$$\omega_{oe} = \dot{\eta}u_z + \dot{\phi} R_{ob} u_x + \dot{\theta} R_{of} u_y + \dot{\psi} R_{oc} u_z \quad (2.16)$$

where

$$R_{of} = R_{ob}R_{bf}$$

$$R_{oc} = R_{ob}R_{bf}R_{fc}$$

Therefore, Equation 2.16 turns out to be

$$\omega_{oe} = \dot{\eta}u_z + \dot{\phi} R_{ob} u_x + \dot{\theta} R_{ob} R_{bf} u_y + \dot{\psi} R_{ob} R_{bf} R_{fc} u_z \quad (2.17)$$

$$\omega_{oe} = \begin{bmatrix} \omega_{oe_x} \\ \omega_{oe_y} \\ \omega_{oe_z} \end{bmatrix} = \dot{\eta} \begin{bmatrix} 0 \\ 0 \\ 1 \end{bmatrix} + \dot{\phi} R_{ob} \begin{bmatrix} 1 \\ 0 \\ 0 \end{bmatrix} + \dot{\theta} R_{ob} R_{bf} \begin{bmatrix} 0 \\ 1 \\ 0 \end{bmatrix} + \dot{\psi} R_{ob} R_{bf} R_{fc} \begin{bmatrix} 0 \\ 0 \\ 1 \end{bmatrix} \quad (2.18)$$

2.3.1.b Angular Velocity of the Inner Gimbal

Similarly, the expression of the angular velocity for the inner gimbal is represented as ω_{ie} . The angular velocity of inner gimbal relative to Frame Earth (F_e) represented in Frame Inner (F_i) is expressed as:

$$\omega_{ie} = \begin{bmatrix} \omega_{ie_x} \\ \omega_{ie_y} \\ \omega_{ie_z} \end{bmatrix}$$

We can establish the relationship between the angular velocities ω_{ie} and ω_{oe} as

$$\omega_{ie} = \dot{\varepsilon} u_y^i + R_{io} \omega_{oe} \quad (2.19)$$

where ε is the angular displacement of inner gimbal and u_y^i is y-axis of Frame Inner (F_i). We can expand it in a detailed way as follows;

$$\omega_{ie} = \dot{\varepsilon} u_y + \dot{\eta} R_{io} u_z + \dot{\phi} R_{io} R_{ob} u_x + \dot{\theta} R_{io} R_{ob} R_{bf} u_y + \dot{\psi} R_{io} R_{ob} R_{bf} R_{fc} u_z \quad (2.20)$$

$$\begin{aligned} \omega_{ie} = \begin{bmatrix} \omega_{ie_x} \\ \omega_{ie_y} \\ \omega_{ie_z} \end{bmatrix} &= \dot{\varepsilon} \begin{bmatrix} 0 \\ 1 \\ 0 \end{bmatrix} + \dot{\eta} R_{io} \begin{bmatrix} 0 \\ 0 \\ 1 \end{bmatrix} + \dot{\phi} R_{io} R_{ob} \begin{bmatrix} 1 \\ 0 \\ 0 \end{bmatrix} + \dot{\theta} R_{io} R_{ob} R_{bf} \begin{bmatrix} 0 \\ 1 \\ 0 \end{bmatrix} \\ &+ \dot{\psi} R_{io} R_{ob} R_{bf} R_{fc} \begin{bmatrix} 0 \\ 0 \\ 1 \end{bmatrix} \end{aligned} \quad (2.21)$$

2.3.2 Angular Accelerations

Now, we focus on the acceleration terms of the 2-DOF antenna body. Basically, the acceleration can be obtained by taking time derivative of the angular velocity. In the previous section, we have discussed the equations of their angular velocities that are functions of angular displacements, relative to earth. In this section, the time derivatives of the velocities will be evaluated; these will results in determination of angular accelerations of the system. The calculations will bring about the derivatives of the rotation matrices. That is why it may be crucial to turn our attention to find them in the way described in Equation 2.13.

We start with R_{io} and continue on R_{ob} , R_{bf} , R_{fc} , R_{ce} , respectively;

$$\dot{R}_{io} = M_{\omega_{io}} R_{io} = \begin{bmatrix} 0 & -\omega_{ioz} & \omega_{ioy} \\ \omega_{ioz} & 0 & -\omega_{iox} \\ -\omega_{ioy} & \omega_{iox} & 0 \end{bmatrix} \begin{bmatrix} \cos\varepsilon & 0 & -\sin\varepsilon \\ 0 & 1 & 0 \\ \sin\varepsilon & 0 & \cos\varepsilon \end{bmatrix} \quad (2.22)$$

$$\dot{R}_{ob} = M_{\omega_{ob}} R_{ob} = \begin{bmatrix} 0 & -\omega_{obz} & \omega_{oby} \\ \omega_{obz} & 0 & -\omega_{obx} \\ -\omega_{oby} & \omega_{obx} & 0 \end{bmatrix} \begin{bmatrix} \cos\eta & \sin\eta & 0 \\ -\sin\eta & \cos\eta & 0 \\ 0 & 0 & 1 \end{bmatrix} \quad (2.23)$$

$$\dot{R}_{bf} = M_{\omega_{bf}} R_{bf} = \begin{bmatrix} 0 & -\omega_{bfz} & \omega_{bfy} \\ \omega_{bfz} & 0 & -\omega_{bfx} \\ -\omega_{bfy} & \omega_{bfx} & 0 \end{bmatrix} \begin{bmatrix} 1 & 0 & 0 \\ 0 & \cos\phi & \sin\phi \\ 0 & -\sin\phi & \cos\phi \end{bmatrix} \quad (2.24)$$

$$\dot{R}_{fc} = M_{\omega_{fc}} R_{fc} = \begin{bmatrix} 0 & -\omega_{fcz} & \omega_{fcy} \\ \omega_{fcz} & 0 & -\omega_{fcx} \\ -\omega_{fcy} & \omega_{fcx} & 0 \end{bmatrix} \begin{bmatrix} \cos\theta & 0 & -\sin\theta \\ 0 & 1 & 0 \\ \sin\theta & 0 & \cos\theta \end{bmatrix} \quad (2.25)$$

$$\dot{R}_{ce} = M_{\omega_{ce}} R_{ce} = \begin{bmatrix} 0 & -\omega_{cez} & \omega_{cey} \\ \omega_{cez} & 0 & -\omega_{cex} \\ -\omega_{cey} & \omega_{cex} & 0 \end{bmatrix} \begin{bmatrix} \cos\psi & \sin\psi & 0 \\ -\sin\psi & \cos\psi & 0 \\ 0 & 0 & 1 \end{bmatrix} \quad (2.26)$$

2.3.2.a Angular Acceleration of the Outer Gimbal

First, the angular acceleration of the outer body is represented as α_{oe} , which is the time derivative of ω_{oe} . We may denote it as;

$$\alpha_{oe} = \begin{bmatrix} \alpha_{oe_x} \\ \alpha_{oe_y} \\ \alpha_{oe_z} \end{bmatrix} \quad (2.27)$$

and

$$\alpha_{oe} = D_o \omega_{oe} \quad (2.28)$$

where D_o is the time derivative operator for the angular velocity of the outer gimbal. Consequently, the expression of the angular velocity of the outer body is expressed in Equation 2.17 as;

$$\begin{aligned} \alpha_{oe} = & \ddot{\eta} u_z \\ & + \ddot{\phi} R_{ob} u_x \\ & + \ddot{\theta} R_{ob} R_{bf} u_y \\ & + \ddot{\psi} R_{ob} R_{bf} R_{fc} u_z \\ & + \dot{\phi} \dot{R}_{ob} u_x \\ & + \dot{\theta} (\dot{R}_{ob} R_{bf} + R_{ob} \dot{R}_{bf}) u_y \\ & + \dot{\psi} (\dot{R}_{ob} R_{bf} R_{fc} + R_{ob} \dot{R}_{bf} R_{fc} + R_{ob} R_{bf} \dot{R}_{fc}) u_z \end{aligned} \quad (2.29)$$

The matrices \dot{R}_{ob} , \dot{R}_{bf} , \dot{R}_{fc} have already been defined previously.

2.3.2.b Angular Acceleration of the Inner Gimbal

Secondly, the equation of angular acceleration is attained by taking the time derivative of the angular velocity established in Equation 2.20:

$$\alpha_{ie} = D_i \omega_{ie} \quad (2.30)$$

where

$$\alpha_{ie} = \begin{bmatrix} \alpha_{ie_x} \\ \alpha_{ie_y} \\ \alpha_{ie_z} \end{bmatrix} \quad (2.31)$$

and D_i is the time derivative operator for the angular velocity of the inner body. Therefore, the angular velocity of the inner gimbal results in;

$$\begin{aligned}
\alpha_{ie} = & \ddot{\varepsilon} u_y \\
& + \ddot{\eta} R_{io} u_z \\
& + \ddot{\phi} R_{io} R_{ob} u_x \\
& + \ddot{\theta} R_{io} R_{ob} R_{bf} u_y \\
& + \ddot{\psi} R_{io} R_{ob} R_{bf} R_{fc} u_z \\
& + \dot{\eta} \dot{R}_{io} u_z \\
& + \dot{\phi} (\dot{R}_{io} R_{ob} + R_{io} \dot{R}_{ob}) u_x \\
& + \dot{\theta} (\dot{R}_{io} R_{ob} R_{bf} + R_{io} \dot{R}_{ob} R_{bf} + R_{io} R_{ob} \dot{R}_{bf}) u_y \\
& + \dot{\psi} (\dot{R}_{io} R_{ob} R_{bf} R_{fc} + R_{io} \dot{R}_{ob} R_{bf} R_{fc} + R_{io} R_{ob} \dot{R}_{bf} R_{fc} \\
& + R_{io} R_{ob} R_{bf} \dot{R}_{fc}) u_z
\end{aligned} \tag{2.32}$$

Again, we may figure out the matrices \dot{R}_{io} , \dot{R}_{ob} , \dot{R}_{bf} , \dot{R}_{fc} from the definitions at the beginning of the section. Now, we have obtained the kinematics of each gimbal of the antenna body that contributes us to achieve the dynamics of the system.

2.4 Dynamic Equations

The antenna platform we worked on is a 2-DOF stabilized plant that needs to be modelled and controlled effectively. To attain the solution, the dynamic equations of the gimbals should be formed, which include all the external forces, the kinematic disturbances and several nonlinearities as well [17].

In literature, the method for obtaining the dynamic equations vary with the complexity of the systems to be modelled. Euler-Lagrangian and Newton-Euler methods may be regarded as the common approaches for dynamic modelling. We can define the former one as a method which combines the energy-based equations that tackles the multi-body systems as a whole whereas the latter one, Newton-Euler method, is fundamentally based on the balance of the forces and torques. Within this method, the dynamic equations of each body or gimbal are written separately.

In Euler-Lagrangian approach, the constraint (inertial) forces are eliminated automatically that results in a compact set of equations including the torques and the displacements. On the other hand, Newton-Euler method contains all the acting forces and moments on each body in which also the coupling effects and the constraint forces are incorporated. Moreover, we may claim that it is easier and more systematic to derive the equations in Newton-Euler approach. Therefore, when these taken into consideration, Newton-Euler method is superior to Euler-Lagrangian regarding the simplicity in achieving the dynamic model of such a complex system [18].

Basically, Newton's dynamic equation figures out that;

$$\text{Sum of Forces} = \text{Variation of Linear Momentum} \quad (2.33)$$

whereas Euler's dynamic equation is based on;

$$\text{Sum of Torques} = \text{Variation of Angular Momentum} \quad (2.34)$$

In this section, we will work on Newton-Euler equation for each body by defining its constraint (inertial) and external torques acting on them.

2.4.1 Dynamic Equation of the Inner Gimbal

For the inner body, we can write the Newton's equation as

$$m_i a_i = F_{oi} + m_i g \quad (2.35)$$

In other words;

$$F_{oi} = m_i (a_i - g) \quad (2.36)$$

where

m_i : mass of the inner gimbal,

a_i : linear acceleration of the center of gravity of the inner gimbal,

F_{oi} : force applied by the outer gimbal on the inner gimbal,

g : gravity vector.

Euler's equation for the inner gimbal about the pivot point (the intersection of the rotational axes of Frame Inner (F_i) and Frame Outer (F_o)):

$$H^i = I_i \omega_{ie} \quad (2.37)$$

$$\Sigma\Gamma = \Delta H^i \quad (2.38)$$

$$\Sigma\Gamma = I_i \cdot \alpha_{ie} + \omega_{ie} \times (I_i \cdot \omega_{ie}) \quad (2.39)$$

$$I_i \cdot \alpha_{ie} + \omega_{ie} \times (I_i \cdot \omega_{ie}) = T_{oi} + r_{oc_i} \times (m_i g^i) \quad (2.40)$$

where

H^i : angular momentum of the inner gimbal,

$\Sigma\Gamma$: total torque acting on the inner gimbal,

ΔH^i : the variation of angular momentum of the inner gimbal,

I_i : inertia tensor of the inner gimbal about pivot point,

α_{ie} : angular acceleration of the inner gimbal relative to Frame Earth (F_e),

ω_{ie} : angular velocity of the inner gimbal relative to Frame Earth (F_e),

T_{oi} : moment applied by the outer gimbal on the inner gimbal,

r_{oc_i} : position vector from the pivot point to COG of the inner gimbal,

g^i : gravity vector transformed to Frame Inner (F_i) relative to Frame Earth (F_e).

We have look at each matrix included in Equation 2.40 in a detailed way. we have already worked on ω_{ie} and α_{ie} previously. First we start with inertia tensor of the inner gimbal denoted as I_i ;

$$I_i = \begin{bmatrix} I_{xx_i} & I_{xy_i} & I_{xz_i} \\ I_{yx_i} & I_{yy_i} & I_{yz_i} \\ I_{zx_i} & I_{zy_i} & I_{zz_i} \end{bmatrix} \quad (2.41)$$

The moment applied by the outer gimbal on the inner gimbal, T_{oi} , is a 3x1 matrix

representing external torques the inner body experiences;

$$T_{oi} = \begin{bmatrix} T_{oi_x} \\ T_{m_i} + T_{fr_i} \\ T_{oi_z} \end{bmatrix} \quad (2.42)$$

where T_{m_i} is the torque applied by the motor on the rotational axis of the inner gimbal. Furthermore, T_{fr_i} is the friction torque between the motor and the pivot point of the inner body. Therefore, the total external torque acting on the rotational axis or elevation axis of the Frame Inner (F_i) can be figured out as $T_{m_i} + T_{fr_i}$. Since the principal axis of the motion is the elevation axis, we will not pay attention to T_{oi_x} and T_{oi_z} . Additionally, r_{oc_i} , the position vector from the origin of the Frame Inner (F_i) to the center of the gravity of the inner gimbal is given by

$$r_{oc_i} = \begin{bmatrix} r_{oc_{ix}} \\ r_{oc_{iy}} \\ r_{oc_{iz}} \end{bmatrix} \quad (2.43)$$

Consequently, the term g^i should be concentrated on. The gravity vector in Frame Earth (F_e) can be defined as $-gu_z$. g^i is the gravity vector represented in Frame Inner (F_i) relative to Frame Earth (F_e). We can express it as;

$$g^i = -g \cdot (R_{io} R_{ob} R_{bf} R_{fc} R_{ce})u_z \quad (2.44)$$

Finally, we can write the Euler equation stated in Equation 2.40 in expanded form as

$$\begin{aligned} & \begin{bmatrix} I_{xx_i} & I_{xy_i} & I_{xz_i} \\ I_{yx_i} & I_{yy_i} & I_{yz_i} \\ I_{zx_i} & I_{zy_i} & I_{zz_i} \end{bmatrix} \cdot \begin{bmatrix} \alpha_{ie_x} \\ \alpha_{ie_y} \\ \alpha_{ie_z} \end{bmatrix} + \begin{bmatrix} \omega_{ie_x} \\ \omega_{ie_y} \\ \omega_{ie_z} \end{bmatrix} \times \left(\begin{bmatrix} I_{xx_i} & I_{xy_i} & I_{xz_i} \\ I_{yx_i} & I_{yy_i} & I_{yz_i} \\ I_{zx_i} & I_{zy_i} & I_{zz_i} \end{bmatrix} \cdot \begin{bmatrix} \omega_{ie_x} \\ \omega_{ie_y} \\ \omega_{ie_z} \end{bmatrix} \right) \\ & = \begin{bmatrix} T_{oi_x} \\ T_{m_i} + T_{fr_i} \\ T_{oi_z} \end{bmatrix} + \begin{bmatrix} r_{oc_{ix}} \\ r_{oc_{iy}} \\ r_{oc_{iz}} \end{bmatrix} \times m_i \begin{bmatrix} g_x^i \\ g_y^i \\ g_z^i \end{bmatrix} \end{aligned} \quad (2.45)$$

2.4.2 Dynamic Equation of the Outer Gimbal

For the outer body, we can state the Newton's equation;

$$(m_o + m_i)(a_{co} - g) = F_{bo} + F_{io} \quad (2.46)$$

Here we can note that $F_{io} = -F_{oi}$, which we have already figured out in Equation 2.36. Therefore Equation 2.46 results in

$$F_{bo} - F_{oi} = (m_o + m_i)(a_o - g) \quad (2.47)$$

where

F_{bo} : force applied by base of the platform on the outer gimbal,

F_{oi} : force applied by the outer gimbal on the inner gimbal,

m_o : mass of the outer gimbal,

m_i : mass of the inner gimbal,

a_o : linear acceleration of the center of gravity of the outer gimbal,

g : gravity vector.

Euler's equation for the outer gimbal about the pivot point (the intersection of the rotational axes of Frame Outer (F_i) and Frame Base (F_b)):

$$H^o = I_o \omega_{oe} + R_{oi} H^i \quad (2.48)$$

where H^i has already expressed in Equation 2.37. It means that the previous equation can be detailed as follows:

$$H^o = I_o \omega_{oe} + R_{oi} (I_i \omega_{ie}) \quad (2.49)$$

$$\Sigma \Gamma = \Delta H^o \quad (2.50)$$

$$\begin{aligned} \Sigma \Gamma = I_o \cdot \alpha_{oe} + \dot{R}_{oi} I_i \omega_{ie} + R_{oi} I_i \alpha_{ie} \\ + \omega_{oe} \times (I_o \omega_{oe} + R_{oi} (I_i \omega_{ie})) \end{aligned} \quad (2.51)$$

$$\begin{aligned} I_o \cdot \alpha_{oe} + \dot{R}_{oi} I_i \omega_{ie} + R_{oi} I_i \alpha_{ie} + \omega_{oe} \times (I_o \omega_{oe} + R_{oi} (I_i \omega_{ie})) \\ = T_{bo} + T_{io} + r_{oco} \times ((m_o + m_i) g^o) \end{aligned} \quad (2.52)$$

where

H^o : angular momentum of the outer gimbal,

R_{oi} : transformation matrix between Frame Outer (F_o) and Frame Inner (F_i),

$\Sigma\Gamma$: total torque acting on the outer gimbal,

ΔH^o : the variation of angular momentum of the outer gimbal,

I_i : inertia tensor of the inner gimbal about the pivot point,

I_o : inertia tensor of the outer gimbal about the pivot point,

α_{ie} : angular acceleration of the inner gimbal relative to Frame Earth (F_e),

α_{oe} : angular acceleration of the outer gimbal relative to Frame Earth (F_e),

ω_{ie} : angular velocity of the the inner gimbal relative to Frame Earth (F_e),

ω_{oe} : angular velocity of the outer gimbal relative to Frame Earth (F_e),

T_{bo} : moment applied by the platform base on the outer gimbal,

T_{io} : moment applied by the inner gimbal on the outer gimbal,

r_{oc_o} : position vector from the pivot point to COG of the outer gimbal,

g^o : gravity vector transformed to Frame Inner (F_o) relative to Frame Earth (F_e).

Now, we can turn our attention to each matrix included in Equation 2.52. The terms coming from the inner gimbal have already been handled. In this part we will concentrate on the matrices associated with the outer gimbal. ω_{oe} and α_{eo} have already been derived previously. First we start with the inertia tensor of the outer gimbal denoted as I_o ;

$$I_o = \begin{bmatrix} I_{xx_o} & I_{xy_o} & I_{xz_o} \\ I_{yx_o} & I_{yy_o} & I_{yz_o} \\ I_{zx_o} & I_{zy_o} & I_{zz_o} \end{bmatrix} \quad (2.53)$$

The moment applied by the inner gimbal on the outer gimbal, T_{io} , is a 3x1 matrix represented by

$$T_{io} = \begin{bmatrix} T_{io_x} \\ T_{io_y} \\ T_{fr_{iz}} \end{bmatrix} \quad (2.54)$$

Here in Equation 2.54 , $T_{fr_{iz}}$ is the transformed friction torque to azimuth axis, the principal rotational axis, between inner and outer gimbals. T_{io_x} and T_{io_y} will not be

taken into consideration since the only motion takes place on the azimuth axis. The moment applied by the base of the platform on the outer gimbal, T_{bo} can be written as follows:

$$T_{bo} = \begin{bmatrix} T_{bo_x} \\ T_{bo_y} \\ T_{m_o} + T_{fr_o} \end{bmatrix} \quad (2.55)$$

where T_{m_o} is the torque applied by the motor on the rotational axis of the outer gimbal. Furthermore, T_{fr_o} is the friction torque between the motor and the pivot point of the outer body. Therefore, the total external torque acting on the rotational axis or the azimuth axis of the Frame Outer (F_o) can be expressed as $T_{m_o} + T_{fr_o}$. Similarly, as the principal axis of the motion is the azimuth axis, T_{bo_x} and T_{bo_y} have become irrelevant. Furthermore, r_{oc_o} , the position vector from the origin of the Frame Inner (F_o) to the center of the gravity of the outer body represented as

$$r_{oc_o} = \begin{bmatrix} r_{oc_o_x} \\ r_{oc_o_y} \\ r_{oc_o_z} \end{bmatrix} \quad (2.56)$$

g^o is the gravity vector represented in Frame Outer (F_o) relative to Frame Earth (F_e). Therefore, it can be expressed as

$$g^o = -g \cdot (R_{ob} R_{bf} R_{fc} R_{ce})u_z \quad (2.57)$$

Then Euler's equation stated in Equation 2.52 may be detailed as;

$$\begin{aligned}
& \begin{bmatrix} I_{xx_o} & I_{xy_o} & I_{xz_o} \\ I_{yx_o} & I_{yy_o} & I_{yz_o} \\ I_{zx_o} & I_{zy_o} & I_{zz_o} \end{bmatrix} \cdot \begin{bmatrix} \alpha_{oe_x} \\ \alpha_{oe_y} \\ \alpha_{oe_z} \end{bmatrix} + \begin{bmatrix} \cos\varepsilon & 0 & \sin\varepsilon \\ 0 & 1 & 0 \\ -\sin\varepsilon & 0 & \cos\varepsilon \end{bmatrix} \cdot \begin{bmatrix} I_{xx_i} & I_{xy_i} & I_{xz_i} \\ I_{yx_i} & I_{yy_i} & I_{yz_i} \\ I_{zx_i} & I_{zy_i} & I_{zz_i} \end{bmatrix} \cdot \begin{bmatrix} \alpha_{ie_x} \\ \alpha_{ie_y} \\ \alpha_{ie_z} \end{bmatrix} \\
& + \begin{bmatrix} -\sin\varepsilon & 0 & \cos\varepsilon \\ 0 & 0 & 0 \\ -\cos\varepsilon & 0 & -\sin\varepsilon \end{bmatrix} \cdot \begin{bmatrix} I_{xx_i} & I_{xy_i} & I_{xz_i} \\ I_{yx_i} & I_{yy_i} & I_{yz_i} \\ I_{zx_i} & I_{zy_i} & I_{zz_i} \end{bmatrix} \cdot \begin{bmatrix} \omega_{ie_x} \\ \omega_{ie_y} \\ \omega_{ie_z} \end{bmatrix} \\
& + \begin{bmatrix} \omega_{oe_x} \\ \omega_{oe_y} \\ \omega_{oe_z} \end{bmatrix} \times \left(\begin{bmatrix} I_{xx_o} & I_{xy_o} & I_{xz_o} \\ I_{yx_o} & I_{yy_o} & I_{yz_o} \\ I_{zx_o} & I_{zy_o} & I_{zz_o} \end{bmatrix} \cdot \begin{bmatrix} \omega_{oe_x} \\ \omega_{oe_y} \\ \omega_{oe_z} \end{bmatrix} \right. \\
& \left. + \begin{bmatrix} \cos\varepsilon & 0 & \sin\varepsilon \\ 0 & 1 & 0 \\ -\sin\varepsilon & 0 & \cos\varepsilon \end{bmatrix} \cdot \begin{bmatrix} I_{xx_i} & I_{xy_i} & I_{xz_i} \\ I_{yx_i} & I_{yy_i} & I_{yz_i} \\ I_{zx_i} & I_{zy_i} & I_{zz_i} \end{bmatrix} \cdot \begin{bmatrix} \omega_{ie_x} \\ \omega_{ie_y} \\ \omega_{ie_z} \end{bmatrix} \right) \\
& = \begin{bmatrix} T_{io_x} \\ T_{io_y} \\ T_{fr_{iz}} \end{bmatrix} + \begin{bmatrix} T_{bo_x} \\ T_{bo_y} \\ T_{m_o} + T_{fr_o} \end{bmatrix} + \begin{bmatrix} r_{oc_{ox}} \\ r_{oc_{oy}} \\ r_{oc_{oz}} \end{bmatrix} \times (m_i + m_o) \begin{bmatrix} g_x^o \\ g_y^o \\ g_z^o \end{bmatrix}
\end{aligned}$$

(2.58)

CHAPTER 3

DYNAMIC AND STATIC MASS UNBALANCE

3.1 Introduction

The purpose of two axes gimballed system, antenna body, is to provide a stabilization for the link between antenna and the satellite it communicates. The gimballed assembly experiences the disturbance resulting from external environment and body motions. In such systems, the most significant disturbance sources are the platform angular motion, the dynamics of the gimballed system and the gimbal mass unbalance. That is why it has a great importance to implement all the dynamics of the system in order to enhance the accuracy of the stabilization [19].

The two axes gimballed systems have been studied with different methods in many cases in which each gimbal is balanced and responsible for only its rotational axis. Those approaches simplify the kinematic and dynamic equations of the plant because it is assumed that the rigid body called as the gimbal has no mass unbalance when the equations of the motion are obtained [20]. For instance, the dynamic equations of the two axes gimballed system have been obtained by assuming that mass distribution is symmetrical and the system has no dynamic disturbances in [21]. Similarly, nonlinear disturbances coming from mass unbalance have been ignored to simplify the design and to reduce the cost in [22]. Moreover, it is argued that the mass properties of the gimbals play a role in stabilization platform; however, it may result in a costly and time-consuming production in [23].

Additionally, in most studies, the azimuth and the elevation axes are assumed to be identical and decoupled; therefore, each of them is implemented separately. That

leads to ignoring the coupling effects, a source of disturbance caused by base angular motion and internal dynamics of the system, between the gimbals. However, to attain a more stable operation and to guarantee a more accurate stabilization, cross coupling between the gimbals, the dynamics of the system, dynamic mass unbalance, and the static mass unbalance should be expressed in plant dynamics [24] .

In this section, the dynamic mass unbalance and the static mass unbalance will be derived from the dynamic equations obtained previously. By considering the cross coupling, the effect of the base angular motion, how much mass unbalance will influence the system will be investigated.

3.2 Dynamic Mass Unbalance

Dynamic mass unbalance results from the unsymmetrical mass distribution called as "Product of Inertia (POI)". We can attribute it with the inertia matrix [24], [23]. When a rigid body has a symmetrical mass distribution with respect to the frame axes, non principal diagonal elements of the inertia matrix are zero; therefore, the inertia matrix is diagonal and the rigid body has no dynamic mass unbalance. In the antenna platform we work on, the inertia matrices of the gimbals are not diagonal; in other words, the plant experiences the dynamic mass unbalance.

3.2.1 Dynamic Mass Unbalance of the Inner Gimbal

We have already figure out Euler's equation for the inner gimbal in Equation 2.40.

$$\begin{aligned} & \begin{bmatrix} I_{xx_i} & I_{xy_i} & I_{xz_i} \\ I_{yx_i} & I_{yy_i} & I_{yz_i} \\ I_{zx_i} & I_{zy_i} & I_{zz_i} \end{bmatrix} \cdot \begin{bmatrix} \alpha_{ie_x} \\ \alpha_{ie_y} \\ \alpha_{ie_z} \end{bmatrix} + \begin{bmatrix} \omega_{ie_x} \\ \omega_{ie_y} \\ \omega_{ie_z} \end{bmatrix} \times \left(\begin{bmatrix} I_{xx_i} & I_{xy_i} & I_{xz_i} \\ I_{yx_i} & I_{yy_i} & I_{yz_i} \\ I_{zx_i} & I_{zy_i} & I_{zz_i} \end{bmatrix} \cdot \begin{bmatrix} \omega_{ie_x} \\ \omega_{ie_y} \\ \omega_{ie_z} \end{bmatrix} \right) \\ &= \begin{bmatrix} T_{oi_x} \\ T_{m_i} + T_{fr_i} \\ T_{oi_z} \end{bmatrix} + \begin{bmatrix} r_{oc_{i_x}} \\ r_{oc_{i_y}} \\ r_{oc_{i_z}} \end{bmatrix} \times m_i \begin{bmatrix} g_x^i \\ g_y^i \\ g_z^i \end{bmatrix} \end{aligned}$$

It can be written in a more detailed way as follows:

$$\begin{aligned} & \begin{bmatrix} I_{xx_i}\alpha_{ie_x} + I_{xy_i}\alpha_{ie_y} + I_{xz_i}\alpha_{ie_z} \\ I_{yx_i}\alpha_{ie_x} + I_{yy_i}\alpha_{ie_y} + I_{yz_i}\alpha_{ie_z} \\ I_{zx_i}\alpha_{ie_x} + I_{zy_i}\alpha_{ie_y} + I_{zz_i}\alpha_{ie_z} \end{bmatrix} + \begin{bmatrix} \omega_{ie_x} \\ \omega_{ie_y} \\ \omega_{ie_z} \end{bmatrix} \times \left(\begin{bmatrix} I_{xx_i}\omega_{ie_x} + I_{xy_i}\omega_{ie_y} + I_{xz_i}\omega_{ie_z} \\ I_{yx_i}\omega_{ie_x} + I_{yy_i}\omega_{ie_y} + I_{yz_i}\omega_{ie_z} \\ I_{zx_i}\omega_{ie_x} + I_{zy_i}\omega_{ie_y} + I_{zz_i}\omega_{ie_z} \end{bmatrix} \right) \\ &= \begin{bmatrix} T_{oi_x} \\ T_{m_i} + T_{fr_i} \\ T_{oi_z} \end{bmatrix} + \begin{bmatrix} r_{oc_{i_x}} \\ r_{oc_{i_y}} \\ r_{oc_{i_z}} \end{bmatrix} \times m_i \begin{bmatrix} g_x^i \\ g_y^i \\ g_z^i \end{bmatrix} \end{aligned}$$

When we carry out the Euler's method, we will end up with three equations that describe the dynamics of the inner gimbal. However, since the principal axis of the motion is elevation, the equation derived for y-axis is regarded as the dynamic equation of the inner gimbal, which is stated in Equation 3.1 as follows:

$$\begin{aligned} & (I_{yx_i}\alpha_{ie_x} + I_{yy_i}\alpha_{ie_y} + I_{yz_i}\alpha_{ie_z}) + \omega_{ie_z} (I_{xx_i}\omega_{ie_x} + I_{xy_i}\omega_{ie_y} + I_{xz_i}\omega_{ie_z}) - \\ & \omega_{ie_x} (I_{zx_i}\omega_{ie_x} + I_{zy_i}\omega_{ie_y} + I_{zz_i}\omega_{ie_z}) = T_{m_i} + T_{fr_i} + m_i (r_{oc_{i_z}}g_x^i - g_z^i r_{oc_{i_x}}) \end{aligned} \quad (3.1)$$

Each term in Equation 3.1 that is the multiplication of any element except for diagonal ones in the inertia tensor can be related to the dynamic mass unbalance for the inner gimbal. The moment transferred to y-axis (I_{yy_i}) of the gimbal creates the angular acceleration ($\alpha_i e$). That acceleration may be considered as the source of the angular motion we attempt to control. Therefore, we may arrange Equation 3.1 as follows such that we can clarify what the role of dynamic mass unbalance is in the dynamic Equation 3.2.

$$I_{yy_i}\alpha_{ie_y} + T_{DynMass_y} = T_{m_i} + T_{fr_i} + m_i (r_{oc_{i_z}}g_x^i - g_z^i r_{oc_{i_x}}) \quad (3.2)$$

where

$$T_{DynMass_y} = I_{yx_i} \alpha_{ie_x} + I_{yz_i} \alpha_{ie_z} + \omega_{ie_z} (I_{xx_i} \omega_{ie_x} + I_{xy_i} \omega_{ie_y} + I_{xz_i} \omega_{ie_z}) \\ - \omega_{ie_x} (I_{zx_i} \omega_{ie_x} + I_{zy_i} \omega_{ie_y} + I_{zz_i} \omega_{ie_z})$$

3.2.2 Dynamic Mass Unbalance of the Outer Gimbal

Similarly, we have expressed the Euler's equation for outer body in Equation 2.52.

$$\begin{aligned} & \begin{bmatrix} I_{xx_o} & I_{xy_o} & I_{xz_o} \\ I_{yx_o} & I_{yy_o} & I_{yz_o} \\ I_{zx_o} & I_{zy_o} & I_{zz_o} \end{bmatrix} \cdot \begin{bmatrix} \alpha_{oe_x} \\ \alpha_{oe_y} \\ \alpha_{oe_z} \end{bmatrix} + \begin{bmatrix} \cos \varepsilon & 0 & \sin \varepsilon \\ 0 & 1 & 0 \\ -\sin \varepsilon & 0 & \cos \varepsilon \end{bmatrix} \cdot \begin{bmatrix} I_{xx_i} & I_{xy_i} & I_{xz_i} \\ I_{yx_i} & I_{yy_i} & I_{yz_i} \\ I_{zx_i} & I_{zy_i} & I_{zz_i} \end{bmatrix} \cdot \begin{bmatrix} \alpha_{ie_x} \\ \alpha_{ie_y} \\ \alpha_{ie_z} \end{bmatrix} \\ & + \begin{bmatrix} -\sin \varepsilon & 0 & \cos \varepsilon \\ 0 & 0 & 0 \\ -\cos \varepsilon & 0 & -\sin \varepsilon \end{bmatrix} \cdot \begin{bmatrix} I_{xx_i} & I_{xy_i} & I_{xz_i} \\ I_{yx_i} & I_{yy_i} & I_{yz_i} \\ I_{zx_i} & I_{zy_i} & I_{zz_i} \end{bmatrix} \cdot \begin{bmatrix} \omega_{ie_x} \\ \omega_{ie_y} \\ \omega_{ie_z} \end{bmatrix} \\ & + \begin{bmatrix} \omega_{oe_x} \\ \omega_{oe_y} \\ \omega_{oe_z} \end{bmatrix} \times \left(\begin{bmatrix} I_{xx_o} & I_{xy_o} & I_{xz_o} \\ I_{yx_o} & I_{yy_o} & I_{yz_o} \\ I_{zx_o} & I_{zy_o} & I_{zz_o} \end{bmatrix} \cdot \begin{bmatrix} \omega_{oe_x} \\ \omega_{oe_y} \\ \omega_{oe_z} \end{bmatrix} \right. \\ & \left. + \begin{bmatrix} \cos \varepsilon & 0 & \sin \varepsilon \\ 0 & 1 & 0 \\ -\sin \varepsilon & 0 & \cos \varepsilon \end{bmatrix} \cdot \begin{bmatrix} I_{xx_i} & I_{xy_i} & I_{xz_i} \\ I_{yx_i} & I_{yy_i} & I_{yz_i} \\ I_{zx_i} & I_{zy_i} & I_{zz_i} \end{bmatrix} \cdot \begin{bmatrix} \omega_{ie_x} \\ \omega_{ie_y} \\ \omega_{ie_z} \end{bmatrix} \right) \\ & = \begin{bmatrix} T_{io_x} \\ T_{io_y} \\ T_{fr_{iz}} \end{bmatrix} + \begin{bmatrix} T_{bo_x} \\ T_{bo_y} \\ T_{m_o} + T_{fr_o} \end{bmatrix} + \begin{bmatrix} r_{oc_{ox}} \\ r_{oc_{oy}} \\ r_{oc_{oz}} \end{bmatrix} \times (m_i + m_o) \begin{bmatrix} g_x^o \\ g_y^o \\ g_z^o \end{bmatrix} \end{aligned}$$

Equation 2.52 can be expanded as

$$\begin{aligned}
& \begin{bmatrix} I_{xx_o} \alpha_{oe_x} + I_{xy_o} \alpha_{oe_y} + I_{xz_o} \alpha_{oe_z} \\ I_{yx_o} \alpha_{oe_x} + I_{yy_o} \alpha_{oe_y} + I_{yz_o} \alpha_{oe_z} \\ I_{zx_o} \alpha_{oe_x} + I_{zy_o} \alpha_{oe_y} + I_{zz_o} \alpha_{oe_z} \end{bmatrix} \\
& + \begin{bmatrix} \cos \varepsilon (I_{xx_i} \alpha_{ie_x} + I_{xy_i} \alpha_{ie_y} + I_{xz_i} \alpha_{ie_z}) + \sin \varepsilon (I_{zx_i} \alpha_{ie_x} + I_{zy_i} \alpha_{ie_y} + I_{zz_i} \alpha_{ie_z}) \\ I_{yx_i} \alpha_{ie_x} + I_{yy_i} \alpha_{ie_y} + I_{yz_i} \alpha_{ie_z} \\ -\sin \varepsilon (I_{xx_i} \alpha_{ie_x} + I_{xy_i} \alpha_{ie_y} + I_{xz_i} \alpha_{ie_z}) + \cos \varepsilon (I_{zx_i} \alpha_{ie_x} + I_{zy_i} \alpha_{ie_y} + I_{zz_i} \alpha_{ie_z}) \end{bmatrix} \\
& + \begin{bmatrix} -\sin \varepsilon (I_{xx_i} \omega_{ie_x} + I_{xy_i} \omega_{ie_y} + I_{xz_i} \omega_{ie_z}) + \cos \varepsilon (I_{zx_i} \omega_{ie_x} + I_{zy_i} \omega_{ie_y} + I_{zz_i} \omega_{ie_z}) \\ 0 \\ -\cos \varepsilon (I_{xx_i} \omega_{ie_x} + I_{xy_i} \omega_{ie_y} + I_{xz_i} \omega_{ie_z}) - \sin \varepsilon (I_{zx_i} \omega_{ie_x} + I_{zy_i} \omega_{ie_y} + I_{zz_i} \omega_{ie_z}) \end{bmatrix} \\
& + \begin{bmatrix} \omega_{oe_x} \\ \omega_{oe_y} \\ \omega_{oe_z} \end{bmatrix} \times \begin{bmatrix} I_{xx_o} \omega_{oe_x} + I_{xy_o} \omega_{oe_y} + I_{xz_o} \omega_{oe_z} \\ I_{yx_o} \omega_{oe_x} + I_{yy_o} \omega_{oe_y} + I_{yz_o} \omega_{oe_z} \\ I_{zx_o} \omega_{oe_x} + I_{zy_o} \omega_{oe_y} + I_{zz_o} \omega_{oe_z} \end{bmatrix} \\
& + \begin{bmatrix} \cos \varepsilon (I_{xx_i} \omega_{ie_x} + I_{xy_i} \omega_{ie_y} + I_{xz_i} \omega_{ie_z}) + \sin \varepsilon (I_{zx_i} \omega_{ie_x} + I_{zy_i} \omega_{ie_y} + I_{zz_i} \omega_{ie_z}) \\ I_{yx_i} \omega_{ie_x} + I_{yy_i} \omega_{ie_y} + I_{yz_i} \omega_{ie_z} \\ -\sin \varepsilon (I_{xx_i} \omega_{ie_x} + I_{xy_i} \omega_{ie_y} + I_{xz_i} \omega_{ie_z}) + \cos \varepsilon (I_{zx_i} \omega_{ie_x} + I_{zy_i} \omega_{ie_y} + I_{zz_i} \omega_{ie_z}) \end{bmatrix} \\
& = \begin{bmatrix} T_{io_x} \\ T_{io_y} \\ T_{friz} \end{bmatrix} + \begin{bmatrix} T_{bo_x} \\ T_{bo_y} \\ T_{m_o} + T_{fr_o} \end{bmatrix} + \begin{bmatrix} r_{oc_o_x} \\ r_{oc_o_y} \\ r_{oc_o_z} \end{bmatrix} \times (m_i + m_o) \begin{bmatrix} g_x^o \\ g_y^o \\ g_z^o \end{bmatrix}
\end{aligned}$$

As we seek a solution to this equation, three equations that define the dynamics of each axis of the outer frame are reached. Since the rotational axis of the body is the azimuth axis, the last row of the solution matrix will be concentrated on, which is represented in Equation 3.3.

$$\begin{aligned}
& I_{zx_o} \alpha_{oe_x} + I_{zy_o} \alpha_{oe_y} + I_{zz_o} \alpha_{oe_z} - \sin \varepsilon (I_{xx_i} \alpha_{ie_x} + I_{xy_i} \alpha_{ie_y} + I_{xz_i} \alpha_{ie_z}) + \\
& \cos \varepsilon (I_{zx_i} \alpha_{ie_x} + I_{zy_i} \alpha_{ie_y} + I_{zz_i} \alpha_{ie_z}) - \cos \varepsilon (I_{xx_i} \omega_{ie_x} + I_{xy_i} \omega_{ie_y} + I_{xz_i} \omega_{ie_z}) \\
& - \sin \varepsilon (I_{zx_i} \omega_{ie_x} + I_{zy_i} \omega_{ie_y} + I_{zz_i} \omega_{ie_z}) + \omega_{oe_x} (I_{yx_o} \omega_{oe_x} + I_{yy_o} \omega_{oe_y} + I_{yz_o} \omega_{oe_z} + I_{yx_i} \\
& \omega_{ie_x} + I_{yy_i} \omega_{ie_y} + I_{yz_i} \omega_{ie_z}) - \omega_{oe_y} (I_{xx_o} \omega_{oe_x} + I_{xy_o} \omega_{oe_y} + I_{xz_o} \omega_{oe_z} + \\
& \cos \varepsilon (I_{xx_i} \omega_{ie_x} + I_{xy_i} \omega_{ie_y} + I_{xz_i} \omega_{ie_z}) + \sin \varepsilon (I_{zx_i} \omega_{ie_x} + I_{zy_i} \omega_{ie_y} + I_{zz_i} \omega_{ie_z})) \\
& = T_{m_o} + T_{fr_o} + T_{friz} + (m_o + m_i) (r_{oc_o_x} g_y^o - g_x^o r_{oc_o_y})
\end{aligned} \tag{3.3}$$

Again, each term in Equation 3.3 that is the multiplication of any element except for diagonal ones in the inertia tensor can be related to the dynamic mass unbalance for the outer gimbal. The torque applied to z-axis (I_{zz_o}) of the gimbal results in the angular acceleration ($\alpha_o e$). The acceleration ($\alpha_o e$) leads to the angular motion of the outer gimbal. Consequently, we may figure out from Equation 3.3 that we can understand what the role of dynamic mass unbalance is in the dynamic Equation 3.4.

$$I_{zz_o} \alpha_{oe_z} + T_{DynMass_z} = T_{m_o} + T_{fr_o} + T_{fr_{iz}} + (m_o + m_i)(r_{oc_{ox}} g_y^o - g_x^o r_{oc_{oy}}) \quad (3.4)$$

where

$$\begin{aligned} T_{DynMass_z} = & I_{zx_o} \alpha_{oe_x} + I_{zy_o} \alpha_{oe_y} - \sin \varepsilon (I_{xx_i} \alpha_{ie_x} + I_{xy_i} \alpha_{ie_y} + I_{xz_i} \alpha_{ie_z}) + \\ & \cos \varepsilon (I_{zx_i} \alpha_{ie_x} + I_{zy_i} \alpha_{ie_y} + I_{zz_i} \alpha_{ie_z}) - \cos \varepsilon (I_{xx_i} \omega_{ie_x} + I_{xy_i} \omega_{ie_y} + I_{xz_i} \omega_{ie_z}) \\ & - \sin \varepsilon (I_{zx_i} \omega_{ie_x} + I_{zy_i} \omega_{ie_y} + I_{zz_i} \omega_{ie_z}) + \omega_{oe_x} (I_{yx_o} \omega_{oe_x} + I_{yy_o} \omega_{oe_y} + I_{yz_o} \omega_{oe_z} + I_{yx_i} \\ & \omega_{ie_x} + I_{yy_i} \omega_{ie_y} + I_{yz_i} \omega_{ie_z}) - \omega_{oe_y} (I_{xx_o} \omega_{oe_x} + I_{xy_o} \omega_{oe_y} + I_{xz_o} \omega_{oe_z} + \\ & \cos \varepsilon (I_{xx_i} \omega_{ie_x} + I_{xy_i} \omega_{ie_y} + I_{xz_i} \omega_{ie_z}) + \sin \varepsilon (I_{zx_i} \omega_{ie_x} + I_{zy_i} \omega_{ie_y} + I_{zz_i} \omega_{ie_z})) \end{aligned}$$

3.2.3 Simulation Results

3.2.3.a Simulation Construction

To understand the effect of the dynamic mass unbalance on the system, the path described in [19] is followed. For this purpose, we will come up with the stabilization loops for the azimuth and the elevation axes that include PI controllers so that we can attain constant velocity control.

Throughout the simulations, angular velocities of each frame are attempted to be kept constant as this is the case in [19]. The dynamic mass unbalance for each gimbal expressed previously is implemented in MATLAB and Simulink environment with these stabilization loops, which is indicated in Figure 3.1.

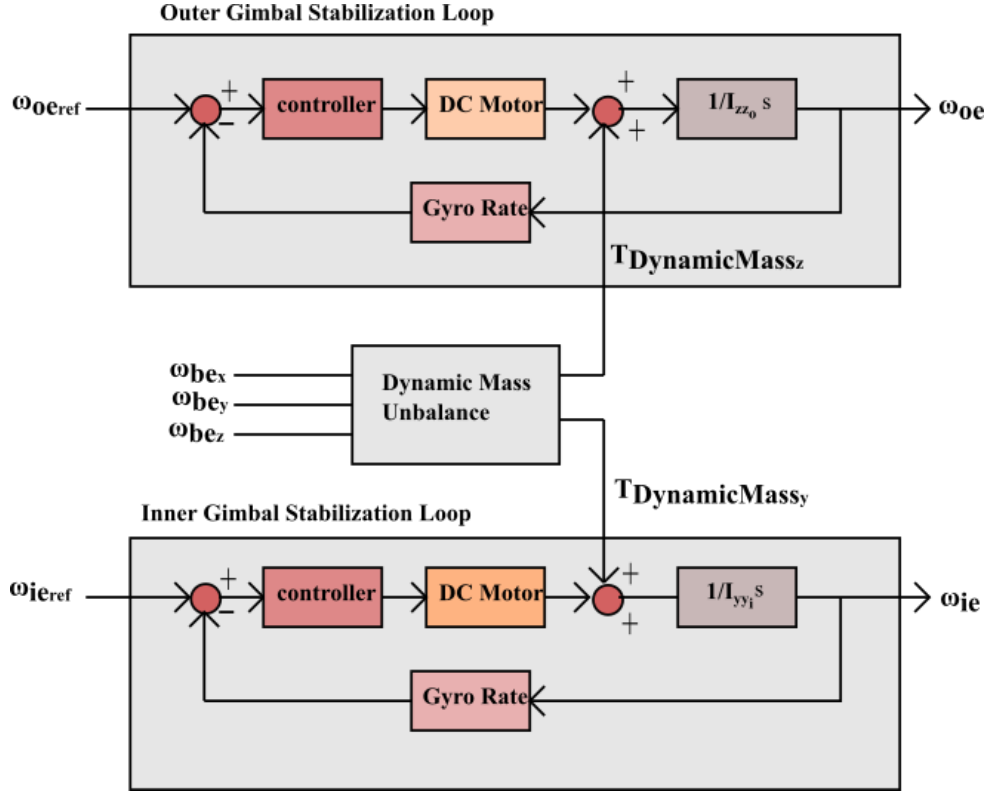


Figure 3.1: Stabilization loops for outer and inner gimbals

In Figure 3.1, each loop is established by combining a PI controller, a DC motor model, a gyro model giving the loop a velocity feedback. For the DC motor model, the basic block diagram in [24] is implemented via the motor characteristics specified by ASELSAN that also provides the gyro transfer function directly. The values of parameters belonging to the gimbals can be found in Appendix. This model also includes the cross coupling between the azimuth and the elevation axes, which is implemented in "Dynamic Mass Unbalance" block.

The inputs and the outputs of the stabilization loops can be described as:

$\omega_{oe,ref}$: Reference angular velocity input for the outer gimbal,

$\omega_{ie,ref}$: Reference angular velocity input for the inner gimbal,

ω_{be} : The angular velocity of the platform relative to Frame Earth (F_e),

ω_{oe} : The angular velocity of outer gimbal relative to Frame Earth (F_e),

ω_{ie} : The angular velocity of inner gimbal relative to Frame Earth (F_e),

$T_{DynMass_z}$: The disturbance due to dynamic mass unbalance induced on the outer gimbal,

$T_{DynMass_y}$: The disturbance due to dynamic mass unbalance induced on the inner gimbal.

The simulations have been conducted with different cases in which the angular velocity of the platform is adjusted to different values. These cases are listed in Table 3.1.

Table 3.1: Different test cases with varying angular velocity of the platform

Case	The Angular Velocity of the Platform		
	ω_{be_x} (deg/s)	ω_{be_y} (deg/s)	ω_{be_z} (deg/s)
Case 1	0	0	0
Case 2	30	30	30
Case 3	30	60	60
Case 4	60	60	60
Case 5	60	75	85

3.2.3.b Simulation Results of the Outer Gimbal

As explained in the previous section, a PI controller has been implemented for constant velocity control. We can note the transfer function of it as:

$$G_{outer} = K_p + \frac{K_i}{s}$$

where $K_p = 20$ and $K_i = 50$. Therefore, the transfer function of the controller may be expressed in Equation 3.5.

$$G_{outer} = 20 + \frac{50}{s} \quad (3.5)$$

Here the purpose is to observe how dynamic mass unbalance resulting from different test scenarios listed in Table 3.1 affects the operation of the constant velocity control. When there is no mass unbalance and friction, the PI parameters specified achieve stable operation which can be concluded from Figure 3.2.

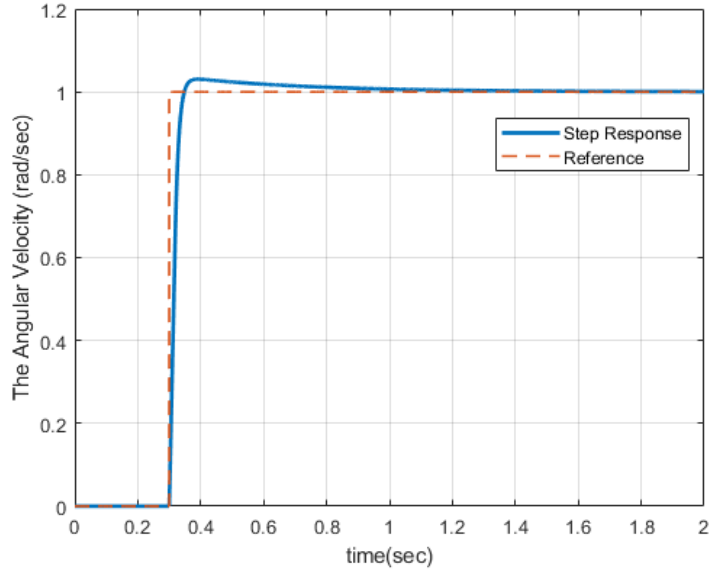


Figure 3.2: Step response of the azimuth axis

In Figure 3.2, step response of the angular velocity of the outer gimbal is depicted when there is no disturbance. To understand the effect of the dynamic mass unbalance, we have conducted the test conditions listed in Table 3.1 with two different constant velocities for the outer gimbal whereas the ω_{ie} is taken as 0.05 rad/sec, a low velocity for each case to see the cross coupling effect as well.

First, the reference angular velocity is adjusted to 0.1 rad/sec while the disturbance coming from the platform varying according to Table 3.1 and the results are observed. By changing the reference to a higher value, 0.5 rad/sec, we aimed to see how the dynamic mass unbalance of outer body influences the system response at a higher constant velocity operation.

i. $\omega_{oe_{ref}} = 0.1$ rad/sec

In this section, $\omega_{oe_{ref}} = 0.1$ rad/sec (about 6 deg/sec) is selected as a low velocity and the simulation has been done. The results can be seen in Figure 3.3.

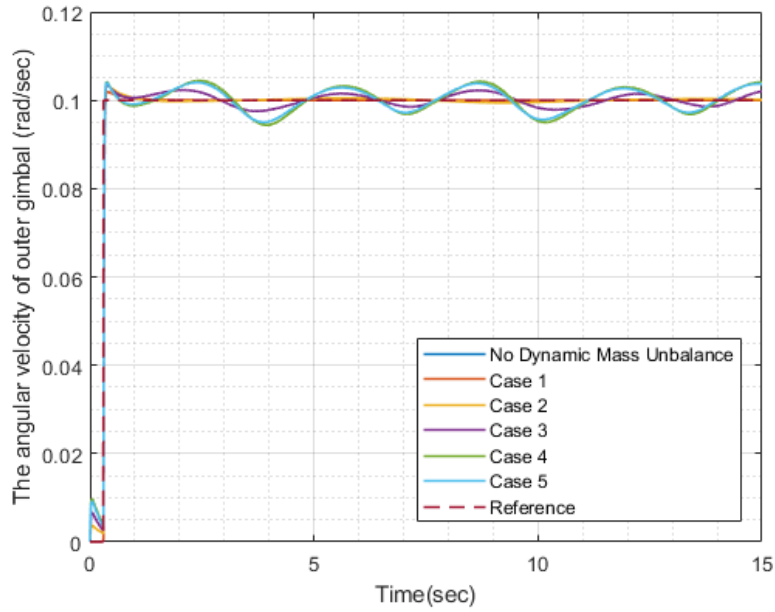


Figure 3.3: Results with test scenarios when $\omega_{oe_{ref}} = 0.1$ rad/sec

Here, in Figure 3.3, we can point out that as the angular velocity of the moving platform increases in Case 1 and Case 2, the overshoot, the settling time increases; however, the steady state error does not change. On the other hand, in Case 3, Case 4 and Case 5, the steady state is not reached any more, which means the system does not attain a stable operation since it oscillates.

ii. $\omega_{oe_{ref}} = 0.5$ rad/sec

In this section, $\omega_{oe_{ref}} = 0.5$ rad/sec (about 30 deg/sec) is selected as a higher velocity and the simulation results have been evaluated similarly. The result is presented in Figure 3.4.

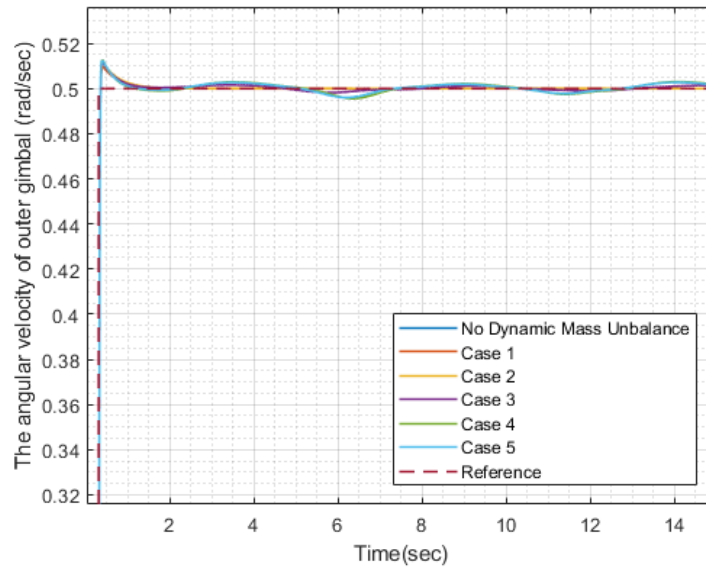


Figure 3.4: Results with test scenarios when $\omega_{o_{ref}} = 0.5$ rad/sec

Here, we can state that as the angular velocity of base frame increases, in Case 1 and Case 2, the overshoot, the settling time increase slightly and the steady state error does not vary. On the other hand, under the conditions in Case 3, Case 4 and Case 5, the system starts to oscillate again. However, the amplitude of the oscillations observed are less than the oscillations during the constant low velocity control, in Figure 3.3. The system response of no dynamic mass unbalance case and the Case 5 (the system experiences the highest disturbance due to dynamic mass unbalance) are compared in Figure 3.5.

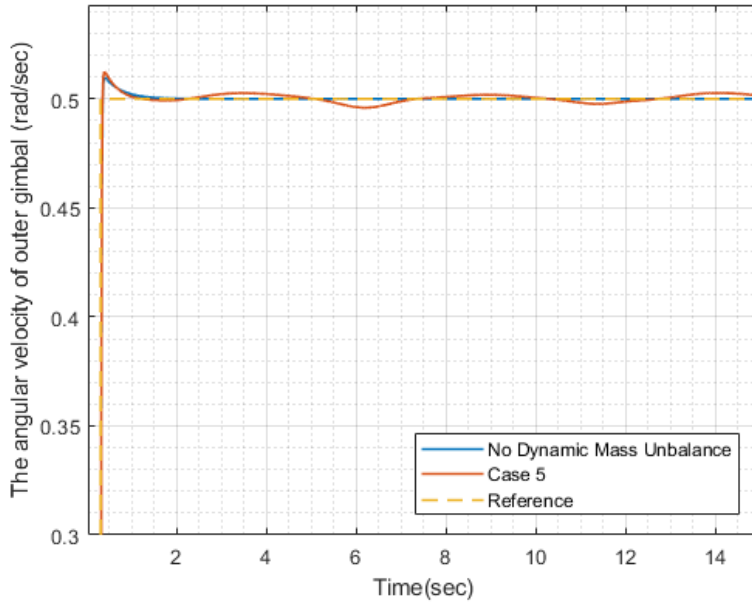


Figure 3.5: The comparison between no disturbance and Case 5 when $\omega_{oe_{ref}} = 0.5$ rad/sec

Figure 3.5 shows the system response becomes oscillating under dynamic mass unbalance more clearly when ω_{oe} is kept at 0.5 rad/sec. However, Figure 3.3 and Figure 3.4 point out that the oscillation occurs much more remarkably at low angular velocities of the moving platform.

3.2.3.c Simulation Results of the Inner Gimbal

Similarly, a PI controller has been implemented for constant angular velocity control of the inner gimbal. We may express the transfer function of it as:

$$G_{inner} = K_p + \frac{K_i}{s}$$

where $K_p = 10$ and $K_i = 30$. Therefore, the transfer function of the controller may be expressed in Equation 3.6 as:

$$G_{inner} = 10 + \frac{30}{s} \quad (3.6)$$

Throughout the simulation, the aim is to evaluate how dynamic mass unbalance resulting from different test scenarios listed in Table 3.1 influences the operation of the

constant velocity control, for which the simulation procedure conducted for the outer gimbal as well. Similarly, in Figure 3.6 , step response of the angular velocity of the inner gimbal is shown when there is no disturbance.

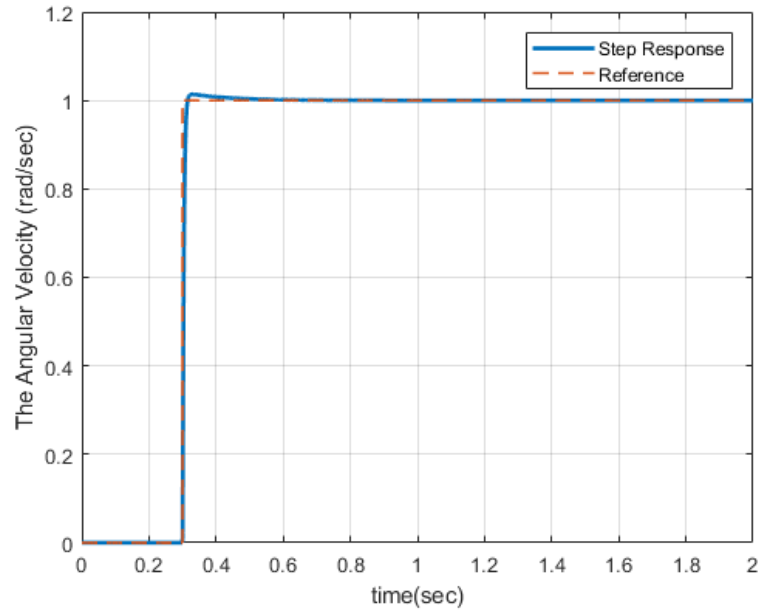


Figure 3.6: Step response of the elevation axis

To understand the effect of the dynamic mass unbalance on the inner gimbal, we have again carried out the simulation with the test conditions listed in Table 3.1. Also, all the cases have been tested with a low angular constant velocity and a higher one so that we can make a comparison between a slow constant velocity motion and relatively faster one. During the simulation, ω_{oe} is kept at 0.05 rad/sec.

i. $\omega_{ie_{ref}} = 0.1$ rad/sec

In this section, $\omega_{ie_{ref}} = 0.1$ rad/sec (about 6 deg/sec) is selected as a low velocity and the simulation has been done. The results are shown in Figure 3.7.

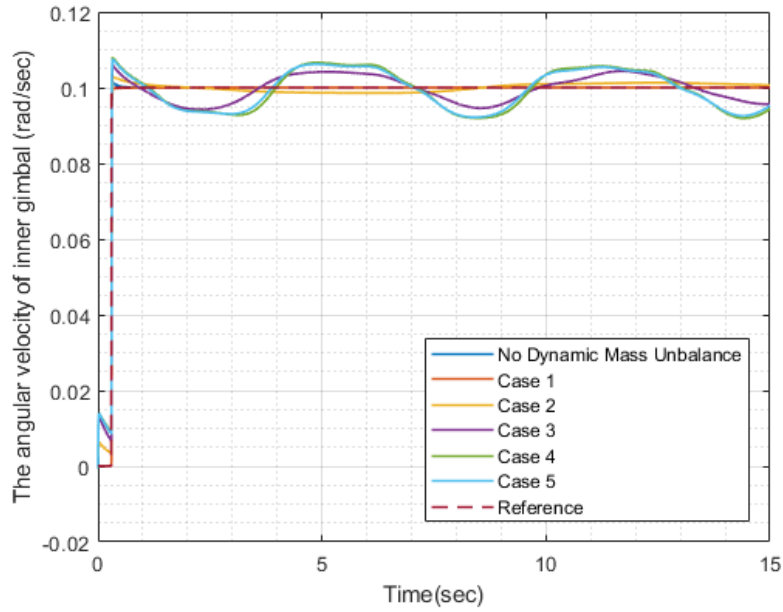


Figure 3.7: Results with test scenarios when $\omega_{ie_{ref}} = 0.1$ rad/sec

Consequently, it can be argued that the increasing angular velocity of the platform makes the system response unstable. In other words, the system undergoes the oscillations in Cases 3, 4 and 5 that disrupts the stable operation.

ii. $\omega_{ie_{ref}} = 0.5$ rad/sec

In this part, $\omega_{ie_{ref}} = 0.5$ rad/sec (about 30 deg/sec) is the higher velocity and the simulation results have been evaluated similarly, which are shown in Figure 3.8.

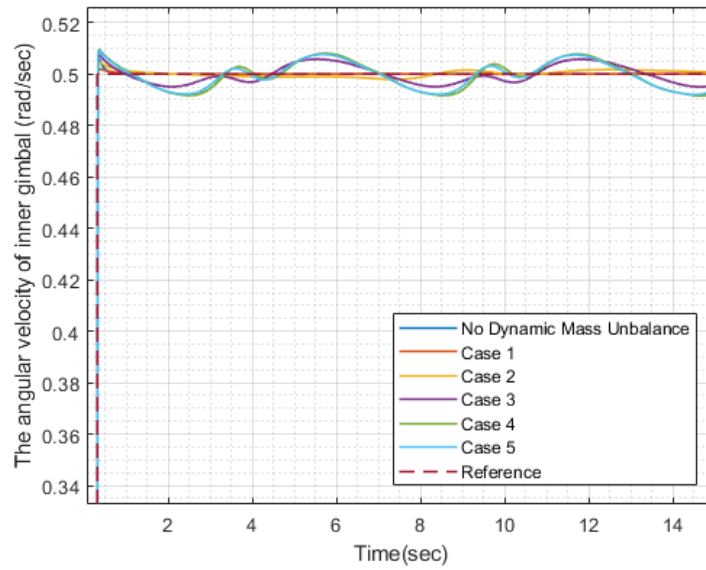


Figure 3.8: Results with test scenarios when $\omega_{ie_{ref}} = 0.5$ rad/sec

Here, again, we can state that disturbance due to the moving platform increases, the system response becomes oscillating. However, Figure 3.8 shows that the oscillations take place in a small range when ω_{ie} is kept at 0.5 rad/sec. Furthermore, Figure 3.7 and Figure 3.8 indicate that the amplitude of the oscillations are higher at low angular velocities.

3.2.3.d Evaluation of the Results

All in all, when the results of inner gimbal and outer gimbal are compared with each other, it can be concluded that the effect of the dynamic mass unbalance is a critical issue for the both of the gimbals. Even though it is more obvious at constant low velocity control, it is also clear that the dynamic mass unbalance degrades the system at higher constant velocities as well. This implies it should be taken into consideration when dynamic modelling performed.

3.3 Static Mass Unbalance

Static mass unbalance is a disturbance torque due to the offset between center of gravity of the gimbal and the pivot point [24]. The acceleration induced to the pivot point ends up with the disturbance if the rotational point and the center of mass do not coincide. Therefore, it becomes problematic for the stabilization loop of the body.

In the antenna platform, the center of the gravities of the gimbals are not located in pivot points. That is why they are expected to experience the disturbance due to the static mass unbalance.

3.3.1 Static Mass Unbalance of the Inner Gimbal

We have already obtained the dynamic equation of the inner gimbal in Equation 3.1 and expressed all applied torques on the body. Static mass unbalance is the term which includes mass of the gimbal, the offset position from the pivot point and gravitational acceleration. Consequently, static mass unbalance of the inner body can be stated as

$$T_{StaticMass_{inner}} = r_{oc_i} \times m_i g^i \quad (3.7)$$

where r_{oc_i} and g^i have been explained in Equation 2.40 previously. The disturbance torque induced on the elevation axis is the y component of the $T_{StaticMass_{inner}}$ which is represented as $T_{StaticMass_y}$

$$T_{StaticMass_y} = m_i (r_{oc_{iz}} g_x^i - g_z^i r_{oc_{ix}}) \quad (3.8)$$

3.3.2 Static Mass Unbalance of the Outer Gimbal

Similarly, the dynamic equation of the outer gimbal in Equation 3.3 has been worked on and we have expressed all the torques acting on the body. Again, static mass unbalance may be considered as the term which covers mass of the gimbal, the offset position from the pivot point and gravitational acceleration. Therefore, static mass unbalance of the inner body can be depicted as

$$T_{StaticMass_{outer}} = r_{oc_z} \times (m_o + m_i) g^o \quad (3.9)$$

where r_{oc_o} and g^o have been explained in Equation 2.52 previously. The disturbance torque induced on the azimuth axis is the z component of the $T_{StaticMass_{outer}}$ which is expressed as $T_{StaticMass_z}$

$$T_{StaticMass_z} = (m_o + m_i) (r_{oc_{oz}} g_x^o - g_z^o r_{oc_{ox}}) \quad (3.10)$$

3.3.3 Simulation Results

3.3.3.a Simulation Construction

To observe the effect of the static mass unbalance on the system, the path described in [24] is followed. For this purpose, we will work on the stabilization loops for the azimuth and the elevation axes that include PI controllers such that we can attain constant velocity control, which is the way we follow in the dynamic mass unbalance case.

Throughout the simulations, the angular velocities of each frame are attempted to be kept constant as this is the case in [19]. Similarly, the static mass unbalance for each gimbal figured out previously is implemented in MATLAB and Simulink environment with these stabilization loops, which is depicted in Figure 3.9.

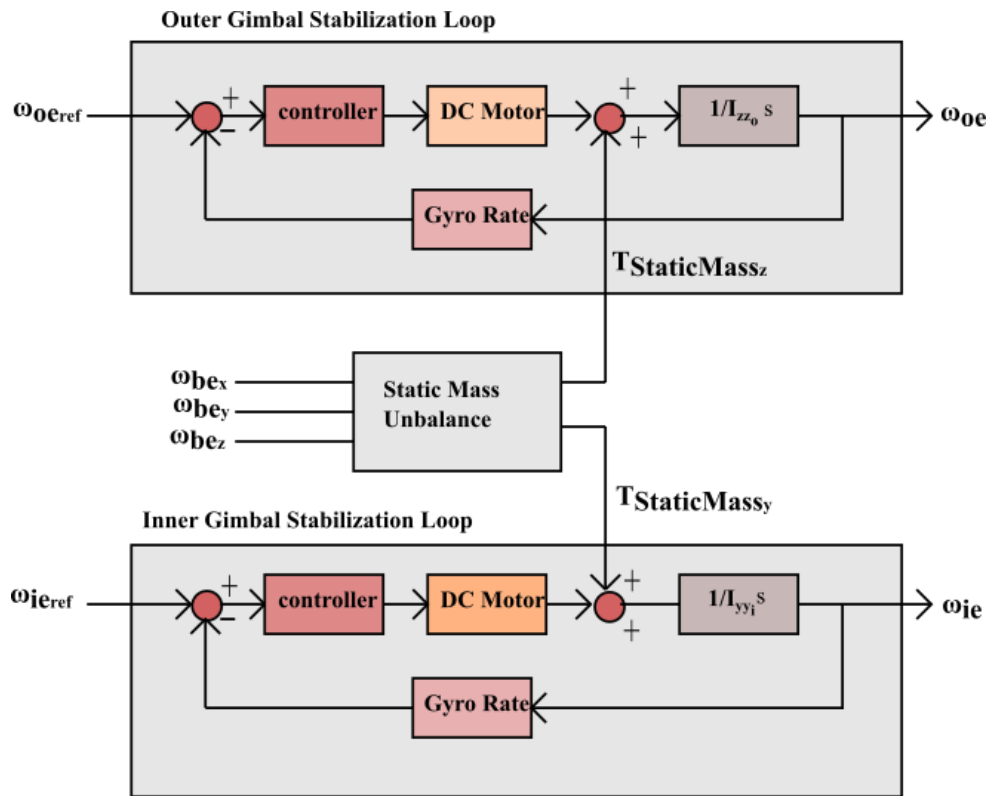


Figure 3.9: Stabilization loops for the outer and the inner gimbals

The simulations will be conducted with different cases in which the angular velocity of the platform will be adjusted to different values. Table 3.2 lists the test cases as follows:

Table 3.2: Different test cases with varying angular velocity of the platform

Case	The Angular Velocity of the Platform		
	ω_{be_x} (deg/s)	ω_{be_y} (deg/s)	ω_{be_z} (deg/s)
Case 1	0	0	0
Case 2	5	5	5
Case 3	10	10	10
Case 4	15	15	15

3.3.3.b Simulation Results of the Outer Gimbal

As explained in the previous section, a PI controller has been implemented for constant velocity control. The parameters of the PI controller have been taken the same as the values in Equation 3.5. Here we can state that the aim is to evaluate how static mass unbalance resulting from different test scenarios listed in Table 3.2 affects the operation of the constant velocity control of inner body.

i. $\omega_{oe_{ref}} = 0.1 \text{ rad/sec}$

We have already obtained the step response of the outer gimbal for $\omega_{oe_{ref}} = 0.1 \text{ rad/sec}$ in Figure 3.2. The system response experiencing static mass unbalance can be seen in Figure 3.10.

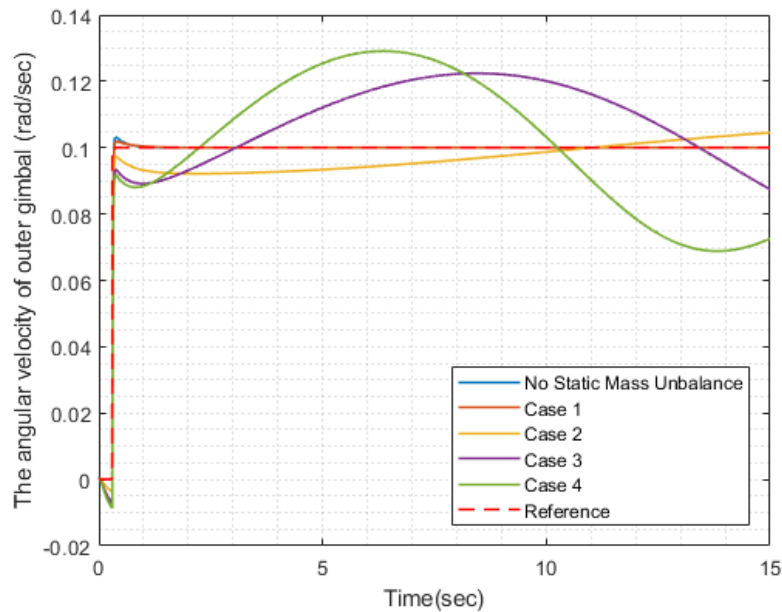


Figure 3.10: Results with test scenarios when $\omega_{oe_{ref}} = 0.1 \text{ rad/sec}$

In Figure 3.10, we may see that the static mass unbalance results in an oscillating system response even at low disturbance due to the moving platform. Increasing angular velocity of the platform results in higher magnitude and frequency oscillations. In fact, the gimbal can not be controlled at a constant velocity mostly.

ii. $\omega_{oe_{ref}} = 0.5 \text{ rad/sec}$

The results at a higher reference angular velocity of the outer gimbal is illustrated in Figure 3.11.

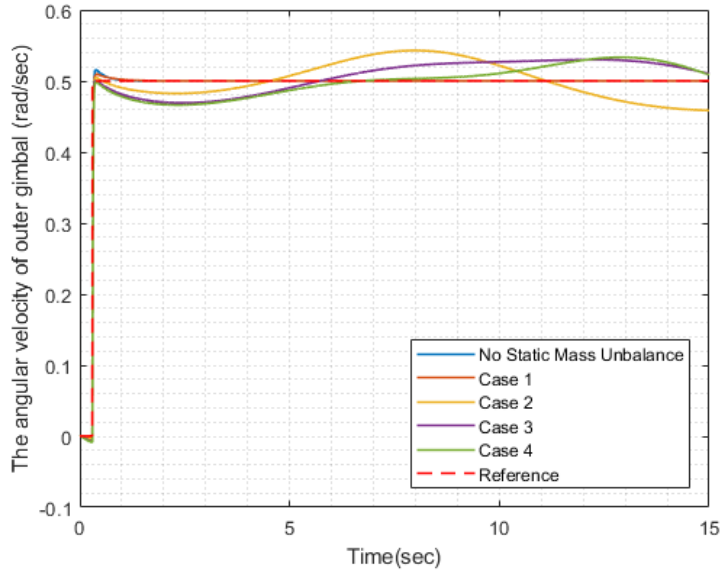


Figure 3.11: Results with test scenarios when $\omega_{oe_{ref}} = 0.5 \text{ rad/sec}$

The static mass unbalance still has a degrading effect on the stabilization at $\omega_{oe_{ref}} = 0.5 \text{ rad/sec}$ at which can be concluded from Figure 3.11. That means the system response still experiences high oscillations and there is no a steady state when the static mass unbalance is introduced to the stabilization loop.

3.3.3.c Simulation Results of the Inner Gimbal

Again, the parameters of the PI controller have been taken the same as the in Equation 3.6. Therefore, the purpose of the simulation is to observe how static mass unbalance resulting from different test scenarios listed in Table 3.2 affects the operation of the constant velocity control of the inner body.

i. $\omega_{ie_{ref}} = 0.1$ rad/sec

The system response of the inner gimbal at 0.1 rad/sec and experiencing static mass unbalance can be seen in Figure 3.12.

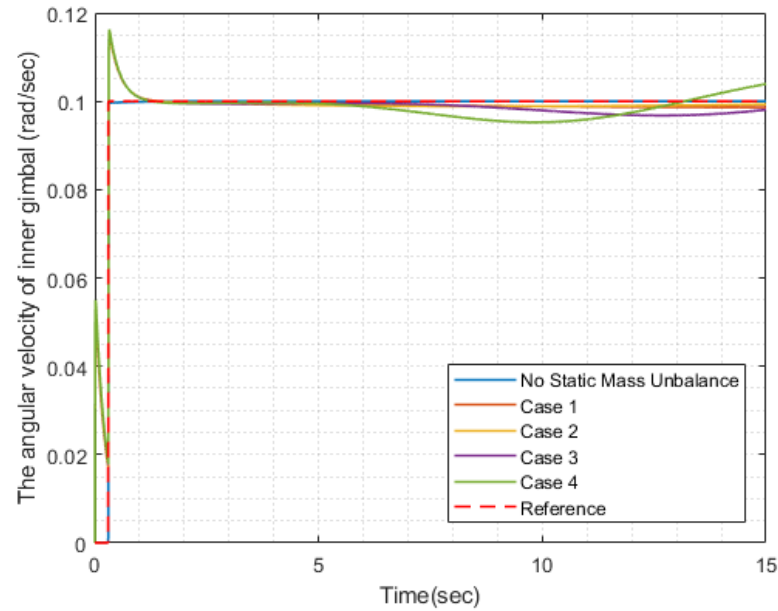


Figure 3.12: Results with test scenarios when $\omega_{ie_{ref}} = 0.1$ rad/sec

In Figure 3.12, we see that the system response has changed significantly when the disturbance due to static mass unbalance is involved in the stabilization loop. In other words, the response again starts to oscillate and the gimbal can not track the reference input precisely any more.

ii. $\omega_{ie_{ref}} = 0.5$ rad/sec

The results at a higher reference angular velocity is illustrated in Figure 3.13.

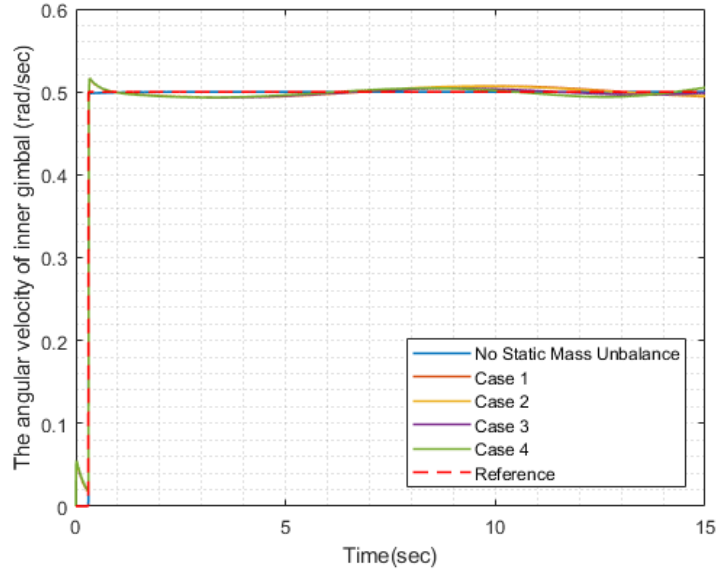


Figure 3.13: Results with test scenarios when $\omega_{i_{ref}} = 0.5$ rad/sec

As seen from Figure 3.13, at a high reference velocity, the response undergoes oscillations with lower amplitude than the case in which the angular velocity $\omega_{i_{ref}} = 0.1$ rad/sec even though the characteristics of the results seems very similar. In other words, the system has no steady state when the disturbance coming from the base movements increases which degrades the stable operation.

3.3.3.d Evaluation of the Results

Consequently, when the results of the inner and the outer gimbals are compared with each other, it can be argued that the effect of the static mass unbalance is a significant issue for both of the gimbals; especially for the outer gimbal. In other words, both of the gimbals have higher oscillations at constant low velocity control and even at higher constant velocities, the system can not achieve a stable operation as well. Therefore, the static mass unbalance concept must be included in the system model and it needs to be dealt with effectively.

3.4 Comparison of the Effects of Dynamic and Static Mass Unbalance

For the outer gimbal, the effect of the static mass unbalance is greater than the effect of the dynamic mass unbalance on the system response. That means that the disturbance due to static mass unbalance to the system becomes significantly dominant over the disturbance due to the dynamic mass unbalance. This result mainly relies on the inertia tensor of the outer gimbal and the offset position of the center of the outer mass. For this mechanical design, the position of the center of mass can be regarded as a more problematic disturbance source for the system response.

On the other hand, for the inner gimbal, the effect of the dynamic mass unbalance is more dominant over the disturbance due to the static mass unbalance. In other words, the effect of the nondiagonal inertia tensor of the inner gimbal becomes more degrading on the system response. Since the position vector of the center of the inner mass from the pivot point takes a very small value around zero, the static mass unbalance becomes a less critical disturbance source for the inner gimbal when it is compared with the effect of the inertia on the system performance.

CHAPTER 4

FRICITION IDENTIFICATION

4.1 Introduction

Friction can be defined as the force resisting to the motion as two mechanical bodies slide against each other and it exists in every mechanical system [25]. It may be represented with the static friction model that reflects the mapping between the relative speed of sliding surfaces and the friction torque is described as Coulomb torque, viscous friction, Stribeck effect. However, the static model can not explain the friction phenomena when the relative velocity of sliding surfaces is zero [26].

For a better understanding of the friction phenomena, it is necessary to describe the behaviour of the friction torque at very low velocities around zero where it may exhibit complicated dynamics [27], [28]. In fact, those dynamics may become dominant over the other system dynamics. In such systems, the static models based on the velocity-friction force mapping may not be sufficient for a high precision positioning and tracking [28], [29]. Furthermore, the dynamics of friction may bring about many other control problems such as large steady state errors and oscillations especially at low velocities. Consequently, it is necessary to come up with a good friction model with well-estimated dynamic parameters so that an accurate control of the system can be achieved [30], [31].

The dynamic friction models take place instead of static models to address the internal dynamics of the friction and to attain a better friction compensation. The Dahl model, the LuGre model can be regarded as the well-known dynamic models to describe the friction concept [26]. Dahl formed a dynamic friction model originated from

Coulomb friction model that includes a hysteresis characteristic around zero velocity [32]. Canudas de Wit et al. worked on the Dahl model by adding bristle concept to it, which has been figured out as Luge model [30], [33]. Luge model aims to describe the friction including static and dynamic properties in sliding and presliding regimes. Dynamic parameters of Luge model are attributed with the deflection of the asperities between mechanical surfaces and this concept results in a hysteresis behavior in presliding regime [34]. It also concentrates on the Stribeck effect that is not stated in the Dahl model, which is one of the reasons why Luge model may achieve more accurate modelling [35], [36].

All in all, Luge friction model, the more advanced dynamic model, will be considered in the friction identification part, which estimates the friction torques expressed in the dynamic equations of the inner and the outer gimbals in Chapter 2 and 3.

4.2 Luge Friction Model

Luge model is a dynamic friction phenomena based on Dahl model and worked up at the universities of Lund and Grenoble. It involves all the properties of Dahl model. Additionally, it also captures Stribeck effect; therefore, it can predict stick-slip motion [35]. In Luge model, friction is regarded as the force due to bending bristles or asperities between two surfaces which behave like springs shown in Figure 4.1.

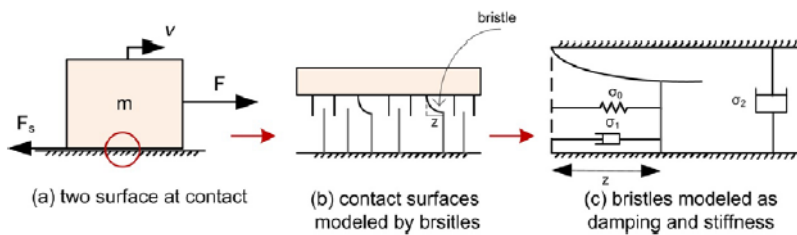


Figure 4.1: The bristles in Luge friction model [37]

The equations describing the model can be written as

$$\begin{aligned} T_{fr} &= \sigma_0 z + \sigma_1 \frac{dz}{dt} + \sigma_2 v \\ \frac{dz}{dt} &= v - \sigma_0 \frac{|v|}{s(v)} z \end{aligned} \quad (4.1)$$

where

T_{fr} : the predicted friction torque,

v : the velocity between two surfaces in contact,

z : the inertial friction state,

σ_0 : stiffness coefficient,

σ_1 : damping coefficient,

σ_2 : viscous damping coefficient,

$s(v)$: Stribeck effect.

The inertial state z represents the average deflection of the bristles. σ_0 and σ_1 are defined for small displacements; that means the spring behaviour of the bristles are modelled at very low velocities. The function $s(v)$ is capturing Stribeck effect and Coulomb torque in equation 4.2.

$$s(v) = T_c + (T_s - T_c) e^{\frac{|v|}{v_s} \delta} \quad (4.2)$$

where

T_s : The stiction torque,

T_c : The Coulomb torque,

v_s : Stribeck velocity,

δ : Stribeck shape factor.

Therefore, LuGre friction model is the combination of nonlinear functions consisting of seven parameters; five static parameters and two dynamic parameters [26]. Next, the experiments conducted to identify the parameters will be worked on.

4.3 The Identification of Friction Model with the Physical System

Lugre Friction Model is considered as the combination of two different friction regimes; presliding and the sliding regime. The sliding regime describes the friction as the force between the two mechanical components resulting from the relative velocity. Therefore, the sliding region points out a static mapping between the velocity of the sliding mechanical body and the friction torque it experiences. This region identifies the static parameters of the friction model.

However, the friction has internal dynamics such as stick-slip, frictional hysteresis that can be described in the presliding regime [38], [39]. It is assumed that there exist asperity junctions between the surfaces. These junctions deform elastically and plastically when the tangential load is applied in which friction torque depends on the displacements of these junctions. Therefore, the identification of the friction model is based on the experiments conducted in two phases; sliding phase experiments and presliding phase experiments. The former one can be attributed to static parameters (steady state characteristics) of the friction whereas the latter identifies the dynamic parameters of Lugre Model.

4.3.1 Sliding Phase Experiments

This section is based on the constant velocity experiments [40], [26], [37]. When inner or outer body is controlled at a constant velocity, the torque applied on the body equals to the friction torque since the system is balanced. To get the set of measurements, the velocity of the inner or outer body has to be kept constant for a while which means that the experiments should be conducted via a closed PI controller to attain a steady state velocity.

The experiments for the inner gimbal and the outer gimbal have been done separately. The sliding phase experiments of the inner gimbal describes the static parameters of the friction between the inner gimbal and its pivot point while the inner body rotates around it. On the other hand, the sliding phase experiments of the outer gimbal identifies the steady state characteristics of the friction between the outer body and the platform.

4.3.1.a Experimental Setup

For outer and inner gimbals, the experiments have been worked on 45 different constant velocities ranging from 0.001 rad/sec to 0.1 rad/sec. At each different velocity, the outer and inner gimbal attain a rotational motion around its axis from 0 degree (initial position) to 75 degrees (final position). In order to concentrate on the Stribeck effect, the number of the measurements at low velocities is greater throughout the experiments. At each velocity, the average torque applied to the gimbal is recorded and all the data is combined such that we can form a mapping between the velocity of the gimbal and the corresponding torque measured, the friction torque. In Figure 4.2 and Figure 4.3, the experiment dataset for both inner and outer gimbals respectively can be seen.

According to the friction-velocity mapping obtained from the experiments, it may be concluded that the curves of the friction torque for inner and outer gimbals have the same characteristics. The friction torque decreases when the angular velocity of the gimbals increases up to a certain value, which can be defined as the Stribeck effect and it starts to rise from that point with a specific slope, that is the viscous effect.

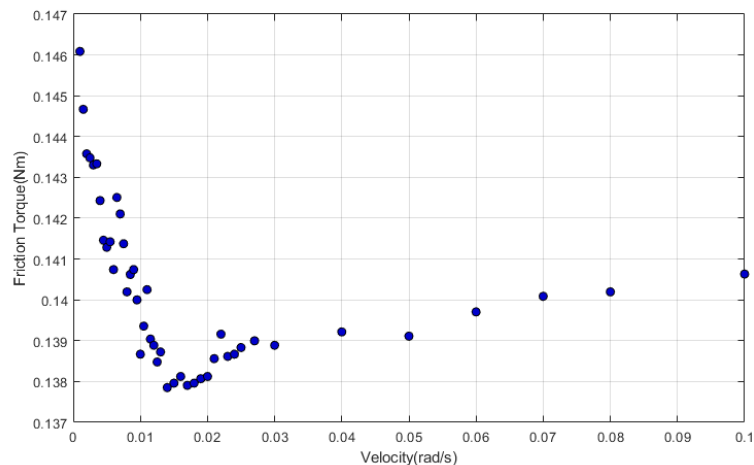


Figure 4.2: The friction-velocity graph of the inner gimbal from the experimental data

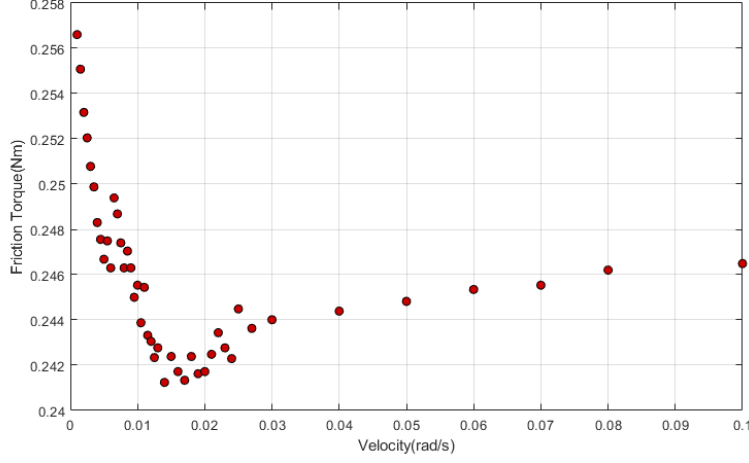


Figure 4.3: The friction-velocity graph of the outer gimbal from the experimental data

4.3.1.b Identification of Static Parameters

The Lugre model for one-axis rotational motion can be written as

$$T_{fr} = \sigma_0 z + \sigma_1 \frac{dz}{dt} + \sigma_2 v$$

$$\frac{dz}{dt} = v - \sigma_0 \frac{|v|}{s(v)} z$$

$$s(v) = T_c + (T_s - T_c) e^{\frac{|v|}{v_s} \delta}$$

In sliding phase experiments, the inner and outer gimbals are assumed to be balanced when they are controlled such that they achieve a constant velocity angular motion. Therefore, we can regard each constant velocity in the experiment set as a steady state velocity for the gimbals. Under steady state velocity, the bristle deflection is constant; therefore, $\frac{dz}{dt}$ equals to zero. By using Equation 4.1, the following can be written:

$$z_{ss} = \frac{s(v)}{\sigma_0} \text{sgn}(v) \tag{4.3}$$

$$T_{ss} = (T_c + (T_s - T_c) e^{\frac{|v|}{v_s} \delta}) \text{sgn}(v) + \sigma_2 v$$

Therefore, T_c , T_s , σ_2 , v_s and δ parameters can be obtained from the friction-velocity map. To identify these static parameters of Lugre model, a curve fitting technique based on nonlinear optimization, is implemented. The cost function of the optimiza-

tion is stated in Equation 4.4.

$$C(T_c, T_s, \sigma_2, v_s, \delta) = \min \sum_{i=1}^n (\hat{T}_{ss_i} - T_{ss_i})^2 \quad (4.4)$$

where \hat{T}_{ss_i} is the experimental torque data obtained during constant velocity v_i whereas T_{ss_i} represents the output of LuGre friction model expressed in Equation 4.3.

i. Static Parameters of the Inner Gimbal

The estimated steady state output of LuGre friction model and the data points obtained from the experiments are depicted in Figure 4.4.

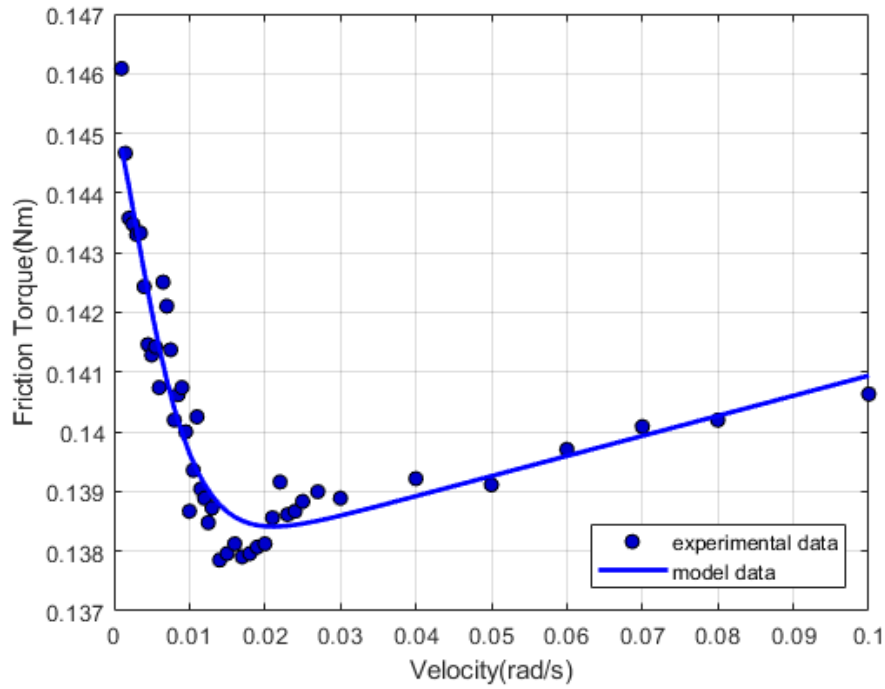


Figure 4.4: The estimated friction-velocity graph of the inner gimbal and experimental data

Therefore, the identified values of the parameters resulting from curve fitting are listed in Table 4.1.

Table 4.1: The static parameters of LuGre friction model for the inner gimbal

Lugre Model Parameter	Unit of the Parameter	Optimized Value
T_s	Nm	0.1451
T_c	Nm	0.1376
v_s	rad/s	0.0075
σ_2	Nm.s/rad	0.0336
δ	-	1.4628

ii. Static Parameters of the Outer Gimbal

Similarly, for the outer gimbal, the estimated steady state output of LuGre friction model and the data points obtained from the experiments are shown in Figure 4.5.

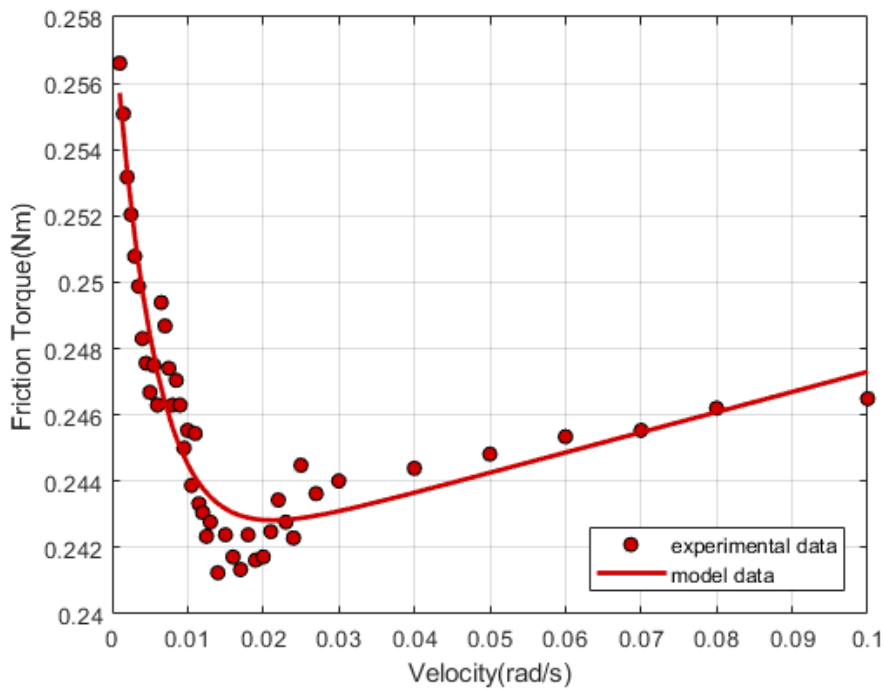


Figure 4.5: The estimated friction-velocity graph of the outer gimbal and experimental data

Consequently, the identified values of the parameters resulting from curve fitting are listed in Table 4.2.

Table 4.2: The static parameters of Lugre friction model for the outer gimbal

Lugre Model Parameter	Unit of the Parameter	Optimized Value
T_s	Nm	0.2585
T_c	Nm	0.2412
v_s	rad/s	0.0054
σ_2	Nm.s/rad	0.0609
δ	-	1.0459

4.3.2 Presliding Phase Experiments

Previously, it is argued that seven parameters describes Lugre friction model. Static parameters have been estimated with sliding phase experiments and there are two remaining in the equations, which are the dynamic parameters; σ_0 and σ_1 . These parameters can be attributed to the stiffness and the damping characteristics of the bristles in the model. Therefore, the identification of σ_0 and σ_1 will be achieved in the presliding phase.

Dynamic parameters are more difficult to be identified when it is compared with the static parameters since they are related to the internal dynamics of the gimbals and z , internal state of the friction model, which is not measurable. In this section, the time domain approach suggested by Hensen [37] will be implemented in order to identify these parameters.

For a rotating body, the following statement is valid:

$$T_{input} = I\dot{v} + T_{fr}$$

where T_{input} represents the input torque to the system, I is the inertia of the rotating body induced on the rotational axis, \dot{v} stands for the angular acceleration and T_{fr} is the friction torque which is the output data of Lugre friction model. In the presliding phase, small junction deformations occur and the condition $|z| \ll s(v)$ is valid, which leads to $\frac{dz}{dt} = v$ as suggested by Equation 4.1. Therefore, the following equation can

be written within small displacements in the presliding phase:

$$\begin{aligned} T_{fr} &= (\sigma_1 + \sigma_2)v + \sigma_0 z \\ T_{input} &= I\dot{v} + T_{fr} \\ T_{input} &= I\dot{v} + (\sigma_1 + \sigma_2)v + \sigma_0 z \end{aligned} \quad (4.5)$$

Since $\frac{dz}{dt} = v$, we can express Equation 4.5 as the following;

$$T_{input} = I\ddot{z} + (\sigma_1 + \sigma_2)\dot{z} + \sigma_0 z \quad (4.6)$$

In Laplace domain;

$$\frac{z(s)}{T_{input}(s)} = \frac{1}{Is^2 + (\sigma_1 + \sigma_2)s + \sigma_0} \quad (4.7)$$

This transfer function represents a second order LTI system around the equilibrium point within the small displacement. If Equation 4.7 is rewritten in the generalized form as follows:

$$\frac{z(s)}{T_{input}(s)} = \frac{K}{s^2 + 2\zeta\omega_n s + \omega_n^2} \quad (4.8)$$

where ζ is the damping ratio and ω_n is the natural frequency of the system. From Equations 4.8 and 4.7, the dynamic parameters of the LuGre friction model may be expressed as;

$$\sigma_0 = \omega_n^2 I \quad (4.9)$$

$$\sigma_1 = 2\zeta\omega_n I - \sigma_2 \quad (4.10)$$

4.3.2.a Experimental Setup

In this work, the input torque applied to the system is observed when the system is controlled at very low velocity around zero point, 0.001 rad/sec, the minimum velocity that can be driven by the system. It is observed that for a certain time, the rotational motion does not exist clearly even though the current of the motor increases. After a time interval, the angular displacement becomes observable and sliding of the body starts. That time interval is noted as the presliding time and the input torque on the interval is evaluated and checked whether it is smaller than the breakaway torque identified previously or not because we have to ensure that the magnitude of the input torque is less than breakaway torque such that the system attains presliding micro displacements. Hence, we guarantee that the system is in presliding phase in

which \dot{v} , v remain zero; therefore, \ddot{z} and \dot{z} equal to zero as well, that results in an approximation based on the Equation 4.5.

$$\Delta T_{input} = \sigma_0 \Delta z \quad (4.11)$$

Therefore, the estimation of σ_0 may be achieved by investigating the input torque within small displacements of the system. During the presliding phase experiments, a slowly varying torque input versus very small displacements the system experience has been assessed for the rotating bodies; inner and outer gimbals separately. Up until sliding phase, those small changes in the angular position can be read from the encoder. Throughout the experiments the positions of the inner and the outer gimbals, the input torque value as well just before the sliding phase starting are recorded with many trials for the consistency. Next, by using the equation 4.11, σ_0 is identified for both of the gimbals. After specifying σ_0 , ω_n can be calculated. Furthermore, the inertia of the inner and outer gimbals can be considered as I_{yy_i} and I_{zz_o} respectively. To identify σ_1 , the only remaining parameter is the damping ratio; ζ . As σ_1 is calculated for the inner and the outer gimbals, the damping ratio, ζ , is considered between 0.8 and 1.0 for a stable operation [37].

In Table 4.3, how long the presliding phase of the gimbals takes have been noted. Moreover, the change in angular position during their time intervals can be figured out as well.

Table 4.3: Presliding phase experimental data

	Presliding Time (second)	$\Delta Angular Position$ (degree)
Inner Gimbal	9.85	0.34
Outer Gimbal	10.3	0.63

In Table 4.4, the identified dynamic parameters of LuGre friction model are depicted for the inner and the outer gimbals.

Table 4.4: Dynamic parameters of LuGre friction model

	ΔT_{input} (Nm)	Δz (rad/s)	σ_0	σ_1
Inner Gimbal	0.144	0.00060	271.68	6.97
Outer Gimbal	0.254	0.00106	238.88	16.02

4.3.3 The Identified Friction Models

4.3.3.a LuGre Friction Model of the Inner Gimbal

All the parameters identified for the inner gimbal are listed in Table 4.5.

Table 4.5: The parameters of LuGre friction model for the inner gimbal

LuGre Model Parameter	Unit of the Parameter	Optimized Value
T_s	Nm	0.1451
T_c	Nm	0.1376
v_s	rad/s	0.0075
σ_0	Nm.s/rad	271.68
σ_1	Nm.s/rad	6.97
σ_2	Nm.s/rad	0.0336
δ	-	1.4628

To evaluate the characteristics of LuGre friction model around zero velocity, a one-period sine wave is input to the system representing the angular velocity of the inner gimbal. The resultant friction- velocity map of the inner gimbal is shown in Figure 4.6.

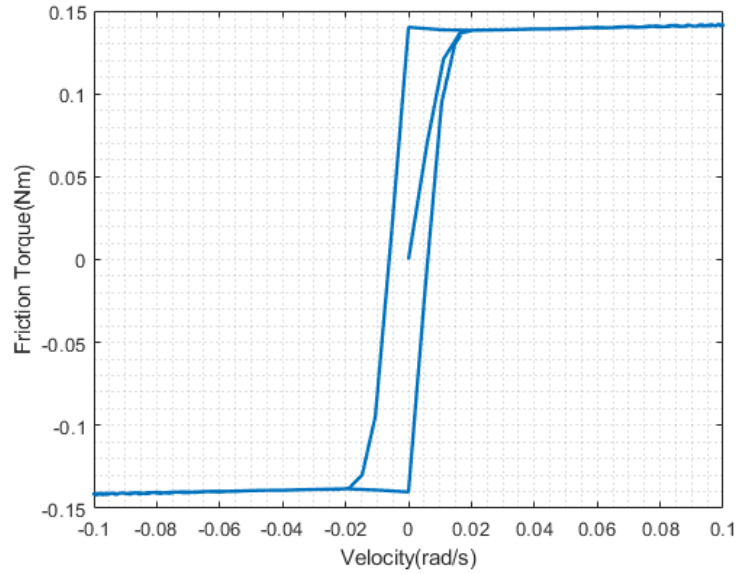


Figure 4.6: The friction-velocity graph of the inner gimbal with identified parameters

In Figure 4.6, the hysteresis behaviour of LuGre friction around zero velocity and also the other characteristics attributed to the model can be seen clearly.

4.3.3.b LuGre Friction Model of the Outer Gimbal

All the parameters identified for the inner gimbal are listed in Table 4.6.

Table 4.6: The parameters of LuGre friction model for the outer gimbal

LuGre Model Parameter	Unit of the Parameter	Optimized Value
T_s	Nm	0.2585
T_c	Nm	0.2412
v_s	rad/s	0.0054
σ_0	Nm.s/rad	238.88
σ_1	Nm.s/rad	16.02
σ_2	Nm.s/rad	0.0609
δ	-	1.0459

Similarly, to observe the characteristics of LuGre friction model around zero velocity, a one-period sine wave is input to the system representing the angular velocity of the

outer gimbal. The resultant friction- velocity map of the outer gimbal is shown in Figure 4.7.

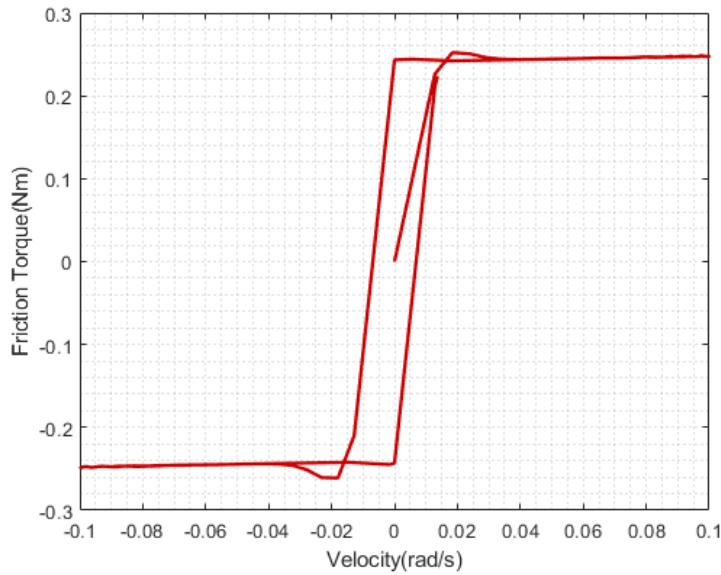


Figure 4.7: The friction-velocity graph of the outer gimbal with identified parameters

Similarly, we can see the hysteresis behaviour of LuGre friction around zero velocity and also the other characteristics attributed the LuGre friction model in Figure 4.7.

4.4 The Identification of Friction Model in Simulation Environment

4.4.1 Simulation Construction

In this section, the friction identification has been worked with the system model in Simulink as a second approach. The output data of the physical system is implemented in Simulink with the identified parameters of LuGre model in the previous section, which are the exact parameters of the friction model. By adding band-limited Gaussian white noise to the output data of the model in Simulink corresponding to a reference input, we simulate the measured data of the physical body. Next, a new parameter matrix identifying the friction torque is found using the simulated data.

As seen from Figure 4.8, a step input is given to the Simulink block that imitates the actual behaviour of the physical system with actual parameters and to Simulink model

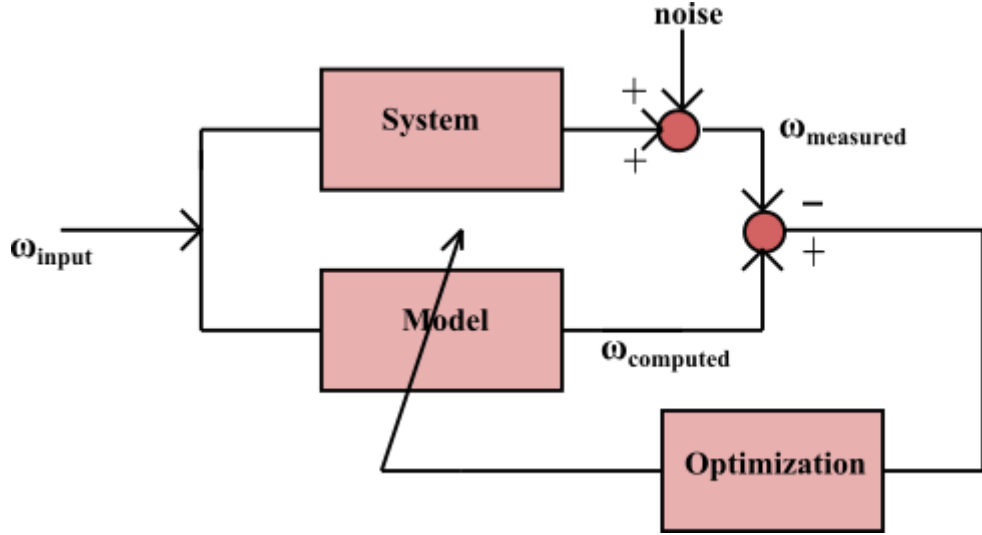


Figure 4.8: The friction-velocity graph of the inner gimbal with identified parameters

based on the dynamical equations of the gimbals. The measurement noise, a band-limited white noise, is added to the system response, which represents the measured data whereas the output of the Simulink model is denoted as computed output data. The difference between the system output and the model output is processed as the error function which will be tried to be minimized via an optimization method. At the end of each iteration, the parameter matrix of the friction model will be updated so that the output of the model can approach to the measured output ultimately.

4.4.2 The Optimization Method

For the procedure, a gradient-based optimization is implemented. The error function can be written as:

$$J(p_k) = \frac{1}{2} \sum_{i=1}^n \|\omega_{computed}^i - \omega_{measured}^i\|^2 \quad (4.12)$$

where n represents the number of sampling at each iteration whereas p_k denotes the parameter matrix of Lugre friction model at k^{th} iteration represented as

$$p_k = [T_s \quad T_c \quad v_s \quad \sigma_0 \quad \sigma_1 \quad \sigma_2 \quad \delta]^T \quad (4.13)$$

The optimization problem can be described as

$$\min_{p_k} J(p_k) = \min_{p_k} \frac{1}{2} \sum_{i=1}^n \|\omega_{computed}^i - \omega_{measured}^i\|^2$$

subject to

the dynamic equations of the gimbals,

$$T_c \leq s(v) \leq T_s$$

At the end of k^{th} iteration, the parameter matrix is updated with the following rule;

$$p_{k+1} = p_k - \alpha_k \nabla J(p_k)$$

where $\alpha_k > 0$ is the step size of the operation and $\nabla J(p_k)$ is the gradient vector.

$$\nabla J(p_k) = \left[\frac{\partial J}{\partial p_1} \quad \frac{\partial J}{\partial p_2} \quad \frac{\partial J}{\partial p_3} \quad \frac{\partial J}{\partial p_4} \quad \frac{\partial J}{\partial p_5} \quad \frac{\partial J}{\partial p_6} \quad \frac{\partial J}{\partial p_7} \right]^T$$

The partial derivatives in the gradient vector is calculated approximately as:

$$\frac{\partial J}{\partial p_j} \simeq \frac{J(p_k + \epsilon e_j) - J(p_k)}{\epsilon} \quad (4.14)$$

where $j = 1, 2, 3, \dots, 7$ represents the j^{th} parameter of Lugre friction parameter matrix while ϵ indicates a very small derivation step. Additionally, e_j is a 7x1 matrix whose j^{th} element is 1. By proceeding the explained operation, the parameters of Lugre model for two gimbals are identified and compared with the exact parameters coming from the measurement with the physical system.

4.4.2.a The Friction Parameters of the Outer Gimbal

The identified parameters resulting from optimization are depicted in Table 4.7.

Table 4.7: The parameters of LuGre friction model for the outer gimbal

Lugre Model Parameter	Unit of the Parameter	Identified Value
T_s	Nm	0.2555
T_c	Nm	0.2455
v_s	rad/s	0.0055
σ_0	Nm.s/rad	230.99
σ_1	Nm.s/rad	14.99
σ_2	Nm.s/rad	0.0655
δ	-	1.05

Furthermore, in Figure 4.9 , the measured output of the system and the computed output of the model are shown as well. It implies that the parameter matrix defined via the optimization session minimizes the error function significantly.

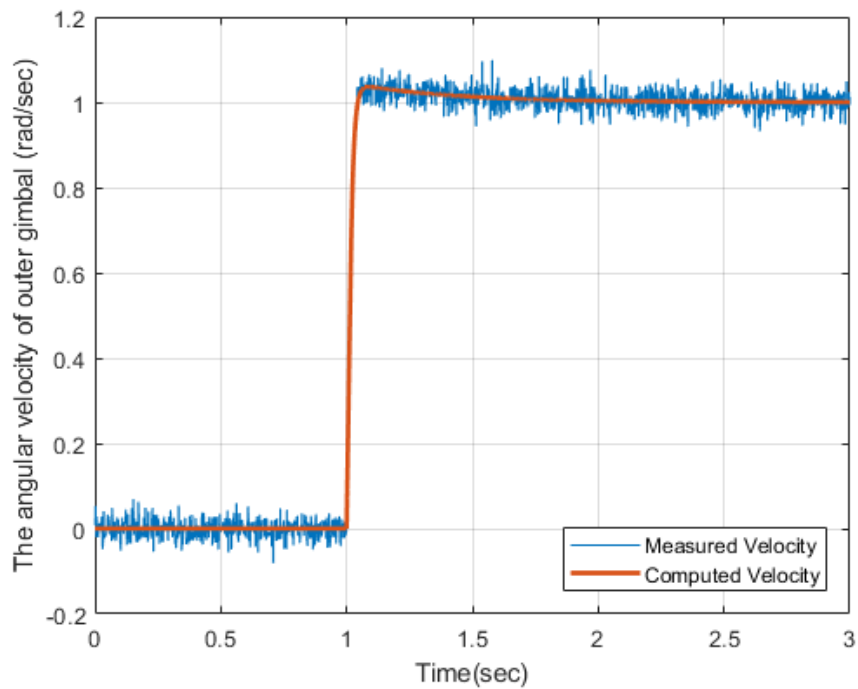


Figure 4.9: The friction-velocity graph of the outer gimbal with identified parameters

In Table 4.8, the exact parameters and the identified parameters in this section is com-

pared.

Table 4.8: Comparison of the parameters

	T_s	T_c	v_s	σ_0	σ_1	σ_2	δ
Exact Parameters	0.2585	0.2412	0.0054	238.88	16.02	0.0609	1.049
Identified Parameters	0.2555	0.2455	0.0055	230.99	14.99	0.0655	1.05

Table 4.8 points out that the identified parameters with the simulated model are close enough to the ones obtained from the measurements.

4.4.2.b The Friction Parameters of the Inner Gimbal

The identified parameters of the inner gimbal via the optimization method are listed in Table 4.9.

Table 4.9: The parameters of Lugre friction model for the inner gimbal

Lugre Model Parameter	Unit of the Parameter	Identified Value
T_s	Nm	0.1455
T_c	Nm	0.1350
v_s	rad/s	0.0071
σ_0	Nm.s/rad	270.01
σ_1	Nm.s/rad	5.99
σ_2	Nm.s/rad	0.0310
δ	-	1.4510

Moreover, in Figure 4.10, the measured output of the system and the computed output of the model are depicted as well. Similarly, it brings about that the parameter matrix defined via the optimization session minimizes the error function crucially.

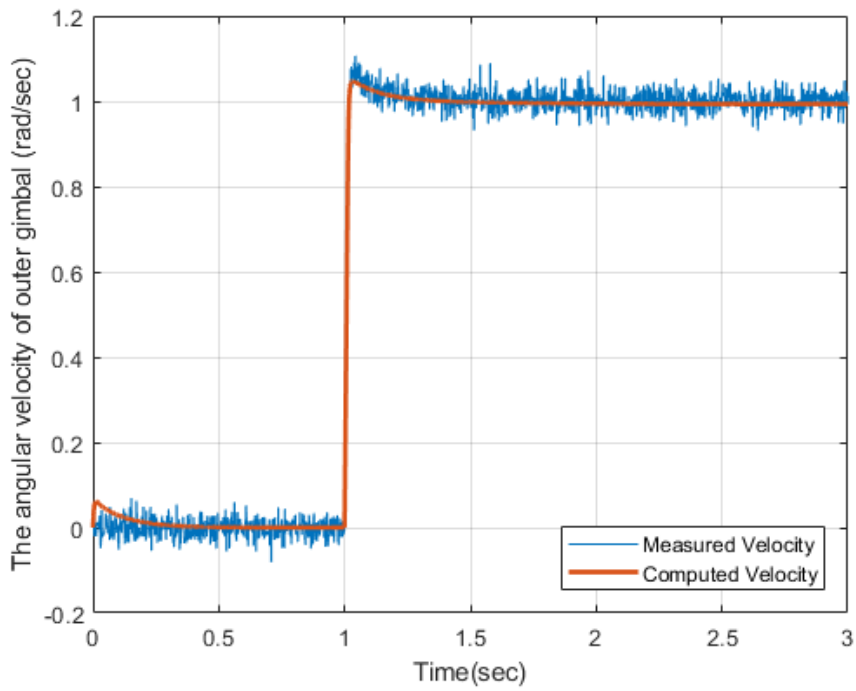


Figure 4.10: The friction-velocity graph of the outer gimbal with identified parameters

In Table 4.10, the exact parameters and the identified parameters in this section is compared.

Table 4.10: Comparison of the parameters

	T_s	T_c	v_s	σ_0	σ_1	σ_2	δ
Exact Parameters	0.1451	0.1376	0.0075	271.68	6.97	0.0336	1.4628
Identified Parameters	0.1455	0.1350	0.0071	270.01	5.99	0.0310	1.4510

Table 4.10 table concludes that the identified parameters with the simulated model are coinciding with the ones obtained from the measurements.

CHAPTER 5

MATHEMATICAL MODEL AND THE CONTROLLER

5.1 Introduction

The dynamic modelling of the inertially stabilized systems has a great importance for a stable operation; however, not only the dynamic modelling but also the controller design should be taken seriously such that the system can attain the required positioning because the nonlinear terms involved in the dynamic equations make the implementation of the controller harder for moving gimballed systems [41], [42].

For such systems, a great number of control methods have been proposed such as sliding mode control, proxy-based sliding control, linear quadratic regulators, linear quadratic Gaussian algorithm. In addition to these approaches, more advanced techniques, such as robust control, variable structure control, fuzzy logical control have also been performed in the stabilization problems [24].

However, in spite of the modern techniques listed above, commercial systems still compromise on the cascade control systems based on PID control [43]. In other words, the conventional PID method and the combination of two or more PID controllers are still most widely-applied controllers since the modern approaches are complicated and hard to implement in real world. Furthermore, the fact that the design of PID controllers is cost-effective and simple with satisfactory high performance makes them the most attractive and the most used method in the industry [24].

Thus, cascade control systems, superior to the conventional PID in terms of positioning and tracking [44] are applied in this thesis work in order to obtain a high

performance. Since derivative computations result in noise easily in industrial applications [45], the derivative gain is not included in the resultant controller. Hence, cascade PI control method is proposed due to the advantages pointed out previously.

5.2 Dynamic Models

5.2.1 Dynamic Model Representation of the Outer Gimbal

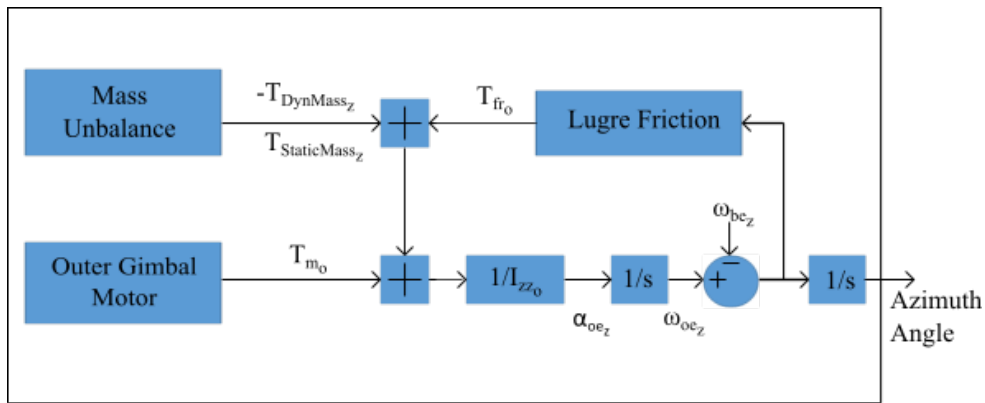


Figure 5.1: The block diagram of the outer gimbal

In Figure 5.1, the block diagram representing the dynamic model of the outer gimbal is indicated. It consists of mainly three sub-blocks; the stabilization loop implementing the kinematic equations without any controller, mass unbalance block investigated in Chapter 3 in a detailed way and Lugre Friction block worked in Chapter 4. It basically integrates all the elements of the dynamic equations into the model which handles torques induced on the azimuth axis. Therefore, the dynamic model of the outer gimbal shown in Figure 5.1 is implemented in Simulink/MATLAB. Next, the controller will be added to the outer body dynamics to achieve a stable control on the azimuth axis.

5.2.2 Dynamic Model Representation of the Inner Gimbal

Similarly, in Figure 5.2, the block diagram of the inner gimbal expressing the dynamic model is presented. Again, we may see three sub-blocks; the stabilization loop

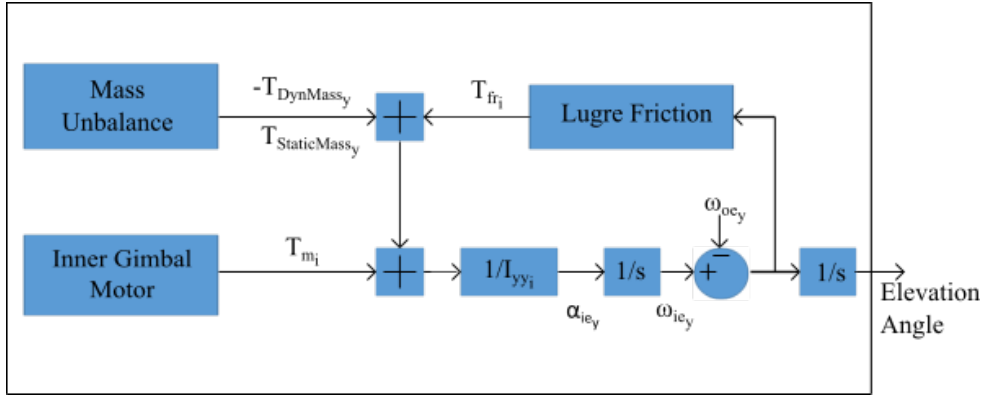


Figure 5.2: The block diagram of the inner gimbal

implementing the kinematic equations, mass unbalance block summarizing dynamic mass unbalance and the static mass unbalance and Lugre Friction block identifying the friction force of the elevation axis. In other words, the block diagram includes all the elements of the dynamic equations in which torques induced on the elevation axis is simulated. Consequently, the dynamic model of the inner gimbal shown in Figure 5.2 is implemented in Simulink/MATLAB and it will be controlled to provide a proper positioning.

5.3 Cascade PI Controller

In this thesis work, cascade PI controller is implemented in both azimuth and elevation axes. In a cascade control system; there are two control loops; primary loop or the outer loop and secondary loop or the inner loop. The controller in the secondary loop is called as the secondary controller or slave controller while the controller in the primary loop is defined as the primary controller or the master controller. The control signal of the primary controller is the input of the secondary controller or the set point of it [46].

The cascade control systems studied in this thesis have also the primary and secondary control loops; therefore, they include the primary controller and the secondary controller. The former takes the feedback from the position of the gimbals whereas the feedback of the latter comes from gyroscope of the related axis. The cascade system

for inner and outer gimbals are indicated in Figure 5.3 and Figure 5.4.

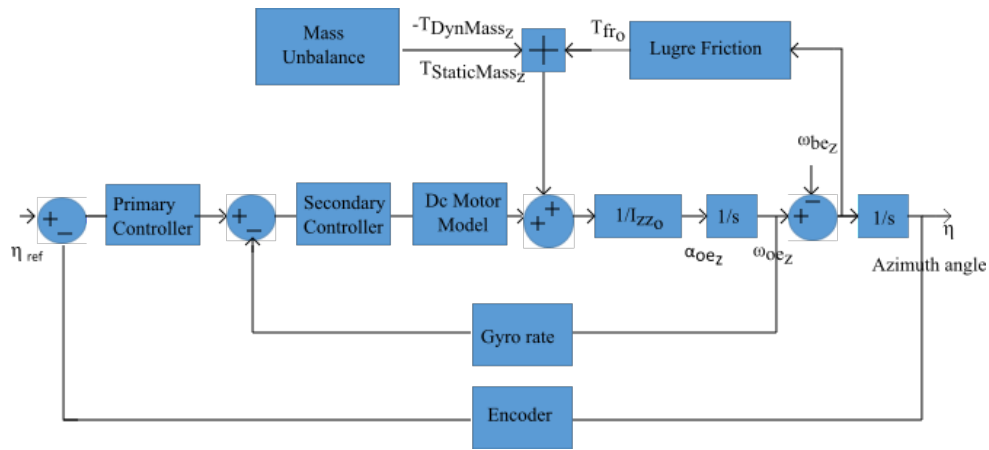


Figure 5.3: The cascade control system for the outer gimbal

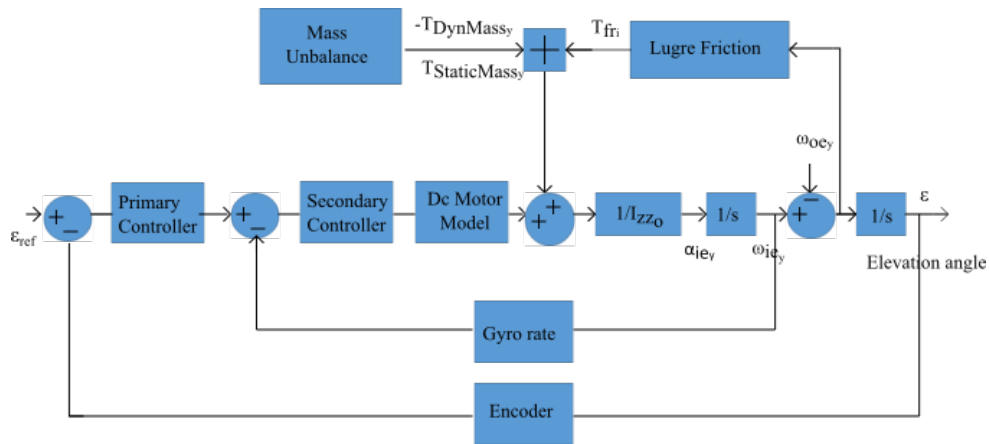


Figure 5.4: The cascade control system for the inner gimbal

Here, the aim of the secondary controller is to compensate the disturbance torque quickly so that the effect of the disturbance on the primary loop output is small which brings about more effective primary control. Furthermore, cascade controller may end up with a more linear relation between the input of the secondary controller and the angular velocities of the gimbals. In the secondary control loop, DC motor is regarded as the actuator. When cascade control is implemented, secondary control loop may be attributed with the new actuator having better linearity or proportionality and the better linearity results in an easier tuning process of the primary controller [46].

All in all, when the advantages of the cascade control systems listed above and the effective and easy-implemented control provided from PID controller are taken into

consideration, PI controllers are chosen as the primary and the secondary controllers whose transfer functions may be expressed as:

$$G(s) = K_p + \frac{K_i}{s}$$

where K_p is the proportional gain while K_i represents the integral gain of the controllers.

5.3.1 Tuning of the Controller Parameters

The tuning of these parameters is carried out to attain specific settling time, overshoot and steady state error of the step response of the systems when the system is induced to a high mass unbalance disturbance due to the moving platform and the friction torque (The angular velocity of the moving base is adjusted to different values based on the test cases in Table 3.1 and Table 3.2 when tuning is performed). The tuning of the parameters is performed step by step; first, the parameters of the secondary controller are tuned and then the primary controller parameters are dealt with.

For each controller, K_p and K_i parameters are set to the initial values manually (while one of them is fixed, the other one takes different values so as to maximize the performance). When the parameters are adjusted to their initial values, the statements in Table 5.1 guides the tuning [47].

Table 5.1: The effect of increasing PI parameters on the dynamic characteristics

Parameter	Overshoot	Settling Time	Steady State Error
K_p	Decrease	Increase	Decrease
K_i	Decrease	Increase	Decrease Significantly

Therefore, by comparing the system response in terms of steady state error, the overshoot and the settling time, the parameters are chosen for the secondary controller and the primary controller, respectively.

5.3.2 The Secondary Controller Design

i. The Secondary Controller of the Outer Gimbal

In Figure 5.5, the secondary loop of the outer gimbal is shown. The purpose of tuning PI parameters of the controller is to attain the most appropriate step response of the secondary control loop in terms of the criteria specified in the previous section.

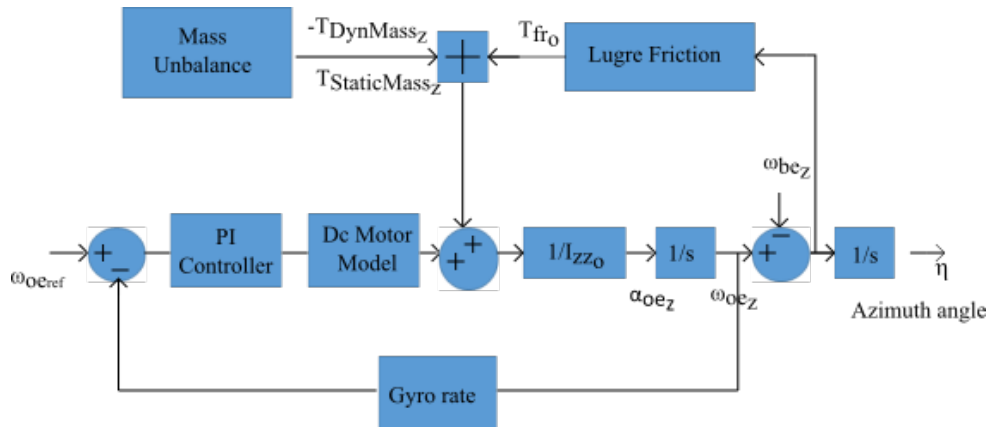


Figure 5.5: The secondary loop of the outer gimbal

The initial values of the parameters are chosen as; $K_p = 20$ and $K_i = 300$. First, K_i is fixed to 300 and K_p is tuned with the values listed in Table 5.2 and it also indicates the dynamics of the step response of the control loop.

Table 5.2: The step response of the secondary control loop with different K_p when $K_i = 300$

K_p	Overshoot (%)	Settling Time (sec)	Steady State Error (%)
20	19.45	0.42	<1
40	11.25	0.48	<1
60	7.86	0.52	<1
80	6.01	0.54	<1
90	5.39	0.54	<1
120	4.07	0.55	<1
140	3.47	0.49	<1

The step responses of the secondary control loop with different K_p gains are depicted in Figure 5.6 as well.

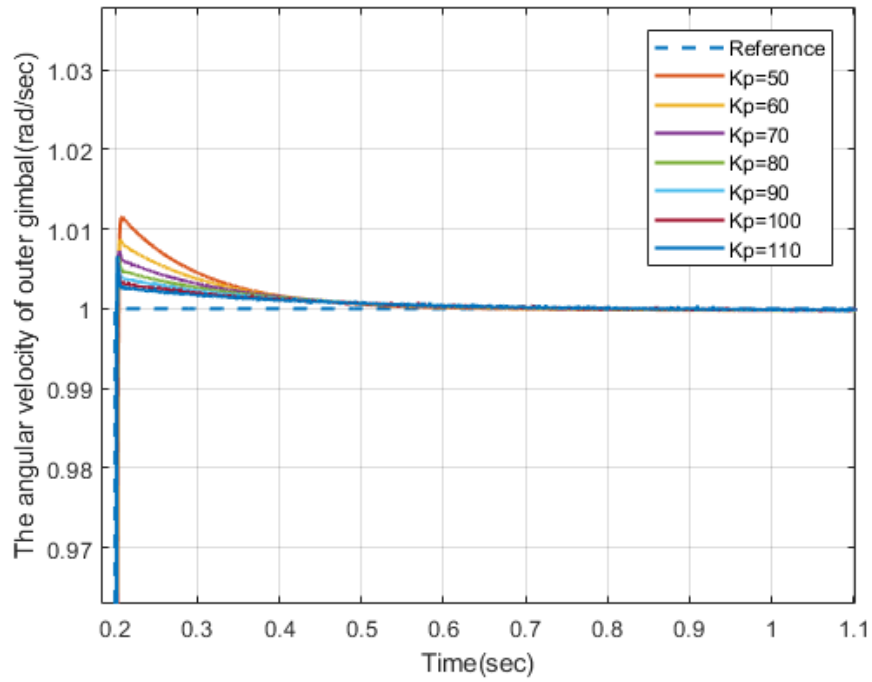


Figure 5.6: The response of the secondary control loop with different K_p when $K_i = 300$

Figure 5.6 and Table 5.2 show that the best results occur when K_p takes 140. Then K_p will be fixed to 140 when K_i has varying values listed in Table 5.3

Table 5.3: The step response of the secondary control loop with different K_i when $K_p = 140$

K_i	Overshoot (%)	Settling Time (sec)	Steady State Error(%)
250	2.87	0.44	<1
300	3.47	0.49	<1
350	4.06	0.52	<1
400	4.65	0.54	<1
450	5.22	0.55	<1

The step responses of the secondary control loop with different K_i gains are shown in Figure 5.7 as well.

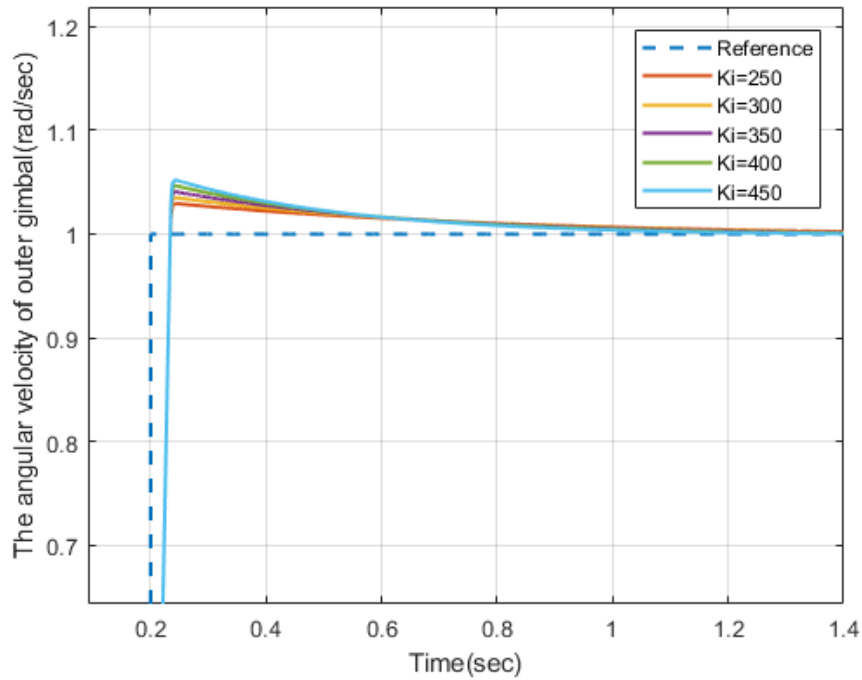


Figure 5.7: The response of the secondary control loop with different K_i when $K_p = 140$

Figure 5.7 and Table 5.3 points out that the best results occur when K_i is assigned to 250. As a result, we can conclude that the best result for the secondary control loop is achieved when $K_p = 140$ and $K_i = 250$.

ii. The Secondary Controller of the Inner Gimbal

In Figure 5.8, the secondary loop of the inner gimbal can be seen. Again, the aim of tuning PI parameters of the controller is to attain the most appropriate step response of the secondary control loop in terms of the criteria specified in the previous section.

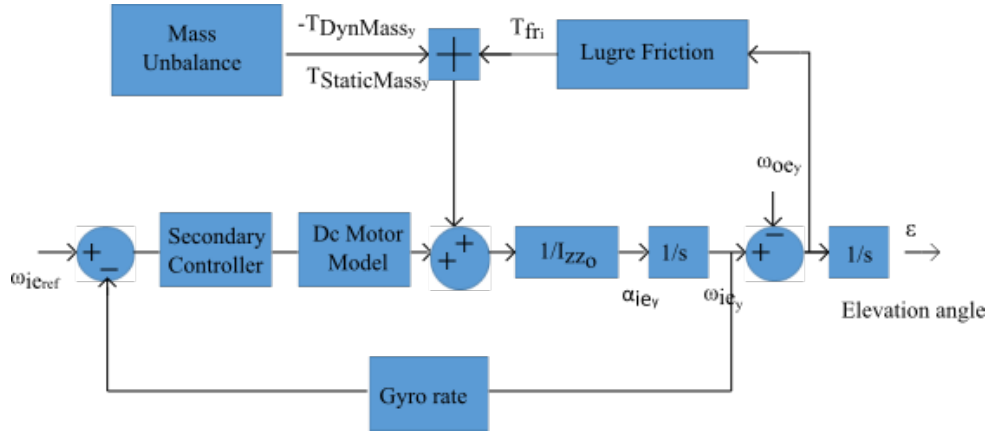


Figure 5.8: The secondary loop of the inner gimbal

The initial values of the parameters as chosen as; $K_p = 5$ and $K_i = 300$. First, K_i is fixed to 300 and K_p is tuned with the varying values listed in Table 5.4 and it also notes the dynamics of the step response of the control loop of inner gimbal.

Table 5.4: The step response of the secondary control loop with different K_p values when $K_i = 300$

K_p	Overshoot (%)	Settling Time (sec)	Steady State Error (%)
5	19.29	0.26	<1
10	11.26	0.27	<1
15	8.02	0.28	<1
20	6.26	0.31	<1
25	5.19	0.32	<1
30	4.47	0.32	<1
35	3.95	0.33	<1

The step responses of the secondary control loop with different K_p gains are indicated in Figure 5.9.

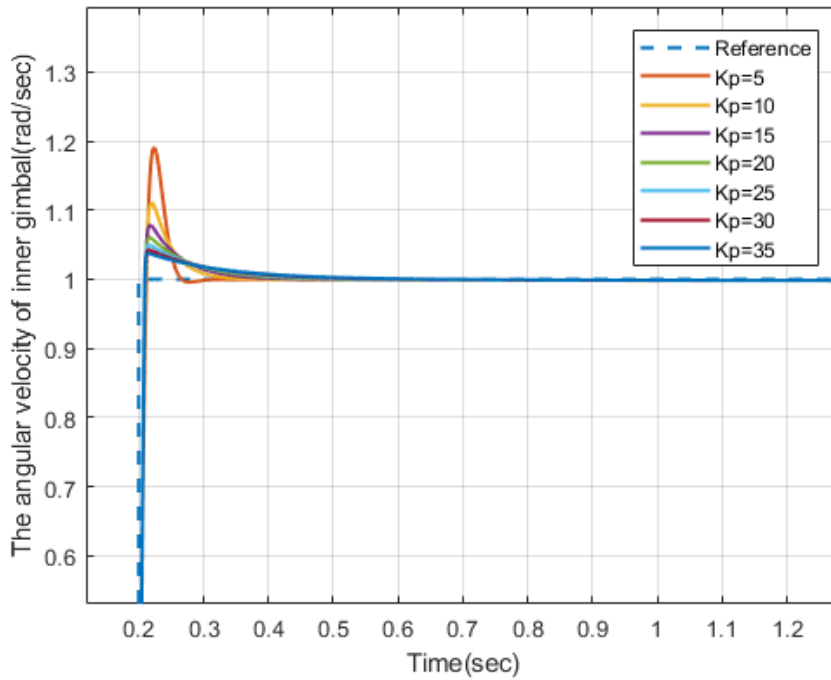


Figure 5.9: The response of the secondary control loop with different K_p values when $K_i = 300$

Figure 5.9 and Table 5.4 figures out that the most appropriate results occur when K_p is chosen as 35. Then K_p will be fixed to 35 when K_i has different values listed in Table 5.5;

Table 5.5: The step response of the secondary control loop with different K_i when $K_p = 35$

K_i	Overshoot (%)	Settling Time (sec)	Steady State Error(%)
250	3.48	0.29	<1
300	3.95	0.30	<1
350	4.46	0.30	<1
400	4.95	0.30	<1
450	5.49	0.29	<1

Similarly, the step responses of the secondary control loop with different K_i gains are shown in Figure 5.10.

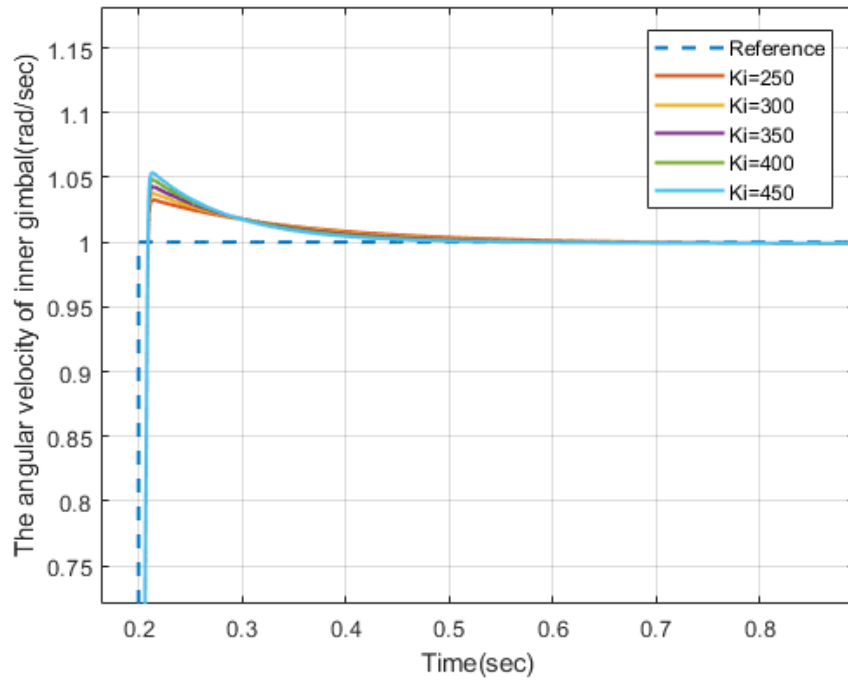


Figure 5.10: The response of the secondary control loop with different K_i values when $K_p = 35$

Therefore, Figure 5.10 and Table 5.5 implies that the best results occur when K_i is assigned to 250. Consequently, we can state that the best result for the secondary control loop of the inner gimbal is performed when $K_p = 35$ and $K_i = 250$.

5.3.3 The Primary Controller Design

i. The Primary Controller of the Outer Gimbal

The primary control loop of the outer gimbal is figured out in Figure 5.3 previously, which is in charge of position control. Again, the tuning of the parameters will be carried out so that the step response of the primary control loop can satisfy the desired conditions in terms of the overshoot, the settling time and the steady state error. The procedure of tuning which is performed in the previous section is repeated in which the PI gains of the secondary controller of the outer gimbal are already tuned with the ones giving the best result.

The initial values of the parameters are specified as; $K_p = 5$ and $K_i = 10$. First, K_i is

fixed to 10 and K_p is varied with the values listed in Table 5.6

Table 5.6: The step response of the primary control loop with different K_p when $K_i = 10$

K_p	Overshoot (%)	Settling Time (sec)	Steady State Error (%)
5	29.67	2.39	<1
5.5	28.75	1.65	<1
6	28.01	1.66	<1
6.5	27.26	1.68	<1
7	26.68	1.69	<1
7.5	27.97	1.69	<1
7.75	30.63	1.68	<1

The step responses of the primary control loop with different K_p gains are indicated in Figure 5.11 as well;

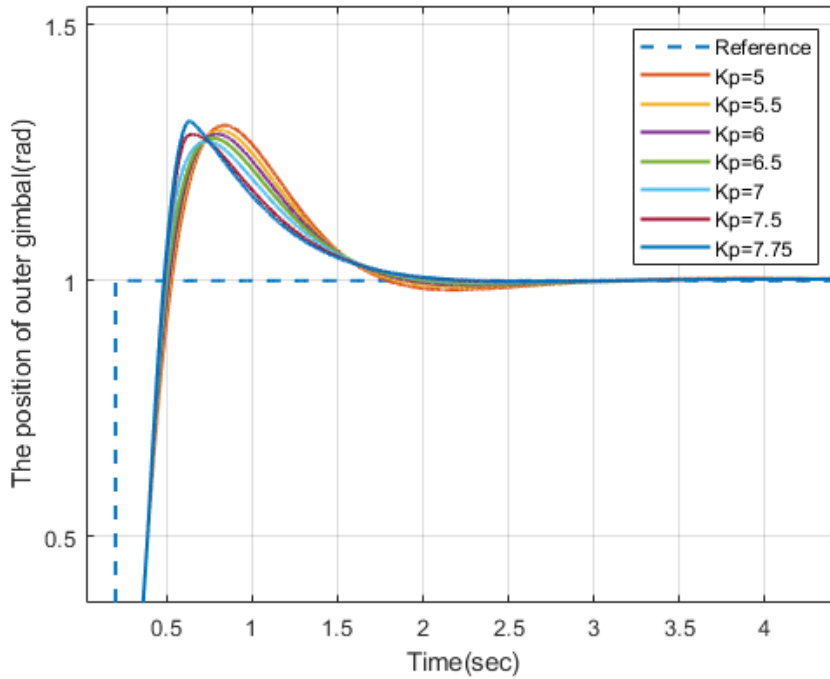


Figure 5.11: The response of the primary control loop with different K_p when $K_i = 10$

Figure 5.11 and Table 5.6 conclude that K_p may be taken as 7. Next, K_p is fixed to 7 and K_i has different values listed in Table 5.7.

Table 5.7: The step response of the primary control loop with different K_i when $K_p = 7$

K_i	Overshoot (%)	Settling Time (sec)	Steady State Error (%)
7	20.86	1.95	<1
8	22.82	1.85	<1
9	24.74	1.77	<1
10	26.68	1.69	<1
11	28.69	1.62	<1

The step responses of the primary control loop with different K_i gains are shown in Figure 5.12 as well.

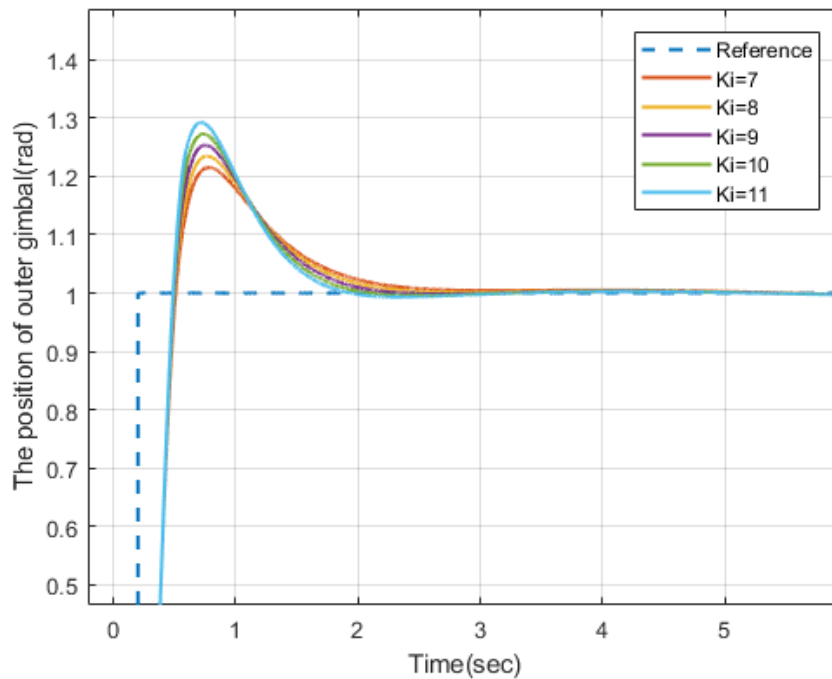


Figure 5.12: The response of the primary control loop with different K_i when $K_p = 7$

Here, Figure 5.12 and Table 5.7 imply that the best result occurs when K_i is assigned to 7. Consequently, we can conclude that K_p, K_i parameters both should take 7.

ii. The Primary Controller of the Inner Gimbal

The primary control loop of the inner gimbal can be seen in Figure 5.4 from the previous section, which handles the position control of the inner gimbal. The tuning of the secondary control loop has been already performed and the suggested PI parameters giving the best result are implemented in the secondary controller here. For the primary controller, K_p and K_i takes the initial values; 8 and 25. First, K_i is fixed to 25 and K_p is varied with the values listed in Table 5.8. The step responses of the primary control loop with different K_p gains are shown in Figure 5.13.

Table 5.8: The step response of the primary control loop with different K_p values when $K_i = 25$

K_p	Overshoot (%)	Settling Time (sec)	Steady State Error(%)
8	25.08	1.17	<1
8.5	25.24	1.18	<1
9	24.85	1.19	<1
9.5	24.53	1.22	<1
10	24.34	1.23	<1
10.5	23.71	1.24	<1
11	23.55	1.25	<1

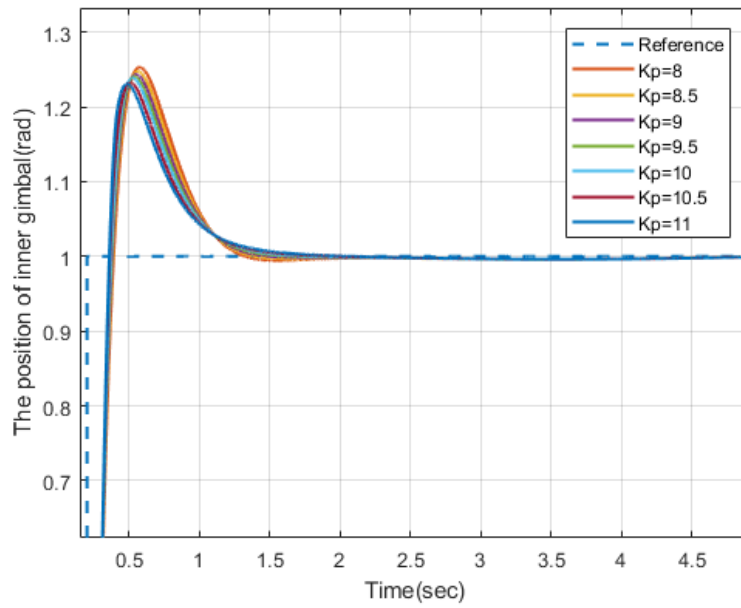


Figure 5.13: The response of the primary control loop with different K_p when $K_i=25$

Figure 5.13 and Table 5.8 show that K_p may be taken as 11. Next, K_p is fixed to 11 and K_i has different values listed in Table 5.9.

Table 5.9: The step response of the primary control loop with different K_i values when $K_p = 11$

K_i	Overshoot (%)	Settling Time (sec)	Steady State Error(%)
20	20.18	1.50	<1
25	23.56	1.26	<1
30	27.09	1.10	<1
35	31.43	0.99	<1
40	36.90	0.91	<1

The step responses of the primary control loop with different K_i gains are shown in Figure 5.14 as well.

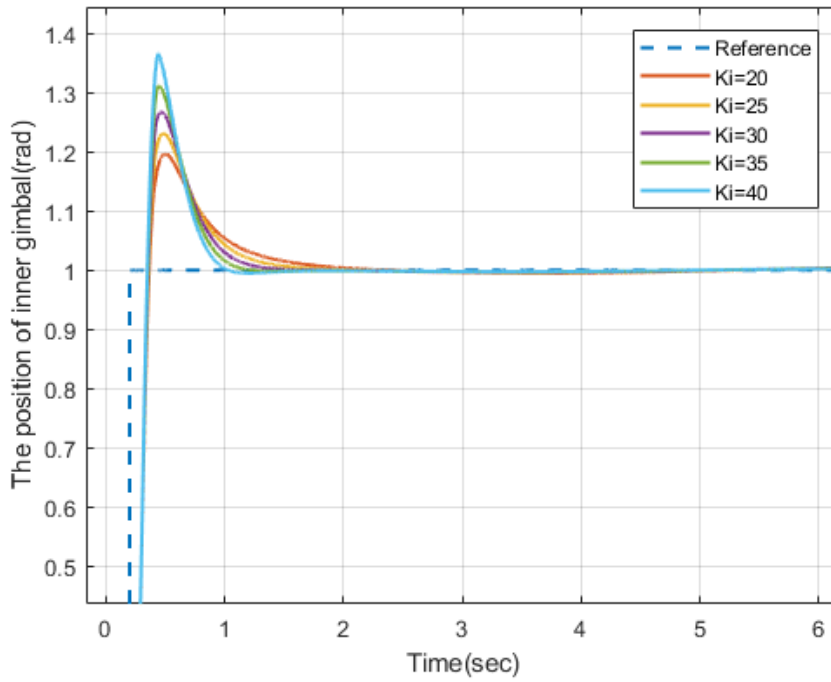


Figure 5.14: The response of the primary control loop with different K_i when $K_p = 11$

Therefore, Figure 5.14 and Table 5.9 imply that the best result occurs when K_i is assigned to 20 and, K_p , K_i parameters should take 11 and 20, respectively.

5.3.4 The Response of the System

In Table 5.10, the resultant parameters of the primary and the secondary controller for both gimbals are noted.

Table 5.10: The resultant parameters of the controller

	Primary Controller		Secondary Controller	
	K_p	K_i	K_p	K_i
Outer Gimbal	7	7	140	250
Inner Gimbal	11	20	35	250

In the previous section, the step responses of the gimbals with the specified parameters have already been investigated. Here, the system performance will be evaluated with a different reference input that includes a small position displacement and a

higher one for both gimbals.

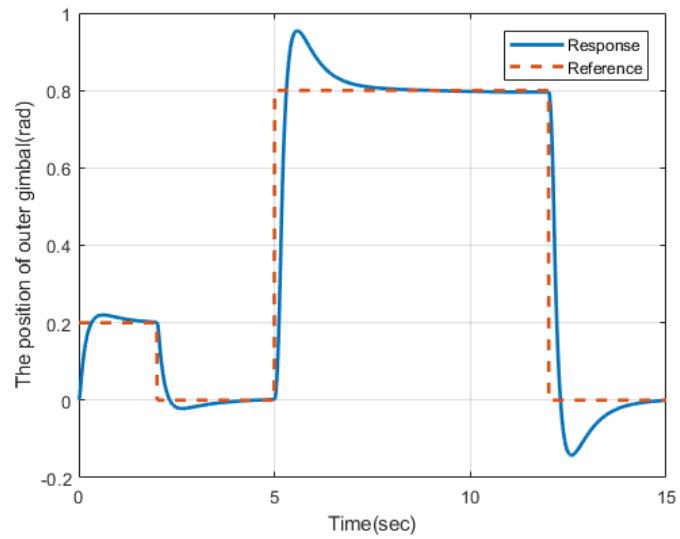


Figure 5.15: The system response of the outer gimbal

In Figure 5.15, the system response of the outer gimbal with respect to the reference signal consisting of two different levels of position tracking is shown. Similarly, the system response of the inner gimbal to the identical reference signal is indicated in Figure 5.16.

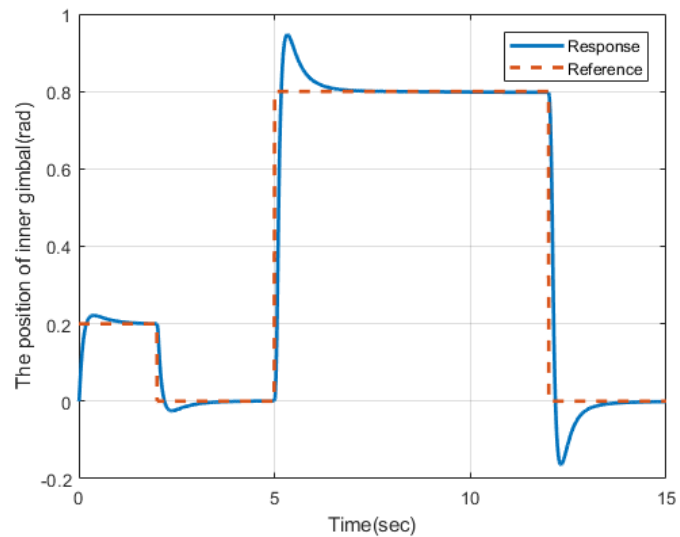


Figure 5.16: The system response of the inner gimbal

The system responses of inner and outer gimbals reveals that the positioning at a higher rate produces more overshoot, which degrades the operation. In fact, a much lower overshoot can be achieved via a prefilter which suppresses the high frequency components of the reference signal [17]. That is why the prefilters will be implemented into the design so that the system response can be enhanced with small overshoots for both gimbals. The parameters of cascade PI will be tuned in a similar way explained previously for the new system to which the prefilters are added.

5.3.5 Cascade PI Controller with Prefilters

In Figure 5.17, the placement of the prefilter block in the stabilization loop is depicted.

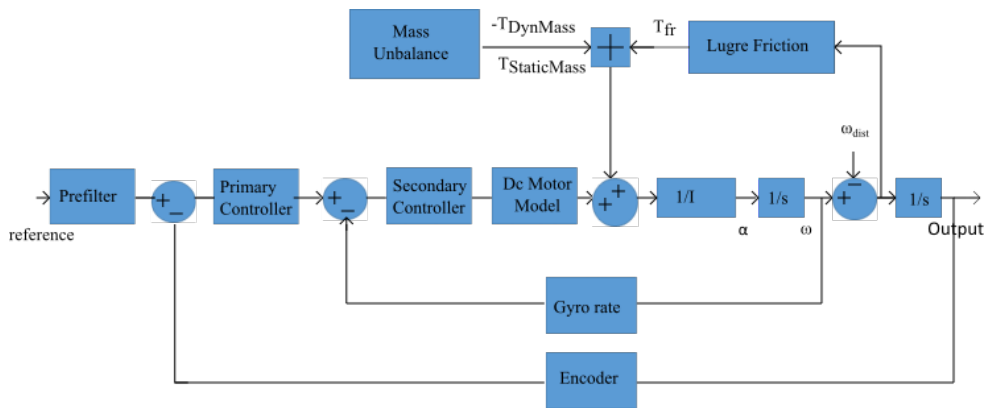


Figure 5.17: The block diagram of the system with prefilter

Transfer functions of the prefilter for the outer gimbal and the inner gimbal are optimized relatively in such a way that the system can achieve a desired response in terms of the overshoot, the settling time and the steady state error:

$$G_{filter_{outer}} = \frac{4.72}{1.3s + 4.72}$$

$$G_{filter_{inner}} = \frac{6.28}{s + 6.28}$$

Table 5.11 shows the resultant new parameters of the controllers for both gimbals which are tuned via the suggested method in the previous section.

Table 5.11: The resultant parameters of the controller with the prefilters

	Primary Controller		Secondary Controller	
	K_p	K_i	K_p	K_i
Outer Gimbal	8	30	150	350
Inner Gimbal	25	300	35	250

Using these values as prefilter parameters, the same reference input specified to evaluate the system in Figures 5.15 and 5.16 is again applied to the control loops to check the effect of the filters. Figure 5.18 and Figure 5.19 show that prefilters added to the system enhance the operation by lowering the overshoot significantly for both gimbals, which attains a much more stable operation.

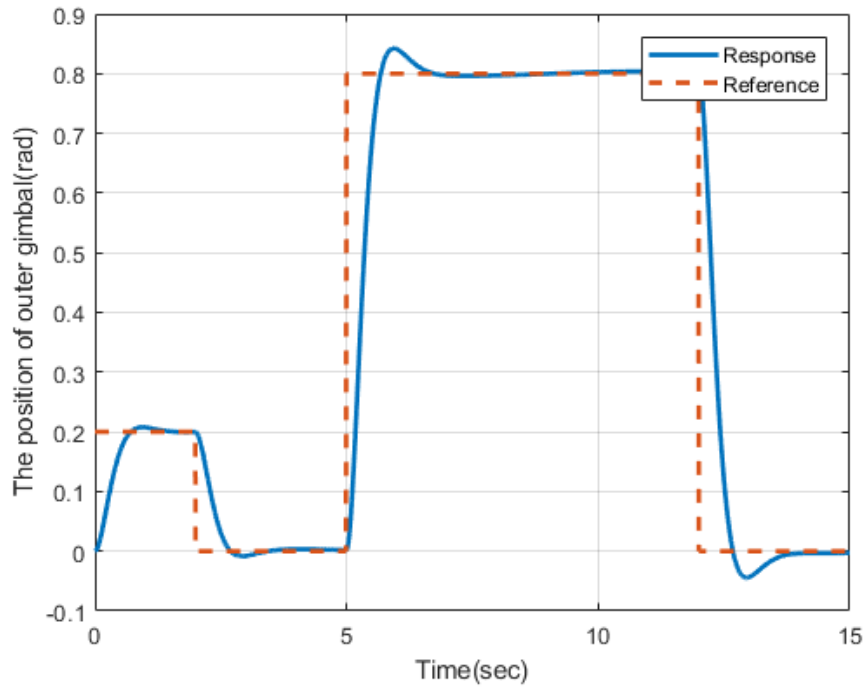


Figure 5.18: The response of the outer gimbal with prefilter

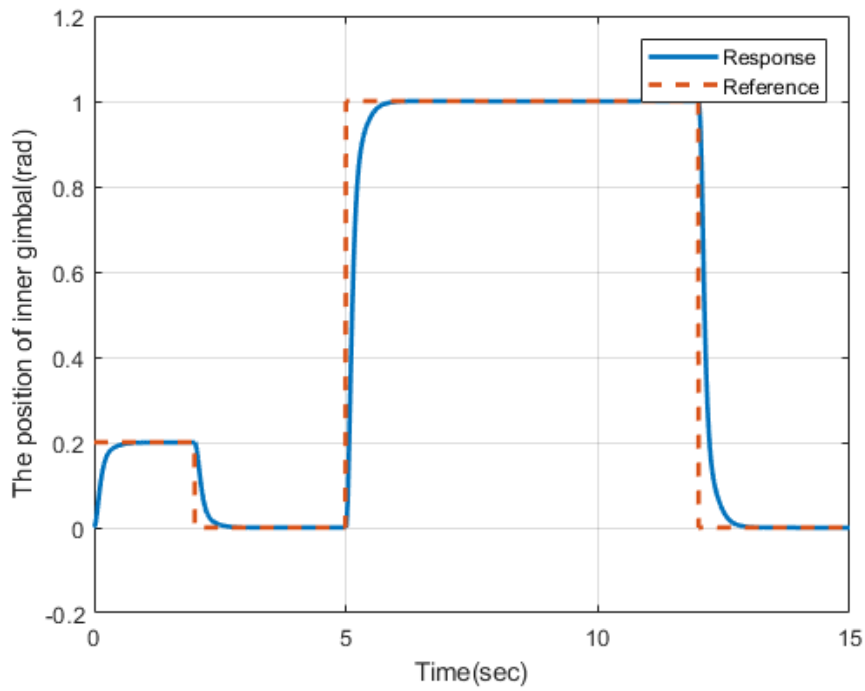


Figure 5.19: The response of the inner gimbal with prefilter

The system response of the outer gimbal to possible different position reference can be found in Table 5.12. Figure 5.20 summarizes the system performance under varying position command.

Table 5.12: The performance of the outer gimbal with different reference inputs

Reference Input	Overshoot (%)	Settling Time (sec)	Steady State Error (%)
0.5 rad	2.85	1.53	<1
0.8 rad	2.87	1.62	<1
1.0 rad	2.86	1.60	<1
1.5 rad	2.89	1.74	<1
2.0 rad	2.92	1.75	<1
2.5 rad	3.27	1.78	<1

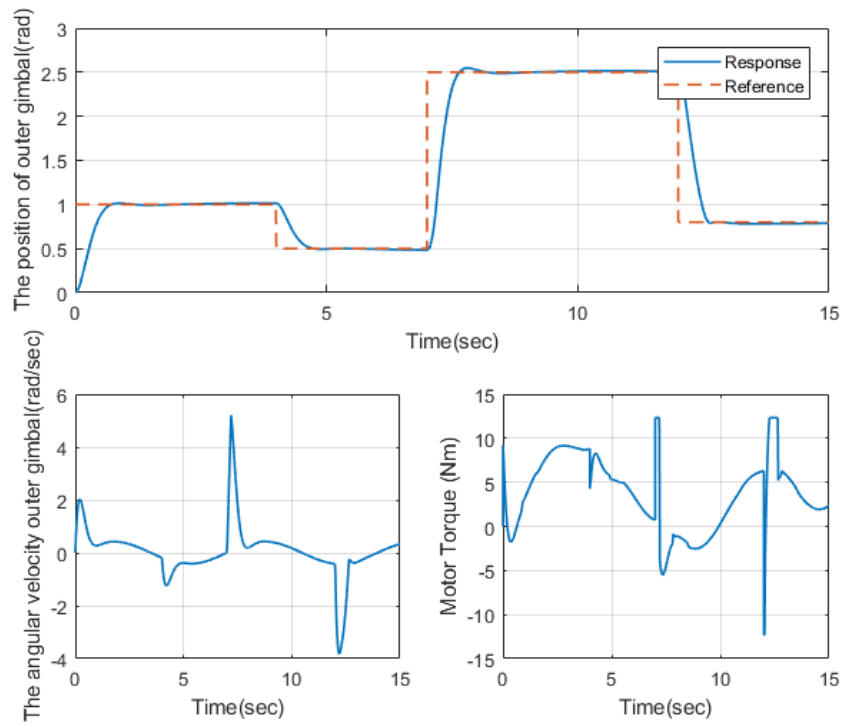


Figure 5.20: The response of the outer gimbal

Table 5.13: The performance of the inner gimbal with different reference inputs

Reference Input	Overshoot (%)	Settling Time (sec)	Steady State Error (%)
0.2 rad	1.62	0.98	<1
0.8 rad	0.45	0.72	<1
1.0 rad	0.41	0.65	<1

In Table 5.13, the possible input references are listed and the system response is evaluated for each one; which is also illustrated in Figure 5.21.

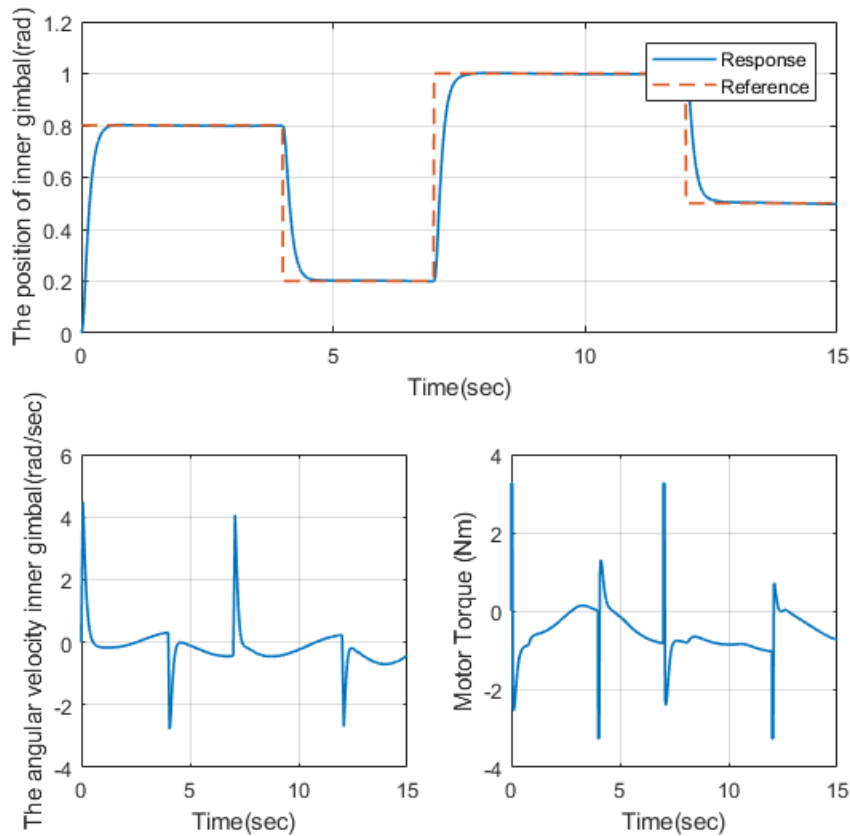


Figure 5.21: The response of the inner gimbal

Therefore, for both outer and inner gimbals, the stable operation at different positioning references is succeeded in terms of the overshoot, settling time and the steady state error with the cascade control systems. Even though the overshoot still exist in outer loop, the prefilter design overcomes the high rate of the overshoot significantly. Table 5.12 shows that when the reference position gets higher values, the overshoot and the settling time increases slightly which ensures the effectiveness of the controllers. For inner gimbal, almost all reference inputs result in a very similar characteristic implying that the controller achieves a stable and a consistent operation after the prefilter is implemented in the inner loop. Hence, it can be concluded that the controller design covered in this section provides inner and outer gimbals a high performance operation.

5.3.6 The Response of the System with Changing Inertia Parameters

In this study, the inertia parameters are obtained from the calculations done with CAD drawing of the physical body. In other words, the parameters in the simulations are the exact values if the physical body is produced perfectly and totally consistent with the drawings. However, this may not be possible all the time which means that the geometry of the body can be slightly different at the end of the production. This makes the inertia matrices different from the predicted values. Therefore, the effectiveness of the controller should be checked when the parameters of the inertia take slightly varying values.

In this section, the system response of the inner and the outer gimbals have been observed when the inertia matrices are assigned to slightly different values by considering the error margin of the parameters. Here, all the parameters of the inertia tensors of both the inner and the outer gimbals are increased by twenty percent and the system responses have been observed with different reference inputs again. The results have been listed in Table 5.14 for the outer gimbal and in Table 5.15 representing the system response of the inner gimbal.

Table 5.14: The performance of the outer gimbal with different reference inputs

Reference Input	Overshoot (%)	Settling Time (sec)	Steady State Error (%)
0.5 rad	5.51	1.83	<1
0.8 rad	3.41	1.81	<1
1.0 rad	2.87	1.75	<1
1.5 rad	2.84	1.74	<1
2.0 rad	2.95	1.81	<1
2.5 rad	4.39	1.83	<1

Table 5.15: The performance of the inner gimbal with different reference inputs

Reference Input	Overshoot (%)	Settling Time (sec)	Steady State Error (%)
0.2 rad	2.61	1.10	<1
0.8 rad	1.30	0.72	<1
1.0 rad	0.47	0.68	<1

For the outer gimbal, when we compare the results in Table 5.14 and Table 5.12, it can be argued that the overshoot and the settling time have increased; however, they are still close to each other, which keeps the stable operation of the outer gimbal. Therefore, the results imply that even if the error margin of the inertia parameters are taken as twenty percent, the controller can achieve a stable operation.

Similarly, for the inner gimbal, when we look at the results in Table 5.15 and Table 5.13, we can figure out that the overshoot and the settling time have increased slightly, which still maintains the stable operation of the inner gimbal. All in all, the comparison points out that even if the error margin of the inertia parameters of the inner body are considered as twenty percent, the system response will be stable with the controller implemented in this study.

CHAPTER 6

CONCLUSION AND FUTURE WORK

6.1 Conclusion

In real world, many examples of the inertially stabilized systems are implemented to achieve high performance in different tracking scenarios. The degree of freedom and the electromechanical design may vary according to the application; however, they all serve a common purpose, an effective stabilization. In this thesis work, one example of the stabilized systems has been investigated. The aim is to stabilize the two-axes gimballed antenna platform, a part of the satellite communication system. The main idea has been to maintain the antenna consisting of the inner and the outer gimbal linked with the satellite when the aircraft it is mounted on moves. To attain this operation, the high precision positioning of both inner and outer gimbals has been studied by working on the detailed dynamic modelling and the control of the system.

The study has started with the task focusing on the dynamic modelling in Chapter 2. The problem of the chapter has been defined as to obtain the dynamic equations of the antenna platform mounted on a moving aircraft. First, the reference frames and the transformation matrices describing the projection between the frames have been studied by probing the mathematical concepts behind it in a detailed way. And then, the kinematic equations, standing for the equations describing the angular velocity and the angular acceleration of the inner and the outer gimbal, have been established. During the derivation of the kinematic equations, the mathematical concepts about the reference frames and the transformation matrices have had a great important role. Next, the dynamic equations worked via Newton-Euler approach, based on the rela-

tionship between the all torques the system experience and the variation of the angular momentum, have been built up. At this stage, in addition to the input torques due to the actuators, the disturbance torques resulting from the nonlinearities of the system have been also introduced to the work, which have also been detailed in Chapter 3 and Chapter 4 as dynamic, static mass unbalance and the friction torque.

Chapter 3 has presented an elaborative work regarding the mass unbalance. First, the concept of the dynamic mass unbalance has been examined and the derivation of it has been accomplished for the outer and the inner gimbals separately. The answer for the question how dynamic mass unbalance affects the system operation under different conditions has been sought. For this purpose, the stabilization loops dealing with the velocity control have been formed and tested with varying angular velocities of the aircraft the antenna mounted on when the system is effected by the dynamic mass unbalance. The similar procedure has been performed to understand the static mass unbalance concept and the influence of it on the system performance. Consequently, it has been concluded that mass unbalance may degrade the system operation significantly for both inner and the outer gimbals. Especially, at low velocities, the disturbance due to inertial dynamics have become more dominant and affected the system more negatively. That is why, it has been clarified that the mass unbalance concept should be taken into consideration not only to attain the required operation properly but also to enhance the system performance.

The friction torque has been introduced to the system when the dynamic equations have been derived in Chapter 2 and it has been investigated deeply in Chapter 4. First, static and dynamic friction models describing the friction between two surfaces have been studied and LuGre friction model, a dynamic model, has been compromised to implement into the system. Friction identification has been accomplished with two sets of experiments conducted on the real physical antenna platform provided by ASELSAN. The experiments have been categorized as the sliding experiments handling the velocity versus the friction torque mapping and the presliding phase experiments describing the dynamic behaviour of the friction torque at very low velocities around zero. The results have been evaluated with the defined identification methods and LuGre friction model has been achieved for both gimbals, which has been integrated into Simulink/MATLAB model later. And then the dynamic identification

of parameters of the friction model has been revised in Simulink environment with a different method as well; thus, the results have been compared. Consequently, by the means of this work, the friction torque appeared in the dynamic equations has been described and implemented into the dynamic model of the system.

Finally, after the work so far, the detailed dynamic modelling has been succeeded and carried into Simulink/MATLAB. Next, the aim has been to control the system in an effective way. To determine the method of the control, many similar applications have been investigated. Thus, cascade PI controller has become the approach for positioning since it provides a high performance and it is cost effective, easily-applicable in industrial applications. The tuning has been performed on the coupled system which experiences all the disturbance introduced previously. The response of the system has been satisfying in terms of the settling time and the steady state error; however, the overshoot has needed to be decreased. Therefore, a prefilter has been added to the system, which has resulted in a lower overshoot of the responses of the inner and the outer gimbals. All in all, the required control of the system dynamically modelled in a detailed way has been achieved in Simulink/MATLAB environment.

6.2 Future Work

In this thesis, the dynamic modelling and the control of a 2-DOF gimbaled antenna system has been performed, in simulations mostly. Unfortunately, the work has not been projected on the physical body since the proper conditions have not been satisfied to work with the physical system yet. When the physical system is ready to work, the system model may be compared with the model experimentally obtained. Next, the controller design may be revisited again. In this thesis, only cascade PI type controllers have been implemented. As the platform becomes available physically and the dynamic model is verified, the other modern control methods may be applied on system to attain a higher performance.

At the very beginning of this work, one of the main purposes was to come up with a dynamic friction model for the system at different temperatures and to observe the influence of the operational temperature on the friction dynamics since the system was supposed to function at a wide range temperatures between -40°C and 85°C . That is why, it was planned to perform the friction identification at different temperatures and according to the result, to apply an adaptive control method. Therefore, when the system is completed in terms of electromechanical integration, the planned task may be worked on via the friction identification method suggested in this thesis work.

REFERENCES

- [1] J. Hilkert, "Inertially stabilized platform technology concepts and principles," *IEEE Control Systems*, vol. 28, no. 1, pp. 26–46, 2008.
- [2] R. Jia, V. K. Nandikolla, G. Haggart, C. Volk, and D. Tazartes, "System performance of an inertially stabilized gimballed platform with friction, resonance, and vibration effects," *Journal of Nonlinear Dynamics*, vol. 2017, pp. 1–21, 2017.
- [3] P. J. Kennedy and R. L. Kennedy, "Direct versus indirect line of sight (los) stabilization," *IEEE Transactions on Control Systems Technology*, vol. 11, no. 1, pp. 3–15, 2003.
- [4] A. Battistel, F. Lizarralde, and L. Hsu, "Inertially stabilized platforms using dual-axis gyros: sensitivity analysis to unmodeled motion and an extension to visual tracking," *American Control Conference*, September 2011.
- [5] S. Leghmizi, S. Liu, R. Fraga, and A. Boughelala, "Dynamics modeling for satellite antenna dish stabilized platform," *Advanced Materials Research*, vol. 566, pp. 187–196, 2012.
- [6] Aselsan. Satellite communication systems solutions. [Online]. Available: https://www.aselsan.com.tr/en-us/capabilities/cpb3/Brochures/Satellite_Air_Platform/Satellite%20Communication%20Systems%20Air%20Platform%20Solutions.pdf
- [7] M. M. Abdo, A. R. Vali, A. R. Toloie, and M. R. Arvan, "Stabilization loop of a two axes gimbal system using self-tuning pid type fuzzy controller," *ISA transactions*, vol. 53, no. 2, pp. 591–602, 2014.
- [8] A. Habashi, M. Ashry, M. Mabrouk, and G. Elnashar, "Controller design for line of sight stabilization system," *International Journal of Engineering Research and Technology*, vol. 4, no. 11, pp. 650–658, 2015.
- [9] C. Knospe, "Pid control," *IEEE Control Systems*, vol. 26, no. 1, pp. 30–31, 2006.
- [10] J.-L. Boiffier, *The dynamics of flight*. Wiley, 1998.
- [11] S. Leghmizi and L. Sheng, "Kinematics modeling for satellite antenna dish stabilized platform," *2010 International Conference on Measuring Technology and Mechatronics Automation*, vol. 2, pp. 558–563, March 2010.

- [12] H. Høifødt, “Dynamic modeling and simulation of robot manipulators: The newton-euler formulation,” Master’s thesis, Institutt for teknisk kybernetikk, 2011.
- [13] S. Leghmizi and L. Sheng, “Dynamics modeling for satellite antenna dish stabilized platform,” *Measuring Technology and Mechatronics Automation, International Conference on*, vol. 2, pp. 558–563, 2010.
- [14] H. Khodadadi, M. R. J. Motlagh, and M. Gorji, “Robust control and modeling a 2-dof inertial stabilized platform,” *Electrical, Control and Computer Engineering (INECCE), 2011 International Conference on*, pp. 223–228, 2011.
- [15] F. N. Barnes, “Stable member equations of motion for a three-axis gyro stabilized platform,” *IEEE Transactions on Aerospace and Electronic Systems*, no. 5, pp. 830–842, 1971.
- [16] E. Poyrazoglu, “Detailed modeling and control of a 2-dof gimbal system,” Master’s thesis, METU, Ankara, Turkey, 2017.
- [17] T. Öztürk, “Angular acceleration assisted stabilization of a 2-dof gimbal platform,” Master’s thesis, METU, Ankara, Turkey, 2010.
- [18] H. F. Al-Shuka, B. J. Corves, and W.-H. Zhu, “Dynamic modeling of biped robot using lagrangian and recursive newton-euler formulations,” *International Journal of Computer Applications*, vol. 101, no. 3, pp. 1–8, 2014.
- [19] M. Abdo, A. R. Vali, A. Toloiei, and M. R. Arvan, “Research on the cross-coupling of a two axes gimbal system with dynamic unbalance,” *International Journal of advanced robotic systems*, vol. 10, no. 10, pp. 357–370, 2013.
- [20] B. Ekstrand, “Equations of motion for a two-axes gimbal system,” *IEEE Transactions on Aerospace and Electronic Systems*, vol. 37, no. 3, pp. 1083–1091, 2001.
- [21] O. Hasturk, A. M. Erkmén, and İ. Erkmén, “Proxy-based sliding mode stabilization of a two-axis gimbaled platform,” *target*, vol. 3, no. 4, pp. 1–7, 2011.
- [22] H. Khodadadi, M. R. J. Motlagh, and M. Gorji, “Robust control and modeling a 2-dof inertial stabilized platform,” *Electrical, Control and Computer Engineering (INECCE), 2011 International Conference on*, pp. 223–228, 2011.
- [23] D. R. Otlowksi, K. Wiener, and B. A. Rathbun, “Mass properties factors in achieving stable imagery from a gimbal mounted camera,” *Airborne intelligence, surveillance, reconnaissance (ISR) systems and applications V*, vol. 6946, p. 69460B, 2008.
- [24] M. Abdo, A. Toloiei, A. R. Vali, and M. R. Arvan, “Cascade control system for two axes gimbal system with mass unbalance,” *International Journal of Scientific & Engineering Research*, vol. 4, no. 9, pp. 903–912, 2013.

- [25] V. Van Geffen, “A study of friction models and friction compensation,” *DCT*, vol. 118, pp. 10–14, 2009.
- [26] X. Wang, S. Lin, and S.-P. Wang, “Dynamic friction parameter identification method with lugre model for direct-drive rotary torque motor,” vol. 2016, pp. 1–8, 2016.
- [27] C. H. Rivetta and S. Hansen, “Friction model of the 2.5-mts sdss telescope,” *Telescope Control Systems III*, vol. 3351, pp. 466–478, 1998.
- [28] C. C. De Wit, H. Olsson, K. Astrom, and P. Lischinsky, “Dynamic friction models and control design,” *American Control Conference, 1993*, pp. 1920–1926, 1993.
- [29] T. Kumar and R. Banavar, “Identification of friction in the 50/80 cm aries schmidt telescope using the lugre model,” *Proc. of the 18th IFAC World Congress*, vol. 18, pp. 980–985, 2011.
- [30] C. De Wit, H. Olsson, K. J. Astrom, and P. Lischinsky, “A new model for control of systems with friction,” *IEEE Transactions on Automatic Control*, vol. 40, no. 3, pp. 419–425, 1995.
- [31] L. Alvarez, J. Yi, R. Horowitz, and L. Olmos, “Dynamic friction model-based tire-road friction estimation and emergency braking control,” *Journal of Dynamic Systems, Measurement, and Control*, vol. 127, no. 1, pp. 22–32, 2005.
- [32] P. R. Dahl, “A solid friction model,” Aerospace Corp El Segundo Ca, Tech. Rep., 1968.
- [33] H. Olsson, K. J. Åström, C. C. De Wit, M. Gäfvert, and P. Lischinsky, “Friction models and friction compensation,” *Eur. J. Control*, vol. 4, no. 3, pp. 176–195, 1998.
- [34] M. Fuad and F. Ikhouane, “Advances on lugre friction model,” *World Academy of Science, Engineering and Technology*, vol. 82, no. 36, pp. 207–212, 2013.
- [35] K. Johanaström and C. Canudas-De-Wit, “Revisiting the lugre friction model,” *IEEE control Systems*, vol. 28, no. 6, pp. 101–114, 2008.
- [36] Y. Liu, J. Li, Z. Zhang, X. Hu, and W. Zhang, “Experimental comparison of five friction models on the same test-bed of the micro stick-slip motion system,” *Mechanical Sciences*, vol. 6, no. 1, pp. 15–28, 2015.
- [37] E. Sincar, “Friction identification and compensation in stabilized pplatforms,” Master’s thesis, METU, Ankara, Turkey.
- [38] D. A. Haessig and B. Friedland, “On the modeling and simulation of friction,” *Journal of Dynamic Systems, Measurement, and Control*, vol. 113, no. 3, pp. 354–362, 1991.

- [39] C. Canudas-de Wit and P. Lischinsky, “Adaptive friction compensation with dynamic friction model,” *IFAC Proceedings Volumes*, vol. 29, no. 1, pp. 2078–2083, 1996.
- [40] H. Olsson, “Control systems with friction,” Ph.D. dissertation, Department of Automatic Control, Lund Institute of Technology (LTH), Lund, Sweden, 1996.
- [41] A. Singh, R. Thakur, and D. S Chatterjee, “Design and optimal control of line of sight stabilization of moving target,” *IOSR Journal of Electrical and Electronics Engineering*, vol. 9, pp. 27–32, 2014.
- [42] S. Kuseyri, “Modelling and stabilization of a three-axis ship-mounted mobile antenna system,” *Proceedings of the Institution of Mechanical Engineers, Part M: Journal of Engineering for the Maritime Environment*, vol. 231, no. 2, pp. 533–541, 2017.
- [43] S. Mandra, “Comparison of automatically tuned cascade control systems of servo-drives for numerically controlled machine tools,” *Elektronika ir elektrotechnika*, vol. 20, no. 3, pp. 16–23, 2014.
- [44] M. Malaysia, “Non-linear modeling and cascade control of an industrial pneumatic actuator system,” *Australian Journal of Basic and Applied Sciences*, vol. 5, no. 8, pp. 465–477, 2011.
- [45] G. Zhang, “Speed control of two-inertia system by pi/pid control,” *IEEE Transactions on Industrial Electronics*, vol. 47, no. 3, pp. 603–609, 2000.
- [46] F. Haugen, *PID control*. Tapir Academic Press Trondheim, 2004, vol. 238.
- [47] M. R. Kondareddy, “Simulation and analysis of cascaded pid controller design for boiler pressure control system,” *International Journal of Informative and Futuristic Research*, vol. 1, pp. 117–126, 2014.

APPENDIX A

THE PARAMETERS

Table A.1: The parameters of the outer gimbal

Parameter	Value	Unit
I_{xx_o}	0.2028	$kg.m^2$
I_{yy_o}	0.3481	$kg.m^2$
I_{zz_o}	0.4386	$kg.m^2$
$I_{xy_o} = I_{yx_o}$	0.04218	$kg.m^2$
$I_{xz_o} = I_{zx_o}$	0.006896	$kg.m^2$
$I_{yz_o} = I_{zy_o}$	0.0002447	$kg.m^2$
$r_{oc_{ox}}$	0.06356	m
$r_{oc_{oy}}$	-0.01475	m
$r_{oc_{oz}}$	-0.01767	m
m_o	14.63	kg

Table A.2: The parameters of the inner gimbal

Parameter	Value	Unit
I_{xx_i}	0.03047	$kg.m^2$
I_{yy_i}	0.06959	$kg.m^2$
I_{zz_i}	0.06420	$kg.m^2$
$I_{xy_i} = I_{yx_i}$	0.0004686	$kg.m^2$
$I_{xz_i} = I_{zx_i}$	0.0006625	$kg.m^2$
$I_{yz_i} = I_{zy_i}$	0.0002815	$kg.m^2$
$r_{oc_{ix}}$	0.02084	m
$r_{oc_{iy}}$	-0.0009696	m
$r_{oc_{iz}}$	0.007755	m
m_i	5.08	kg